HIDROGÉIS DE QUITOSANA LIVRE DE CÉLULAS E REFORÇADOS POR NANOTUBOS DE CARBONO E NANOPARTÍCULAS DE HIDROXIAPATITA PARA APLICAÇÃO EM TECIDO ÓSSEO

CELL-FREE CHITOSAN HYDROGELS REINFORCED BY CARBON NANOTUBES AND HYDROXYAPATITE NANOPARTICLES FOR BONE TISSUE APPLICATION

JOÃO PAULO RUIZ LUCIO DE LIMA PARRA

PhD Candidate

Botucatu

2024

UNIVERSIDADE ESTADUAL PAULISTA

"JÚLIO DE MESQUITA FILHO"

Instituto de Biociências de Botucatu

João Paulo Ruiz Lucio de Lima Parra

CELL-FREE CHITOSAN HYDROGELS REINFORCED BY CARBON NANOTUBES AND HYDROXYAPATITE NANOPARTICLES FOR BONE TISSUE APPLICATION

Thesis submitted to the Institute of Biosciences, Botucatu Campus, UNESP, for the Defense Examination for the Doctoral Program in Biotechnology, in Biotechnology Applied to Human and Animal Health

Advisor: Profº. Drº. Willian Fernando Zambuzzi

Co-advisor: Drº. Murillo Longo Martins

Botucatu-SP

2024

FICHA CATALOGRÁFICA ELABORADA PELA SEÇÃO TÉC. AQUIS. TRATAMENTO DA INFORM.
DIVISÃO TÉCNICA DE BIBLIOTECA E DOCUMENTAÇÃO - CÂMPUS DE BOTUCATU - UNESP

BIBLIOTECÁRIA RESPONSÁVEL: ROSANGELA APARECIDA LOBO-CRB 8/7500

Parra, João Paulo Ruiz Lucio de Lima.
Hidrogéis de quitosana livre de células e reforçados por nanotubos de carbono e nanopartículas de hidroxiapatita para aplicação em tecido ósseo / João Paulo Ruiz Lucio de Lima Parra. - Botucatu, 2024

Tese (doutorado) - Universidade Estadual Paulista (UNESP), Instituto de Biociências, Botucatu
Orientador: Willian Fernando Zambuzzi
Coorientador: Murillo Longo Martins
Capes: 90194000

1. Bioimpressão. 2. Materiais biomédicos. 3. Engenharia tecidual. 4. Medicina regenerativa.

Palavras-chave: Bioimpressão 3D; Biomateriais; Biotinta; Engenharia de tecidos; Medicina regenerativa.

ATA DA DEFESA PÚBLICA DA TESE DE DOUTORADO DE JOÃO PAULO RUIZ LUCIO DE LIMA PARRA, DISCENTE DO PROGRAMA DE PÓS-GRADUAÇÃO EM BIOTECNOLOGIA, DO INSTITUTO DE BIOCIÊNCIAS - CÂMPUS DE BOTUCATU.

Aos 26 dias do mês de julho do ano de 2024, às 09:00 horas, por meio de Videoconferência, realizou-se a defesa de TESE DE DOUTORADO de JOÃO PAULO RUIZ LUCIO DE LIMA PARRA, intitulada **HIDROGÉIS DE QUITOSANA INJETÁVEL LIVRE DE CÉLULAS E REFORÇADOS POR NANOTUBOS DE CARBONO E NANOPARTÍCULAS DE HIDROXIAPATITA PARA APLICAÇÃO EM TECIDO ÓSSEO**. A Comissão Examinadora foi constituida pelos seguintes membros: Dr. MURILLO LONGO MARTINS (Co-orientador(a) - Participação Virtual) do(a) Neutron Scattering Division / Oak Ridge National Laboratory (Knoxville, Tennessee, EUA), Profa. Dra. MARGARIDA JURI SAEKI (Participação Virtual) do(a) Departamento de Ciências Químicas e Biológicas – Setor de Química e Bioquímica / Instituto de Biociências - UNESP - Botucatu, Prof. Dr. JOSE MAURO GRANJEIRO (Participação Virtual) do(a) Departamento de Biologia Celular e Molecular / UFF e INMETRO, Profa. Dra. ANA PAULA RAMOS (Participação Virtual) do(a) Departamento de Química / Faculdade de Filosofia, Ciências e Letras de Ribeirão Preto da Universidade de São Paulo-FFCLRP, Profa. Dra. CECÍLIA HELENA DE AZEVEDO GOUVEIA FERREIRA (Participação Virtual) do(a) Departamento de Anatomia do Instituto de Ciências Biomédicas / Universidade de São Paulo – Campus de São Paulo. Após a exposição pelo doutorando e arguição pelos membros da Comissão Examinadora que participaram do ato, de forma presencial e/ou virtual, o discente recebeu o conceito final:_ _Aprovado_ _ _ _ _ _ . Nada mais havendo, foi lavrada a presente ata, que após lida e aprovada, foi assinada pelo(a) Presidente(a) da Comissão Examinadora.

Dr. MURILLO LONGO MARTINS

Documento assinado digitalmente
gov.br
MURILLO LONGO MARTINS
Data: 26/07/2024 16:05:04-0300
Verifique em https://validar.iti.gov.br

“To be a scientist is to be naive.

We are so focused on our search for truth,

We fail to consider how few actually want us to find it.

But it is always there, whether we see it or not,

Whether we choose to or not.

The truth does not care about our needs or wants.

It does not care about our governments, our ideologies, our religions.

It will lie in wait for all time.”

- *Valery Legasov*

À minha avó Affonsa (in memorian), Aos meus pais, Paulo (in memorian) e Marília,

À toda a minha família paterna e materna,

À minha irmã Gabriela e meu sobrinho René,

À minha namorada, Ana Carolina,

Ao infinito, e além!

Agradecimentos

Primeiramente, gostaria de agradecer ao Plano Maior pela oportunidade desta existência e passagem e aos meus guias que me intuem a todo o momento em busca da curiosidade constante.

Agradeço do fundo de minha alma aos meus pais, Paulo *(in memorian)* e Marília, e minha irmã, Gabriela, e aos meus tios, Paulo e Luciana, pelo apoio seja qual tenha sido a circunstância, mas todas recheadas de vida e de lindos momentos. Se vivo, são por vocês. Em especial, ao meu recente guia espiritual, meu pai, que continua sendo uma doce alma que envia abelhas periódicas para dizer que está por perto, mas que também desbrava a Espiritualidade nos confins da Eternidade.

Ao meu orientador e valiosíssimo amigo, Profº Willian Fernando Zambuzzi, pela oportunidade dada e por nunca deixar de acreditar no meu potencial, pela surpreendente acolhida no momento em que todas as possibilidades pareciam ter se esgotado, por todo o amparo, esforço, dedicação e paciência comigo desde esta acolhida durante o meu doutorado até os momentos de agora, mais díficeis. Apesar disso, são incontáveis alegrias profissionais alcançadas que jamais pensei realizar tão cedo.

Ao amigo e co-orientador, Murillo, por todos os conselhos e ponderações sempre construtivas e pela amizade que se matém desde outrora. A sua contribuição na minha formação e neste trabalho é imensurável. Obrigado por tudo.

À todos as professoras e professores que tive durante toda a minha vida: Elma, Elza, Fabiana, Veras, Lúcia, Elcione, Sato, Sebastião, Sérgio, Antônio, Sandras, Elizabeth, Lucianas, Denise, Mariza, Nelson, Fany, Rosine, Pedro, Christina, Anas Marias, Cláudias, Lídia, Etiene, Luís, Joel, José Luís, José Ricardo, Rezende, Vladmir, Ney, Fontes, Paulos, Roberto, José Roberto, Gustavo, Willian, Sônia, Júlio, Pedro Padilha, Giuseppina e Fernando. Em especial, à professora Margarida Saeki e ao professor Valber Pedrosa, meus ex-orientadores, por terem semeado em mim a vontade de fazer ciência e a encará-la como um trabalho, as vezes muito árduo, mas sempre.

To my invaluable friends and teammates from WFIRM, Jun Tae Huh, Wonwoo Jeong, Joshua Copus, Joshua Cheng, Adit Mehta, Seongyu Jeon, Siyuhan "Claire" Li, , for all

the most extraordinary moments during my stay in the USA. Also, to Dr. Sang Jin Lee, Dr. Shay Soker, Dr. James J. Yoo, and Dr. Anthony Atala for all the mentorship during my stay in the USA between 2022 and 2023 to show me how to do state-of-the-art science and for all the invaluable advices about life and work.

Aos colegas do **LaBIO**, Amanda, Anderson, Beatriz, Emerson, Geórgia, Guilherme, Marcel, Matheus Luquirini e Matheus Amaral, Suelen pela convivência e rotina durante todos esses anos, das conversas descontraídas, de cafés à discussões científicas ou não. Devo à vocês pelo conhecimento e maturidade adquiridos durante estes anos.

Aos amigos que Botucatu pode me proporcionar durante todos esses anos das Repúblicas PMD, Vizinhos e Zona Azul, por todas as risadas e loucuras. Em especial, gostaria também de agradecer aos meus grandes amigos Helton (Beyoncé), Renan (Gregui), Felipe (Jabulani), Gabriel (Mais/GEV) e novamente Marcel (Ptinha), por todos esses anos de grande amizade bem vividos e e devidamente aproveitados.

Aos funcionários do departamento de Ciências Químicas e Biológicas, do setor de Química e Bioquímica: Gabriela, Danielle, Elaine, Silvia, Selma, Ivalde, Fabinho, Ester e Rose por todo o convívio e suporte desde a iniciação científica até o doutorado.

Aos irmãos que a vida me presenteou, Renan (Ree), Pedros (PM, Xampa e Cirilo), Anderson (Sonson), Felipes (Reis e Joa), Gabriel (Biela) e Victor (Vitoka), vocês são a minha segunda família e um dos meus mais preciosos tesouros guardados no fundo do coração. Devo a vida a vocês.

À minha namorada e companheira Ana Carolina, que continua a ser o mais lindo presente que Deus me enviou, de forma leve e doce. Obrigado por dividir bons momentos da vida comigo sendo além de minha parceira e companhia favorita, minha melhor amiga. Também, ao meu sogro, sogra e cunhado, Wagner, Cláudia e Matheus por cada sorriso, risada e parceria

À CAPES, ao Programa de Pós-graduação em Biotecnologia do Instituto de Biociências de Botucatu – IBB (**33004064087P8**) e a FAPESP (**Processos 2014/22689-3, 2019/09735-0, 2021/11291-2)** pelo imprescindível suporte acadêmico e financeiro para que a realização deste trabalho fosse viável.

Àqueles que contribuíram de forma direta ou indireta com este estudo.

Abbreviation Index

ANOVA – Analysis of Variance

CAD – Computer-Aided Design

CAM – Computer-Aided Manufacturing

CV – Crystal Violet

DI – Deionized Water

DTA – Differential Thermal Analysis

EDS – Energy Dispersive X-ray Scattering

ECM – Extracellular Matrix

FDM – Fused Deposition Modeling

MWCNT – Multi-Walled Carbon Nanotubes

FTIR – Fourier Transform Infrared

MTT - Mitochondrial Dehydrogenase Enzymatic

nHA – hydroxyapatite nanoparticles

PBS – Phosphate Buffer Saline

TGA – Thermogravimetry Analysis

SEM – Scanning Electron Microscopy

Figure Index

Summary

RESUMO

Este estudo apresenta o desenvolvimento e caracterização de um hidrogel de quitosana injetável, livre de células, reforçado com nanotubos de carbono de paredes múltiplas (MWCNT) e nanopartículas de hidroxiapatita (nHA) para aplicação em engenharia de tecido ósseo. O hidrogel visa melhorar as propriedades mecânicas, biocompatibilidade e osteocondutividade, oferecendo uma solução potencial para a regeneração óssea. A funcionalização dos MWCNTs foi realizada por meio de um ataque ácido assistido por banho ultrassônico, aumentando significativamente a carga de superfície e reduzindo o tamanho das partículas. Este processo garantiu melhor interação com a matriz de quitosana, prevenindo a floculação e promovendo a formação uniforme do hidrogel. A Espectroscopia de Infravermelho por Transformada de Fourier (FTIR) confirmou a incorporação bem-sucedida de grupos funcionais da quitosana, MWCNT e nHA, indicando a integração eficaz dos materiais. A estabilidade física e química dos hidrogéis foi avaliada por meio de testes de intumescimento e degradação. Os hidrogéis exibiram propriedades de intumescimento significativas e taxas de degradação controladas em água deionizada e solução salina tamponada com fosfato (PBS), essenciais para manter a integridade estrutural enquanto suportam o crescimento celular. A análise termogravimétrica (TGA/DTA) demonstrou ainda a estabilidade térmica do hidrogel, confirmando sua adequação para aplicações biomédicas. As análises morfológicas e elementares, utilizando Microscopia Eletrônica de Varredura (SEM) e Espectroscopia de Dispersão de Energia (EDS), revelaram uma estrutura porosa bem definida e a presença de cálcio e fósforo, indicando a integração bem-sucedida da nHA na matriz do hidrogel. Essas características são cruciais para mimetizar o ambiente ósseo natural e promover a adesão e proliferação celular. A biocompatibilidade foi avaliada por meio de testes de citotoxicidade e adesão celular utilizando pré-osteoblastos MC3T3-E1. Os resultados mostraram alta viabilidade celular e forte adesão, destacando o potencial do hidrogel para suportar a atividade dos osteoblastos e a regeneração do tecido ósseo. A viabilidade celular foi mantida acima do limiar definido pelas diretrizes ISO 10993-5, confirmando a segurança do material para uso biomédico. A análise da expressão gênica, utilizando a Reação em Cadeia da Polimerase Quantitativa por Transcrição Reversa (RT-qPCR), monitorou a expressão de marcadores osteogênicos chave, incluindo Alp, Tgf-β2, Runx2, Opn, Bglap e Col1a1. A análise demonstrou a regulação positiva desses marcadores, indicando que o hidrogel promove a diferenciação dos osteoblastos e a remodelação da matriz extracelular, processos essenciais para a regeneração óssea eficaz. A atividade das metaloproteinases de matriz (MMP), crucial para a remodelação da matriz extracelular, foi avaliada por ensaios de zimografia. Os resultados mostraram MMPs ativas, particularmente MMP-2 e MMP-9, no ambiente do hidrogel, apoiando a remodelação dinâmica necessária para a regeneração do tecido ósseo. Em conclusão, o hidrogel de quitosana desenvolvido, reforçado com MWCNT e nHA, apresenta propriedades promissoras para aplicações em engenharia de tecido ósseo. Sua robustez mecânica, biocompatibilidade e osteocondutividade fazem dele um candidato viável para uso clínico na regeneração óssea. Este hidrogel oferece uma

nova abordagem para o tratamento de lesões e condições relacionadas ao osso, potencialmente melhorando os resultados dos pacientes por meio da reparação e regeneração óssea aprimoradas. A avaliação abrangente de suas propriedades sugere que este hidrogel pode efetivamente suportar a atividade dos osteoblastos e facilitar o complexo processo de remodelação do tecido ósseo, marcando um avanço significativo no campo da medicina regenerativa e engenharia de tecidos.

Palavras-chave: biomateriais, medicina regenerativa, biotinta, bioimpressão 3D, engenharia de tecidos, quitosana, hidroxiapatita, nanotubos de carbono.

ABSTRACT

This study presents the development and characterization of a cell-free chitosan hydrogel reinforced with multi-walled carbon nanotubes (MWCNT) and hydroxyapatite nanoparticles (nHA) for application in bone tissue engineering. The hydrogel aims to enhance mechanical properties, biocompatibility, and osteoconductivity, providing a potential solution for bone regeneration. The functionalization of MWCNT was achieved through an acid attack assisted by an ultrasonic bath, significantly increasing the surface charge and reducing particle size. This process ensured better interaction with the chitosan matrix, preventing flocculation and promoting uniform hydrogel formation. Fourier Transformed Infrared Spectroscopy (FTIR) confirmed the successful incorporation of functional groups from chitosan, MWCNT, and nHA, indicating effective material integration. Physical and chemical stability of the hydrogels was assessed through swelling and degradation tests. The hydrogels exhibited significant swelling properties and controlled degradation rates in both deionized water and phosphate-buffered saline (PBS), essential for maintaining structural integrity while supporting cell growth. Thermogravimetric analysis (TGA/DTA) further demonstrated the hydrogel's thermal stability, confirming its suitability for biomedical applications. Morphological and elemental analyses using Scanning Electron Microscopy (SEM) and Energy Dispersive Spectroscopy (EDS) revealed a well-defined porous structure and the presence of calcium and phosphorus, indicative of successful nHA integration into the hydrogel matrix. These characteristics are crucial for mimicking the natural bone environment and promoting cell attachment and proliferation. Biocompatibility was evaluated through cytotoxicity and cell adhesion tests using MC3T3-E1 pre-osteoblasts. The results showed high cell viability and strong adhesion, highlighting the hydrogel's potential to support osteoblast activity and bone tissue regeneration. The cell viability was maintained above the threshold defined by ISO 10993-5 guidelines, confirming the material's safety for biomedical use. Gene expression analysis using Reverse Transcription-quantitative Polymerase Chain Reaction (RT-qPCR) monitored the expression of key osteogenic markers, including Alp, Tgf-β2, Runx2, Opn, Bglap, and Col1a1. The analysis demonstrated the upregulation of these markers, indicating that the hydrogel promotes osteoblast differentiation and extracellular matrix (ECM) remodeling, essential processes for effective bone regeneration. Matrix metalloproteinase (MMP) activity, crucial for extracellular matrix remodeling, was assessed using zymography assays. The results showed active MMPs within the hydrogel environment, particularly MMP-2 and MMP-9, supporting the dynamic remodeling required for bone tissue regeneration. In conclusion, the developed chitosan hydrogel reinforced with MWCNT and nHA exhibits promising properties for bone tissue engineering applications. Its mechanical robustness, biocompatibility, and osteoconductivity make it a viable candidate for clinical use in bone regeneration. This hydrogel provides a new avenue for treating bone-related injuries and conditions, potentially improving patient outcomes through enhanced bone repair and regeneration. The comprehensive evaluation of its properties suggests that this hydrogel can effectively support osteoblast activity and facilitate the complex process of bone

tissue remodeling, marking a significant advancement in the field of regenerative medicine and tissue engineering.

Keywords: biomaterials, regenerative medicine, bio-ink, 3D bioprinting, tissue engineering, chitosan, hydroxyapatite, carbon nanotubes.

1. INTRODUCTION

1.1 Bone Structure and Physiology

The human skeletal system is a dynamic organ comprising about 200 bones that provide structural support and protection to vital organs, facilitate movement, store minerals, and house bone marrow for hematopoiesis (HART et al., 2020; OLIVEIRA; LEEUWENBURGH; MANO, 2021). Bone injuries, categorized as critical or non-critical, pose a significant clinical challenge due to their varying requirements for repair and regeneration. Non-critical injuries, such as simple fractures, typically heal through the body's natural reparative processes, while critical injuries, like large bone defects, may not heal adequately without intervention (GEMINI-PIPERNI et al., 2014). A deeper understanding of bone structure and physiology, including the roles of differentiation and ECM remodeling gene markers, is essential for developing effective treatments.

Two main categories divide the bone tissue, which are the macroscopic and microscopic. Subidiving the macroscopic organization, we have the cortical and trabecular bones. The first comprehend the dense outer layer forms approximately 80% of the skeletal mass and provides mechanical strength, particularly in weight-bearing bones. Cortical bone is organized into osteons, or Haversian systems, cylindrical structures aligned with the bone's longitudinal axis, enabling resistance to compressive forces (HART et al., 2020). The second is localized predominantly at the ends of long bones, and within the vertebrae, trabecular bone has a porous architecture that reduces weight while maintaining structural integrity. Its mesh-like network of trabeculae is vital for the absorption and distribution of mechanical loads and serves as a critical site for hematopoiesis due to its housing of red bone marrow (TOMASZEWSKA et al., 2021). Besides, the cell organization in bone tissues is very dynamic, containing highly specialized matrices that work together to maintain bone integrity and function.

Histologically, three specific cell types constitute bone, as follows: **1.** Osteoblasts, mesenchymal-derived cells that actively participate in the synthesis of the bone matrix by producing organic components and subsequently mineralizing them (BOSKEY; ROBEY, 2019) – osteoblasts an essential role during bone tissue regeneration and because that proper relevance has been highlighted this cell during bone engineering; **2.** Osteoclasts

are hematological-derived cells that become multinucleated during osteoclastogenesis in response to RANKL and MCSF. Osteoclasts perform the opposite function to osteoblasts, as they break down the bone matrix for mineral and protein reabsorption (BOSKEY; ROBEY, 2019); and **3.** Osteocytes, osteoblast-derived cells embedded in the mineralized bone matrix and responsible for orchestrating bone remodeling, also serve as relevant reserves of RANKL (BOSKEY; ROBEY, 2019), as illustrated below in **Figure 1:**

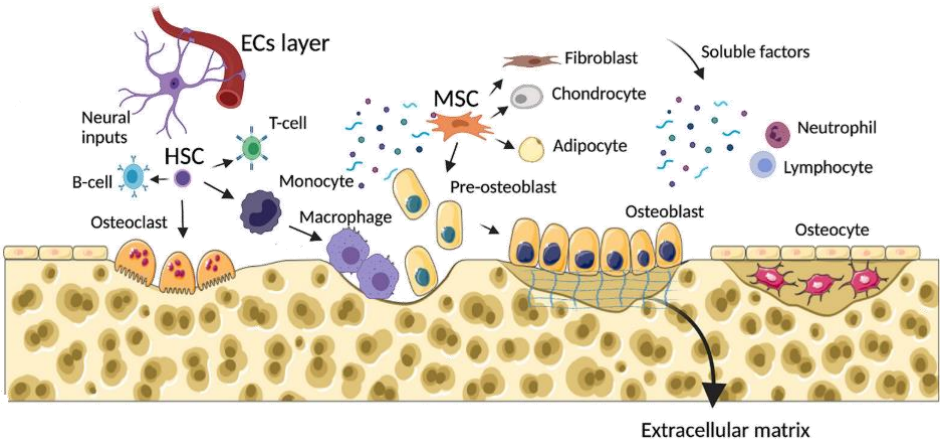

Figure 1: Example of the microenvironment of bone tissue regarding different hierarchical cell sources and their respective differentiation and orchestration. (Taken and adapted from OLIVEIRA; LEEUWENBURGH; MANO, 2021)

Thus, it is essential to consider biological events such as cell adhesion, proliferation, and differentiation in the complex organization of bone tissue to design a bio-ink that adequately mimics the desired environmental features of native tissue.

Cell adhesion is currently a well-studied event in normal physiological processes, pathological conditions, and/or other cell-cell and cell-matrix interactions (OKEGAWA et al., 2004). The components governing cell adhesion contribute decisively to regulating cell differentiation, proliferation, and death. Therefore, proper cell adhesion and subsequent integration with the host tissue are crucial for homeostasis maintenance. Over the last decades, our research group has investigated cell-material interaction to map biomarkers to better comprehend this biological and essential step during bone regeneration, also because it can guide researchers to have previsibility during novel material's propositions. For instance, we showed that within the first 2 hours of adhesion, physiological osteoblast adaptation culminates in different signaling pathways responsible for cytoskeleton rearrangement, with signals triggered from the activation of

proteins such as MAPKp38 and FAK (ZAMBUZZI et al., 2009) and it is finely modulated when those cells are adapted on ceramic or metallic materials (FERNANDES et al., 2023; DE ALMEIDA et al., 2024; FERNANDES et al., 2023; GOMES et al., 2023). In this scenario, we have gained experience also demonstrating cell signaling during osteoblast adhesion, showing that reactive oxygen species (ROS) modulates the action of protein tyrosine phosphatases (PTPs) during cellular mechanisms involved in osteoblast adhesion, and it needs to be considered during predictable biomaterial development (FERNANDES et al., 2014). Our research group's investigation of the adhesion transition to the proliferative metabolism of osteoblasts showed significant findings that brought light to understanding the entrance to differentiation metabolism.

As mentioned earlier, once injured, bone tissue undergoes a healing process that can occur through two distinct mechanisms: repair and regeneration. Regeneration occurs when the damaged tissue is repopulated based on the proliferation and differentiation of the original tissue's cells. Consequently, the regenerated tissue should have the same functional and morphological properties as the native tissue. On the other hand, in the repair process, the damaged tissue is sometimes replaced by fibrous connective tissue, resulting in a collagen scar, and it leads to a loss of the original characteristics and functions and bone regeneration is considered a priority over repair in trauma cases, thus restoring the bone's original shape and functions (ZAMBUZZI et al., 2011a, 2011b). The process of bone regeneration comprises distinct stages that may assemble, including inflammation, hard callus formation, and other remodeling processes (KALFAS, 2001). Non-critical injuries, such as minor fractures or small bone defects, typically heal naturally through the bone's intrinsic repair mechanisms. Monitoring markers like alkaline phosphatase (ALP) and osteocalcin (BGLAP) are essential in assessing the healing progression in non-critical injuries (KARSENTY, 2017; NAKAMURA et al., 2020; VIMALRAJ, 2020). Meanwhile, critical bone injuries, such as segmental bone defects or comminuted fractures, pose a significant challenge due to the extensive bone loss or severe damage that the body's natural processes cannot adequately repair. These injuries, such as grafts or biomaterials, require external intervention to facilitate healing. Then, it often necessitates monitoring gene markers such as BMP-2, RUNX2, and other essential genes regarding the remodeling of bone inorganic crystal deposition involved in bone cell proliferation, osteogenic differentiation, and extracellular matrix (ECM)

remodeling activities (BERGERON et al., 2007; CARREIRA et al., 2014; HALLORAN; DURBANO; NOHE, 2020; RAIS et al., 2023).

Proliferation of bone cells, particularly osteoprogenitor cells, is the foundational step in bone repair and regeneration. This early stage involves the rapid expansion of progenitor cells to ensure a sufficient supply of osteoblasts for subsequent differentiation and matrix production (LI et al., 2019). It highlights the importance of controlled proliferation by regulating several key gene markers involved in cell cycle progression and cellular adhesion. The cyclin-dependent kinases (CDKs) are central regulators of the cell cycle, driving the transition from the G1 phase to the S phase. Together with their respective cyclins, CDK2, CDK4, and CDK6 phosphorylate the retinoblastoma protein (Rb), releasing E2F transcription factors that promote DNA replication and cell proliferation . Proper regulation of these CDKs is essential for ensuring controlled proliferation, which could lead to aberrant tissue formation (AMANI et al., 2021; ASGHAR et al., 2022; MACHADO et al., 2019; WESTON; BARR, 2023). Also, we have the p15 gene marker, a cyclin-dependent kinase inhibitor that binds to and inhibits CDK4 and CDK6, preventing excessive proliferation by blocking cell cycle progression at the G1 phase. Such inhibition is crucial for maintaining a balance between cell proliferation and differentiation during bone healing (AMANI et al., 2021; PAN et al., 2010). Another important marker for bone cell proliferation is focal adhesion kinase (FAK), a non-receptor tyrosine-kinase that mediates cell adhesion, migration, and proliferation. It plays a pivotal role in the initial phase of bone healing by promoting the adhesion and proliferation of osteoprogenitor cells at the injury site. FAK signaling pathways are activated in response to integrin engagement and mechanical stress, facilitating cellular proliferation and tissue repair (FÅHRAEUS; P.LANE, 1999; MISHRA; MANAVATHI, 2021).

Following proliferation, the differentiation of osteoprogenitor cells into mature osteoblasts is critical for bone formation. The expression of osteogenic proteins and matrix components regulates several genes such as RUNX2, BGLAP, osteopontin, Tissue Growth Factor Beta 2 (TGF-β2), COL1A1, and alkaline phosphatase (ALP), which are pivotal in differentiating osteoblasts from precursor cells. ALP is an early osteoblast differentiation marker crucial for the mineralization process. ALP hydrolyzes phosphate esters, increasing local concentrations of inorganic phosphate, which combines with

calcium to form hydroxyapatite crystals in the bone matrix. Elevated ALP activity indicates active bone formation, commonly used as a marker for osteogenic differentiation (BERGERON et al., 2007; LI et al., 2019; MYGIND et al., 2007). TGF-β2 is a multifunctional growth factor that regulates both proliferation and differentiation of osteoprogenitor cells. TGF-β2 promotes the synthesis of collagen and other matrix proteins and modulates the expression of key osteogenic markers like RUNX2, thereby enhancing osteoblast differentiation and bone formation (ELDRED et al., 2012; LI et al., 2022; TOWNSEND et al., 2011). RUNX2 controls the expression of many osteogenic genes, including the ALP, COL1A1, and BGLAP. RUNX2 activity is essential for the maturation of osteoprogenitor cells into functional osteoblasts and is a critical determinant of bone formation capacity (GOMATHI et al., 2020; KOMORI, 2010; LIU et al., 2021; WAGLEY et al., 2020). COL1A1 is the primary component of the organic bone matrix, and type I collagen provides a scaffold for mineral deposition and structural support. COL1A1 expression is upregulated during osteoblast differentiation, facilitating the production of a collagenous matrix critical for bone strength and integrity (KOMORI, 2019). Meanwhile, BGLAP works as a late marker of osteoblast differentiation that regulates bone mineralization, which binds to hydroxyapatite and calcium ions in the bone matrix, contributing to the stabilization and maturation of newly formed bone (KARSENTY, 2017; KARSENTY; FERRON, 2012). Another important gene to monitor is osteopontin, a non-collagenous glycoprotein that promotes cell adhesion, migration, and mineralization (NAKAMURA et al., 2020). Osteopontin is involved in both the initial and later stages of bone formation, facilitating the attachment of osteoblasts to the matrix and contributing to ECM organization.

Regarding the activity of ECM during the bone healing process involving the breakdown of damaged matrix components and the deposition of new ones, other important genes, such as Matrix metalloproteinases 2 and 9 (MMP-2 and -9), Bone Sialoprotein (BSP), Tissue Inhibitors of Metalloproteinases 1 and 2 (TIMP-1 and -2), and Bone Morphogenetic Protein 2 (BMP-2) are critical in its remodeling. MMP-2 and -9 enzymes degrade collagen and other ECM components, allowing for matrix turnover and remodeling. MMP-2 and MMP-9 are particularly important during the early phases of bone healing, where they help clear damaged tissue and create space for new bone formation (CHEN et al., 2021; ELDRED et al., 2012; LA ROCCA et al., 2004; PEETERS-JORIS; HAMMANI; SINGER, 1998; PUCCI-MINAFRA et al., 2001). On

the other hand, TIMP-1 and -2 balance their activity to prevent excessive matrix degradation (JANSEN et al., 2006; LI; TAY; YIU, 2020; SHIBUTANI et al., 1999; XI et al., 2020), while BSP nucleates hydroxyapatite crystals and the mineralization of the bone matrix, which is highly expressed in areas of active bone remodeling and is essential for proper matrix organization and mineralization (BARTHELEMI et al., 2012; CHAVEZ et al., 2023; HUNTER; GOLDBERG, 1993). Last, BMP-2 is a potent osteogenic factor promoting osteoblast differentiation and ECM synthesis. BMP-2 stimulates the production of collagen and other matrix proteins and enhances mineral deposition, making it a key player in bone regeneration and repair (CARREIRA et al., 2014; HALLORAN; DURBANO; NOHE, 2020; PARK et al., 2020; ZHANG et al., 2018). All of them facilitate the reorganization of the ECM, a necessary step for new bone formation, ensuring a balance between matrix degradation. Monitoring these markers provides insights into the remodeling phase of bone repair and is vital for developing therapeutic interventions.

Often, to improve the healing of bone tissues and recover their natural physiology and functions, surgeons use bone autologous grafts collected from the patient's bones to avoid rejection problems. Although such a strategy is fundamental in daily medical procedures and considered the gold standard, doctors cannot collect significant amounts for grafting critical bony lesions. Then, using natural or synthetic scaffolds in therapeutic interventions plays a crucial role in offering medically feasible routes and improving patient recovery. Natural scaffolds are derived from biocompatible and biodegradable materials like collagen, chitosan, and hyaluronic acid, which provide a favorable environment for cellular functions and facilitate tissue integration. Natural scaffolds can be combined with growth factors and other bioactive molecules to enhance bone regeneration further, while synthetic scaffolds provide structural support and promote cell attachment, proliferation, and differentiation. They combine synthetic materials such as hydroxyapatite, tricalcium phosphate, bioactive glass, and carbon-based materials with many polymer options (i.e., hydrogel-based composites) to create osteoconductive/osteoinductive environments that encourage new bone formation. Therefore, developing new biomaterial synthesis routes is crucial as they can orchestrate active biomolecules derived from different cell types, integrating a biological response that favors tissue regenerative mechanisms and looking for recapitulating the desired bone microenvironment to host osteoprogenitor cells.

1.2 The Bone Microenvironment Recapitulation by Hydrogel-based Biomaterials

The recovery of bone injuries through biomaterials as a cell-laden 3D scaffold encompasses different factors. For example, the stimulation of recruitment and action of new cells whose properties enable them to participate in bone tissue remodeling is of paramount relevance. These cells must also be able to communicate with each other through signaling mechanisms to provide greater integration and dynamism to the new tissue, where bioactive molecules are essential to drive this process (KOHLI et al., 2018; ZAMBUZZI; MILANI; TETI, 2010). Furthermore, biomaterial composites must form biocompatible support matrices whose supporting purpose is fulfilled concomitantly with their mechanical properties and incorporating those signaling molecules and other biochemical cues. In terms of biomaterials for bone regeneration purposes, one of the most used compounds in bone tissue bioengineering, easy to reproduce at the benchtop, and that meets the necessary mineral features is hydroxyapatite (nHA) [$Ca_{10}(PO_4)_6(OH)_2$] (HARUN et al., 2018; LI et al., 2020a; MAVROPOULOS et al., 2012). It is a significant component in the inorganic portion of bones, which can be obtained by chemical synthesis with a mineral phase analogous to that naturally found in the human body and with other different degrees of crystallinity (or maturation, commonly referred to in bone tissue studies) (HE et al., 2017). Several biomaterial routes are designed using nanotechnology approaches to explore how to tailor the compounds of interest, such as active biomolecules, within the scaffold matrix. The compound tailoring for recapitulating bone microenvironment has improved with the state-of-the-art additive manufacturing technology, using hydrogel-tailored composites called bio-inks. Bio-inks are extrudable biomaterials, cell-laden or not, combined for mimetic orchestration of native injured tissue, using 3D printers that precisely control the material deposition, customizing to fit the lesioned area (DAI et al., 2020b; PRAMANIK et al., 2009; RAMESH; MORATTI; DIAS, 2018; WENZ et al., 2016, 2017). Then, bio-inks are an excellent example of how biomaterials can rapidly take the desired form of recapitulated bone microenvironment using cutting-edge nanotechnology, as depicted below in **Figure 2**:

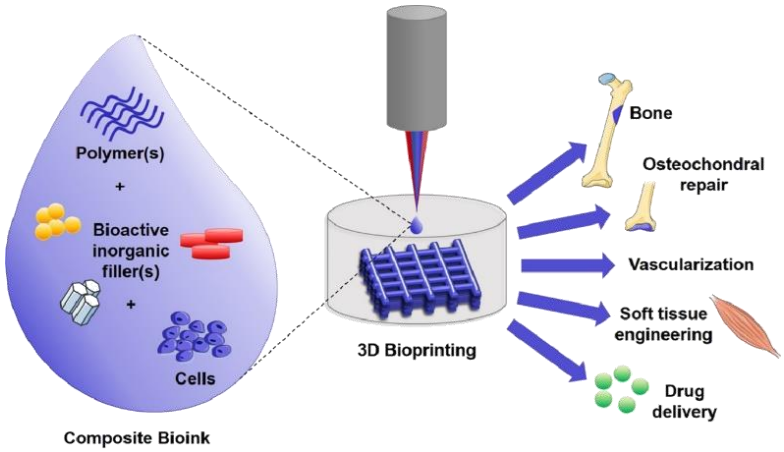

Figure 2: A general scaffold orchestration scheme to achieve a biomimetic bio-ink for bone tissue regeneration (Fully taken from HEID; BOCCACCINI, 2020).

From the materials science standpoint, nanotechnology combines different areas of knowledge to solve quotidian issues whose applications at the nanoscale reveal highly innovative and functional properties. The combination of tunable properties in nanomaterials allows their participation in biological pathways with greater efficiency due to the wide range of possible physicochemical modifications, including the distinct signaling pathways already investigated in bone tissue regeneration (GUNGOR-OZKERIM et al., 2018; TOH et al., 2014). In this context, establishing a biomaterial synthesis and ideal formulation for bone injuries should rely on a well-established relationship between nanomaterials-based biomaterials and osteointegration, attempting to build the recapitulation of the bone microenvironment to improve adhesion, proliferation, and migration of osteogenic cells (GRIFFIN et al., 2016). Therefore, developing osseointegrated nanocomposites focuses on obtaining these properties to achieve results comparable to the gold standard protocol for bone repair and regeneration, autologous grafting (KOHLI et al., 2018).

Considering the interaction between a biomaterial, such as a new potential bio-ink, and the host bone microenvironment after surgery, osteointegration can occur either fully or partially. In other words, the synthesis, characterization, and application of biomaterials in bone lesions should aim to stimulate the replacement capacity of these structures by the original tissue, resulting in similar anatomical and functional characteristics. Therefore, a potential bio-ink should promote mechanical and regenerative properties that correlate with these levels of integration. Understanding the

interface between the scaffold surface and the necessary physicochemical modifications to improve cell survival and differentiation is the key to achieving such a goal. This adaptation allows further analysis of the activation of cellular signaling mechanisms responsible for the cellular machinery of osteointegration: cell adhesion, adaptation, proliferation, and differentiation with balanced activity of extracellular matrix (ECM) remodeling, as well as the investigation of inflammatory pathways, to potentially serve as cell-laden scaffolds for the growth of new adjacent tissue. In summary, most biomaterial development approaches must aim to achieve mechanical, controlled degradation, short-term swelling rate, and injectability using the reinforcement of chitosan as a hydrogel polymer matrix. Considering these features, we designed our biomaterial blend using a hydrogel chemical tailoring approach by reinforcing the chitosan polymer with hydroxyapatite nanoparticles (nHA) and multi-walled carbon nanotubes (MWCNT) in order to form a close biomimetic structure of bone microenvironment.

1.3 Chitosan-reinforced Hydrogels and its Applications in Bone Tissue Engineering

Many material combinations have been proposed to trigger bioactivity signaling in osteoblasts gathering polymers and organic or inorganic fillers. Regarding polymers, chitosan obtainment occurs through total or partial deacetylation of chitin (a nitrogen-rich polysaccharide) under alkaline conditions, an abundant biopolymer exoskeleton of crustaceans and other invertebrates. Polysaccharides, in general, are highly regarded as biomimetic structural materials due to their similarity to the ones found in the ECM of natural tissues (CARROW; GAHARWAR, 2015; DEMIRTAŞ; IRMAK; GÜMÜŞDERELIOĞLU, 2017). Chitosan is widely used as a support agent in the form of dry-porous matrices or hydrogels in tissue engineering, although it is considered a challenge for hydrogel application due to the necessity to use low pH conditions to solubilize it, which is harmfully for cells. In addition to enabling various processing methods, chitosan is considered to have low toxicity and intrinsic antibacterial properties (RAMESH; MORATTI; DIAS, 2017).

Modifications are typically performed on the chitosan surface using hydroxyapatite crystals and vice-versa through the protonated amine groups on the polysaccharide chain for bone tissue applications and even as a drug carrier for cancer

treatment (MARTINS et al., 2014, 2020c). In vitro studies with bone marrow stromal undifferentiated cells have shown excellent adhesion issues and reflected cell viability and proliferation when combined with hydroxyapatite and chitosan through covalent bonds between hydroxyl (-OH) and amine ($-NH_2$) groups. The use of hydroxyapatite ranges from either crystalline or non-crystalline phases (RODRIGUES; SILVA; MALAFAYA, 2006) when carbonate substitution occurs within the crystal structure, for instance, and it exhibits an amorphous character (ANNA, 2005). Regarding bioprinting, several works demonstrate that chitosan has the desired features, such as thermal and pH-sensitive gelation shear-thinning behavior in its rheology when modified with hydroxyapatite and applied for bone tissue regeneration. (ASHAMMAKHI et al., 2019; DEMIRTAŞ; IRMAK; GÜMÜŞDERELIOĞLU, 2017). However, chitosan polymer alone presents poor mechanical strength, and combining it with other polymers or inorganic fillers is necessary to overcome this issue (KOHLI et al., 2018; NAZEER et al., 2020; SADAT-SHOJAI et al., 2013; SADEGHIANMARYAN et al., 2022). Next, **Table 1** highlights the main strategies reported to improve the mechanical properties of chitosan hydrogels, including hydroxyapatite:

Table 1: Reported Reinforcement Strategies of Chitosan Hydrogels for Bone Tissue Engineering

Chitosan Reinforcement Strategy	Used Cell Lines	References
Hydroxyapatite	MSCs	LAZARIDOU et al., 2022
Alginate	Osteoblasts	DEMIRTAS et al., 2017
Gelatin	(MC3T3-E1)	NG, W.L et al., 2016
Graphene Oxide	BMSCs	AHMED et al. 2020
PCL	BMMSCs	DONG et al., 2017
Nanocelullose	MC3T3-E1	MATURAVONGSADIT et al., 2021
PVA + Bioactive Glass	MG-63	BIGLARI et al., 2024
Silk Fibroin	NIH/3T3	KIM et al., 2018
Polyethylene Glycol (PEG)	NIH/3T3	PILUSO et al., 2021
Hydroxyapatite (nHA) + Multi-walled Carbon Nanotubes (MWCNT)	hFOB	SANCHEZ et al., 2021
Poly-ε-caprolactone (PCL) + MWCNT	HDPSCs	FLORES-CEDILLO et al., 2016
β-Glycerophosphate + MWCNT	MG-63	GHOLIZADEH et al., 2017

Although hydroxyapatite nanoparticles (nHA) are known to be osteogenic and osteoconductive, their fragile nature hinders their fabrication in various shapes and sizes (OJEDA et al., 2022). Additionally, the association of hydroxyapatite and biodegradable polymers allows the production of materials and hydrogels with differential properties, such as gels or films, without requiring hydroxyapatite to undergo thermal treatments for grain growth. Hydroxyapatite remains one of the leading biomaterials used in tissue engineering as an interesting coating compound, mimicking the ideal conditions to replicate the mineralization portion of bone tissue. One of the main advantages of using hydroxyapatite nanoparticles in tissue engineering is the ease of synthesis, although it

alone cannot significantly improve the hydrogel mechanical properties for long periods. Then, combining chitosan polymer with inorganic fillers in the same biomaterial blend, such as carbon nanotubes and hydroxyapatite, is a promising strategy for hydrogel reinforcement in tissue engineering approaches.

Carbon nanotubes (CNTs) are allotropes of carbon with a cylindrical morphology. They are categorized as single-walled nanotubes (SWNTs) and multi-walled nanotubes (MWNTs) (ŢUCUREANU et al., 2016). Carbon-based structures are lightweight and robust and can be formulated to incorporate nanoscale components of bone, such as hydroxyapatite and collagen, in the production of biomaterials (SAHITHI et al., 2010). Substrates based on carbon nanotubes have shown the growth of osteoblastic cells (TUTAK et al., 2009). Carbon nanotubes are non-biodegradable, acting as an inert matrix to inflammatory responses or participating positively in signaling pathways, where cells can proliferate and deposit new bioactive materials (DU et al., 2013). The modification to these structures generally occurs through an acidic attack assisted by ultrasonication depositing functional groups on their surface (PEDROSA et al., 2010). Also, these processes remove impurities from the nanotubes and reduce their length, creating defects in the side walls of the functionalized carbon nanotubes. After functionalizing them, various functional groups are present at their ends or specific reactive sites along the carbon backbone, with carboxylic acid and hydroxyl groups being the most common (O'CONNELL, 2006). Therefore, carbon nanotubes are an option as a modifying agent for chitosan, which could form a polymeric-reinforced network with high cell adhesion and proliferation capacity.

Taking the adhesion phenomenon to functional groups present in carbon nanotubes, an interesting study using carbonic self-assembled monolayers functionalized with OH, COOH, and CH_3 investigated the cell integrin proteins' ability to bind, revealing that this process occurs efficiently following the order $OH>COOH=NH_2>CH_3$ (KESELOWSKY; GARCÍA, 2004). Therefore, an approach where MWCNT functionalized with those used to reinforce polymers has a high potential for synthesis through covalent interactions such as hydrogen bonds, hydrophobic non-covalent wrapping, or electrostatic interactions between protonated amine and carboxyl groups. However, its concentration can induce high levels of cytotoxicity in bone cells in high concentrations. Several authors detected remarkable differences using very low doses of MWCNT, which treated different types of cells, varying concentrations from 5 μg/mL to

3000 µg/mL (ZHAO; LIU, 2012). The abovementioned functionalization routes, including MWCNT size, shape, and surface charges, are crucial in cell response outcome, where its modification in polymer-based compounds and their use as modifier agents must occur safely (KYRIAKIDOU et al., 2020). Actually, it is one of the challenges of using carbon nanotubes for tissue engineering due to the necessity of using considerable MWCNT concentration for polymer-reinforcement strategies, although several authors reported doing so, as described below.

Recently, many studies reported the combination of chitosan, nHA, and MWCNT in tissue engineering for bone tissue application, achieving well-developed biomaterials with interesting properties, such as mechanical, porosity, water uptake, controlled morphology, and satisfactory cell viability features. The main reasons to gather these compounds are increasing the mechanical properties to overcome chitosan's fast degradability, considering as a strategy the recapitulation of the bone microenvironment also promoted by nHA mineralization, necessary to improve cell accommodation (CHEN et al., 2013; CHEW et al., 2011; DAI et al., 2020a; JIAN et al., 2023; LI et al., 2020a, 2020b; RAHMAN et al., 2024; RATH et al., 2012b; SANCHEZ et al., 2021; TÜRK et al., 2018; VENKATESAN et al., 2011). However, to the best of our knowledge, no direct attention was paid to the literature regarding how byproducts released by reinforced chitosan polymers with MWCNT and nHA combination influence cell responses. All the abovementioned works reported important data regarding some *in vivo* and *in vitro* applications, although they do not go deep into hydrogel network formation and gene expression to study cell machinery investigation. To be used as a scaffold for bone tissue regeneration, any degradation events that generate byproducts from compounds present within a hydrogel formulation to cell culture medium must participate positively or be inert when challenged with cells. In this way, one of the most recommended guidelines used worldwide to standardize the test of promising biomaterials for potential medical applications regarding cytotoxicity is the International Standardization Organization (ISO) 10993-5.

1.4 The Limitation of Direct and Indirect Biomaterial Contact Tests for Cytotoxicity Screening

The ISO 10993-5 guideline is titled "*Biological evaluation of medical devices"* and is a regimental and standardized protocol used worldwide to test the preliminary cytotoxicity of a respective material ruled by the ISO and International Electrotechnical Commission (IEC) (INTERNATIONAL STANDARD ORGANIZATION, 2012). Many experiments in the ISO 10993-5 guideline are divided into a broad range of recommended tests to diffuse and homogenize the first necessary investigations before using materials for safe use, covering from agriculture to healthcare. Briefly, there are two ways to test the cytotoxicity of biomaterials intended to be used in further pre-clinical testing: indirect and direct contact methods using fluid extracts to treat a specific cell carpet monolayer, as displayed in **Figure 3:**

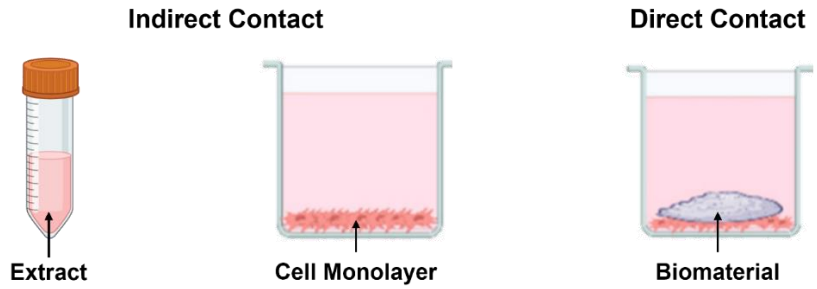

Figure 3: Representative indirect and direct contact test scheme preconized by ISO 10993-5 guideline for cytotoxicity evaluation (Adapted from KOVRLIJA et al., 2024 using BioRender® free version).

The indirect contact method is based on pre-conditioning the cell culture medium (extract) with a sterilized biomaterial for 24 h at 37° C. The ISO guideline recommends the ratios between the sample weight and extract. In such a test, only the cytotoxicity byproducts released from the biomaterial to the cell medium through chemical processes are evaluated. In contrast, the direct contact test surpasses the pre-conditioning step, and the solid/porous biomaterial is placed directly onto the cell monolayer. In this case, not only the influence of biomaterial's byproducts but also surface features (porosity and roughness), mechanical stress, and other factors. In both experiments, the biomaterial is considered non-cytotoxic if it allows for cell viability of at least 70% (CHRANIUK et al., 2022; INTERNATIONAL STANDARD ORGANIZATION, 2012; PRZEKORA, 2019). ISO 10993-5 intentionally remains open to the flexibility of some criteria accompanying science's fast technological development pace (GRUBER; NICKEL, 2023). A good example of the innovative approaches explored recently is using 3D scaffold models (bio-

inks) that provide enough spatial distribution of cells to recapitulate the physiological environment, and also the use of cell spheroids and organoids mirroring tissues or organs features (FRISCH et al., 2023). For instance, these combined approaches are applicable in many efforts to reduce the extensive use of animal models in toxicology drug screening using additive manufacturing and tissue engineering approaches (HUH et al., 2024).

1.5 Quarantine Protocol for Cell-free Bioink Screening (QP-BioScreen) Using Chitosan-MWCNT-nHA Hydrogels

Some authors cleverly pointed out some limitations during the ISO 10993-5 guideline execution, specifically in the indirect contact method regarding the presence of nHA and MWCNT compounds that could generate “false” cytotoxicity responses. Firstly, it is pointed out that different types and phases of calcium phosphate apatites and functionalized MWCNT highly adsorb ions and micronutrients from the environment, drastically changing cytotoxicity evaluation. Secondly, the indirect contact method is nothing similar to any physiological condition, even though it is considered an important and diffused gold standard procedure by ISO 10993-5 (GUO et al., 2008; GUSTAVSSON et al., 2011; KLIMEK et al., 2016; KOVRLIJA et al., 2024; ZHAO; LIU, 2012). On the other hand, many researchers report using pre-conditioning culture media by cells, similar to the medium conditioning of indirect contact found in ISO 10993-5 guideline, to improve biological responses. Either high secretome activity, protective and bioactive substances such as cytokines, chemokines, growth factors, hormones, and extracellular vesicles, or pharmacological stimuli influence address positive responses when treating target cells for regeneration purposes, including bone (GIULIANI et al., 2020; SMOLINSKÁ; BOHÁČ; DANIŠOVIČ, 2023; TOUANI et al., 2021). Therefore, two genuine questions emerge: **(i)** since the cell secretome after the pre-conditioning culture medium can positively influence cell machinery and signaling by releasing bioactive molecules, could the released byproducts of a cell-free bio-ink do the same?; **(ii)** Could monitoring bone cell machinery, such as mitochondrial activity, adhesion, differentiation, and ECM remodeling, along with monitoring bone scaffold synthesis parameters, assist the ISO 10993-5 guideline besides simply looking at cytotoxicity tests? Complete answers to these questions are quite challenging to achieve fully, although we investigated generous insights to address assistance in bringing light to them.

In this way, we present a bioengineered synthesis approach to chitosan hydrogel reinforcement using MWCNT and nHA cell-free bio-ink. Our design was conceived to recapitulate the bone microenvironment regarding its reproducibility, deeply looking at the cell viability, adhesion, and gene expression regarding differentiation and ECM remodeling using molecular biology based on the premises of ISO 10993-5 guidelines. To the best of our knowledge, works reported elsewhere regarding using chitosan, MWCNT, and nHA in hydrogel approaches, despite their successful *in vitro*/*in vivo* results, did not go beyond the indirect contact method to evaluate cell viability assays. Also, such an approach can be addressed to other scaffold development for tissue regeneration, improving a more assertive screening before moving to *in vivo* tests, reducing false *in vitro* non-cytotoxic results, and reducing animal models without need. Combining indirect contact test with RT-qPCR gene expression monitoring, the ***Quarantine Protocol for Cell-Free Bio-ink Screening (QP-BioScreen)*.** Such a protocol can be a more accurate screening test candidate for biomaterials before its application in 3D-bioprinting, where, after the screening is done, the same conditioned medium could be used to assist the cell machinery in improving its maturation to culture a 3D-cell-laden scaffold. The hypothetical configuration of the chitosan-reinforced hydrogel by MWCNT and nHA that mimetic the bone microenvironment is represented below in **Figure 4**:

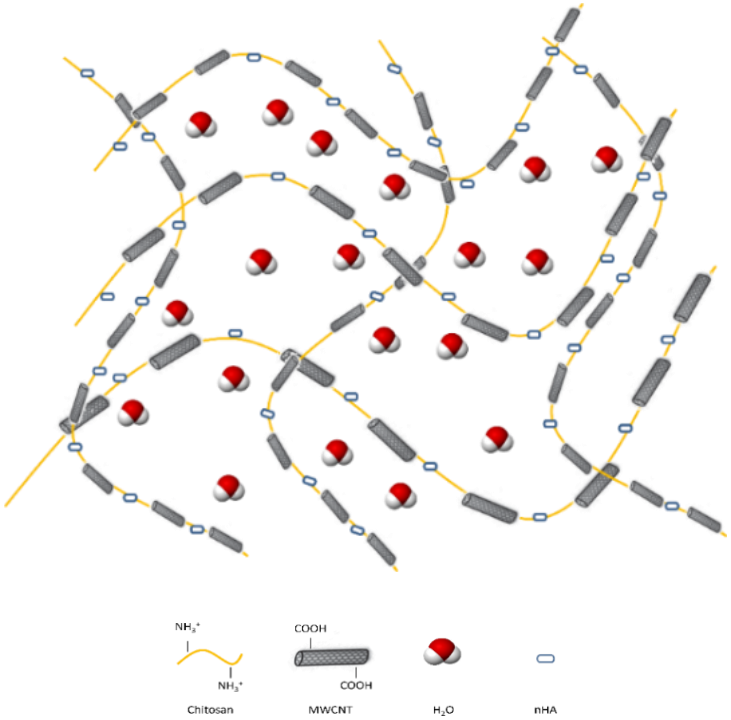

Figure 4: Scheme of our hypothetical bone *cell-free* hydrogel final configuration with adequate biological properties to promote adhesion, proliferation, and differentiation of bone cells.

1.6 Study Limitations

After paying much attention to describing the importance of the recapitulation of the bone microenvironment by a bone bio-ink, you might notice beyond this point that, unfortunately, we could not explore the feasibility of our hydrogel formulation into the 3D-bioprinting technique. The reasons concern the hydrogel formulation and infrastructure limitations we are still trying to overcome.

Regarding our hydrogel formulation approach, one of the main routes to chitosan hydrogel be used in 3D-bioprinting and achieve a proper *sol-gel* transition sensitivity at 37° C is through the use of β-glycerophosphate (DEMIRTAŞ; IRMAK; GÜMÜŞDERELIOĞLU, 2017; GHOLIZADEH et al., 2017). Besides the thermos-sensitivity, β-glycerophosphate is also used as a pH-neutralizing agent, drastically diminishing NaOH use and assisting in maintaining chitosan into a hydrogel form (DEMIRTAŞ; IRMAK; GÜMÜŞDERELIOĞLU, 2017). Using only NaOH, we experimentally observed that chitosan lost its viscosity feature, jeopardizing hydrogel configuration, which cannot be used in additive manufacturing approaches. When using β-glycerophosphate, the reported concentration elsewhere is about 62- 65% w/v for pure chitosan hydrogels. When synthesized using MWCNT as an inorganic filler to improve mechanical stability, β-glycerophosphate concentration is reduced by about 7.5% w/v (GHOLIZADEH et al., 2017). Since our hydrogel approach also has hydroxyapatite nanoparticles in its formulation, we investigated several β-glycerophosphate concentrations under 7.5% w/v, where lower concentration, the chitosan-MWCNT-nHA viscosity feature, was also lost. Although the use of β-glycerophosphate was unsuccessful, exhaustively extrusion tries using hydrogels only neutralized by NaOH were performed to develop a printability protocol to determine printing parameters. We faced poor-controlled extrusion and no long-term hydrogel stability (<7 days) when chitosan-MWCNT-nHA hydrogel was challenged using a cell culture medium.

Regarding the infrastructure limitations, our lab's available printer is unsuitable for bioprinting purposes and does not match our printing necessities. Although several attempts were made to adapt a Fused Deposition Modeling printer (FDM), it does not have a temperature controller for cell survivor maintenance (37° C) if embedded into the scaffold. Also, we have a space limitation in our shared-cell culture room to accommodate

the FDM printer in a sterile environment, which is one of the primary demands of working with bio-inks to avoid contamination. The PhD candidate learned these critical considerations during his studying abroad program at Wake Forest Institute for Regenerative Medicine (WFIRM) between 2022 and 2023, where more information regarding additive manufacturing training and developed projects is available in the Appendix Section. Thus, we focused on the abovementioned strategies to create a cell-free bio-ink screening using ISO 10933-5 guidelines and RT-qPCR while trying to solve these limitations.

2. OBJECTIVES

Develop cell-free bio-ink synthesis using chitosan hydrogels reinforced with multi-walled carbon nanotubes and hydroxyapatite nanoparticles, looking to offer a byproduct able to on pre-osteoblast cell machinery and further mineralization ability.

- **Specific aims:**

    1. Determination and optimizing the biomaterial synthesis parameters and formulation;
    2. Characterization of the reinforced scaffold analyzing its mechanism formation regarding vibrational, morphological, swelling, thermal, and injectability features;
    3. Evaluate the regular cell viability of pre-osteoblasts cell line using the chitosan-reinforced scaffolds following ISO 10993-5 guidelines using the indirect contact method;
    4. Investigate the gene expression of proliferation, differentiation, ECM remodeling, and mineralization index regarding pre-osteoblast cell treatment;

3. MATERIALS AND METHODS

3.1 Materials

(i) Hydrogel synthesis: Calcium chloride ($CaCl_2$, 76%) was obtained from Impex (Varginha, Minas Gerais, BRA), phosphoric acid (H_3PO_4.95%) from Dinâmica (Indaiatuba, São Paulo, BRA). Sodium hydroxide (NaOH, 100%), potassium bromide (KBr, 99%), acetic acid (CH_3COOH, 99%), nitric acid (HNO_3, 70%), sulfuric acid (H_2SO_4, 95% – 98%), chitosan (extracted from shrimp shells, ≥75% deacetylated), multi-walled carbon nanotubes (>98% carbon basis, OD × L = 6-13 nm × 2.5-20 μm), Phosphate Buffer Saline powder, (PBS, 10 mmol/L), and potassium bromide (KBr) were purchased from Sigma-Aldrich (St. Louis, Missouri, USA). **(ii)** Cell culture and colorimetric assay: The cell culture flasks were purchased from TPP (Trasadingen, Switzerland); Fetal bovine serum, MEM-α cell media, trypsin, and penicillin antibiotics were purchased from Vitrocell-Embriolife (Campinas, São Paulo, BRA). The β-Glycerophosphate, dexamethasone, and ascorbic acid, Alizarin Red S salt, tetrazolium salt 3-(4, 5-dimethylthiazol-2-yl)-2, 5-diphenyltetrazolium bromide (MTT), N-(4-(bis(4-(dimethylamino)phenyl)methylene)-2,5-cyclohexadien-1-ylidene)-N methylmethanaminium salt (Crystal Violet, CV) were purchased from Sigma-Aldrich (St. Louis, Missouri, USA). MC3T3-E1 subclone 4 immortalized cell line from mouse calvaria was purchased from the American Type Culture Collection (ATCC, Gaithersburg, Maryland, USA); **(iii)** Molecular Biology: Ambion TRIzol Reagent were purchased from Life Sciences–Fisher Scientific Inc. (Waltham, Massachusetts, USA), DNase I was purchased from Invitrogen, (Carls-band, California, USA), High Capacity cDNA Reverse Transcription Kit, and PowerUpTM SYBRTM Green Master Mix 2x were purchased from Applied Biosystems (Foster City, CA, USA). **(iv)** Zymography: gelatin, Tris-HCl buffer, ammonium persulfate (APS), and triton X100 were purchased from Sigma-Aldrich (St. Louis, Missouri, USA); Sodium dodecyl sulfate was purchased from Synth (Diadema, São Paulo, Brazil); Poly-acrylamide/BIS-acrylamide solution (29:1), and N, N, N', N'tetramethylethylenediamine (TEMED) were purchase from Bio-Rad (Hercules, California, USA); **(v)** ESI-MS/MS: ammonium bicarbonate/acetonitrile (Ambic/ACN, 50:50 v/v), dithiothreitol (DTT), Indole-3-Acetic Acid (IAA), methanol, and formic acid were purchased from Sigma-Aldrich (St. Louis, Missouri, USA).

3.2 Methods

3.2.1 Strategy to Reinforce Chitosan Hydrogel

Considering the deacetylation degree (75%) of chitosan, we initially estimated that about 10% of the chitosan monomer's mass weight corresponds to NH_2 groups, and these are the most likely interaction sites with MWCNT and nHA that were used as our reference parameter to vary the chitosan/MWCNT/nHA ratios. We investigated three main synthesis parameters: temperature (20 °C and 37 °C), MWCNT, and nHA concentration within chitosan ($Chitosan_{NH2}$: MWCNT = $Chitosan_{NH2}$: nHA = 1:1, 2:1, 4:1, 1:2, and 1:4 w/w), and time reaction (0, 3, and 6 h).

Then, we screened MWCNT- and nHA-bearing systems regarding the interaction level among the compounds to determine a composite hydrogel formulation. Such a screen test was based on the samples' physical-chemical characterization based on Fourier Transformed Infra-Red Spectroscopy (FTIR), Scanning Electron Microscopy and Energy Dispersive Spectrometry (SEM/EDS), Thermal, and Swelling properties. Then, the composite was led to the indirect contact method as a second screen test to assess cell viability and mitochondrial activity according to the regular ISO 10993-5 guidelines. Afterward, we gathered the $Chitosan_{NH2}$: MWCNT = 2:1 (w/w) and $Chitosan_{NH2}$: nHA = 1:1 (w/w) conditions to form $Chitosan_{NH2}$: MWCNT = 2:1:2 (w/w/w) hydrogel blend, which was conducted to all gene expression of differentiation and ECM remodeling. Also, to deeply understand these remodeling phenomena, we performed a zymography assay using the same conditioned medium by the gathered hydrogel condition to investigate gelatinase activity. We propose that these extra cell machinery characterizations address direct assistance to the ISO-10993-5 guideline, named here as the QP-BioScreen protocol.

3.2.2 Functionalization of Multi-Walled Carbon Nanotubes

Pristine multi-walled carbon nanotubes were functionalized via acid attack assisted by an ultrasonic bath for nine hours (PEDROSA et al., 2010). Briefly, 100 mg of MWCNT were immersed in 4 mL of a sulfonitric solution (H_2SO_4:HNO_3 = 3:1, v/v) to obtain a colloidal suspension. After the 9-hour ultrasonic bath, the suspension of f-MWCNT was rinsed several times through centrifugation by applying 10000 RPM for 30 minutes in each wash

until pH reached values around 3 ~ 4 to remove the excess undesirable organic groups. By the end, the functionalized MWCNT suspension was concentrated at 0.8 % (w/v) before being used in chitosan reinforcement and was evaluated regarding its surface charge and particle size by Zeta Potential and Nano Tracking Analysis, respectively.

3.2.3 Synthesis of Hydroxyapatite Nanoparticles

The synthesis route of the hydroxyapatite (Ca_{10} $(PO_4)_6$ OH_2) nanoparticles was based on the co-precipitation method, widely used in the literature and previously studied by authors (MARTINS et al., 2020a). First, precursor solutions of [$CaCl_2$] = 6.0 mmol/L and [Na_3PO_4] = 3.6 mmol/L were prepared and mixed following the Ca/P molar ratio of 1.67 in a final volume of 250 mL. Calcium chloride was dripped into the sodium phosphate solution under vigorous magnetic stirring to obtain the nanoparticles. After dripping, a 1-hour of synthesis time was adopted. To prevent the degradation of hydroxyapatite nanoparticles, we first obtained sodium phosphate by phosphoric acid with sodium hydroxide reaction in a 1:3 molar ratio, dripping $CaCl_2$ afterward. After the end of the synthesis, the samples were washed and centrifuged twice at 5000 rpm for 3 minutes to remove non-binding residues. Thus, the pH of the suspensions of the synthesized hydroxyapatite nanoparticles remained alkaline, around 7 and 8, to avoid degradation during nHA participation in the crosslinking process within the chitosan matrix. Hydroxyapatite nanoparticles were analyzed using FTIR spectroscopy.

3.2.4 Synthesis of chitosan hydrogels crosslinked with MWCNT and nHA nanoparticles

80 mg of chitosan was dissolved in 4 mL of acetic acid solution (2% v/v) and kept at 37 °C under gentle stirring for 20 minutes. Then, composites with only chitosan and MWCNT were initially prepared by dripping the MWCNT suspension into the polymer solution, and after a uniform dispersion was achieved after 30 minutes, its pH was raised to ~ 6.5 with NaOH solution (2 mol/L). The Chitosan/MWCNT composites were initially prepared with a $Chitosan_{NH2}$: MWCNT = 1:1 w/w ratio, and the reaction was conducted

either at 20 °C or 37 °C for 3 h. Next, the reaction temperature was fixed at 37 °C, and the Chitosan$_{NH2}$: MWCNT w/w ratio was varied as 1:1, 2:1, and 4:1. In this case, the reactions were conducted for 3 h and 6 h.

Chitosan/nHA composites were sequentially synthesized using the same experimental parameters (time, temperature, and w/w ratios) to prepare the Chitosan/MWCNT samples. Finally, Chitosan/MWCNT/nHA composites were prepared with a Chitosan$_{NH2}$: MWCNT: nHA = 2:1:2 w/w ratio, and the reaction was conducted during 0 h and 3 h. Below, **Figure 5** shows a scheme illustrating the compound's structures and organization when used in hydrogel form:

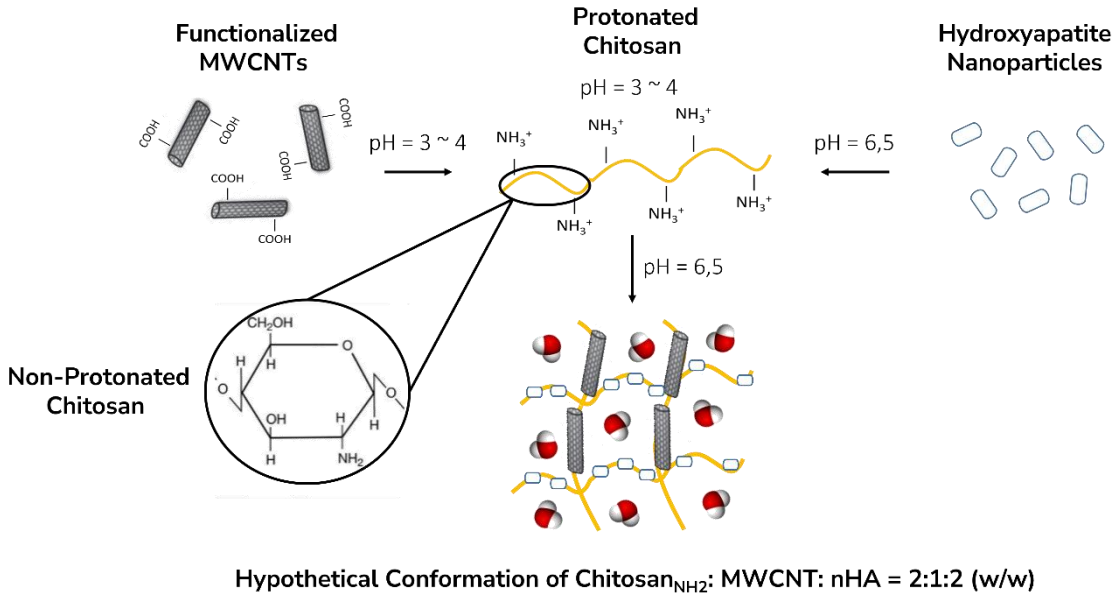

Figure 5: Scheme representation of chitosan, MWCNT, and hydroxyapatite nanoparticles before and after mixing during the hydrogel synthesis.

3.3 Materials Characterization

3.3.1 Zeta Potential and Particle Size of MWCNT

The surface charge and particle size of functionalized MWCNT were evaluated using a Zetasizer Nano ZS90 and Nano Tracking Analysis using a Malvern NanoSight NS300 equipment. The MWCNT suspension (0.1% w/v) was diluted on a pH scale between 3 and 8.

3.3.2 Fourier Transformed Infrared Spectroscopy (FTIR)

In the FTIR technique, we investigated the vibrational features of the crosslinked chitosan hydrogels. All samples were dried in an oven at 65°C for 18 h before the data collection and further pelleted with the analytical KBr salt using a Nexus Nicolet 640 spectrometer to characterize the surface chemical groups. All the spectra were collected between 400 and 4000 cm^{-1}. More relevant information was found in spectral intervals between 1800 cm^{-1} - 1200 cm^{-1} and 1200 cm^{-1} - 900 cm^{-1} regions, in which we focused our discussion and normalized by maximum absorbance value for each interval to evaluate the temperature, concentration, and time effects parameters. All the collected data were processed and analyzed using Origin Pro 8.5 software (OriginLab, USA).

3.3.3 Swelling and Degradation Properties

The short-term swelling ability of shape-less pure chitosan and the hydrogels with the following w/w ratios were evaluated: $Chitosan_{NH2}$: MWCNT = 2:1 (w/w), $Chitosan_{NH2}$: nHA = 1:1 (w/w), and $Chitosan_{NH2}$: MWCNT: nHA = 2:1:2 (w/w/w). The selected samples were washed and immersed in 20 mL of absolute ethanol for complete dehydration for these experiments. After every 10 minutes of immersion, the pure ethanol was exchanged until a total immersion time of 1 h. Next, all the samples were left at room temperature for 24 hours for slow ethanol evaporation to preserve the internal porous structure, and the swelling of the samples was evaluated in deionized water (DI), PBS (Phosphate Buffer Saline, 10 mmol/L, pH = 7.4).

For the degradation test and after synthesis, 1 mL of the pure chitosan and $Chitosan_{NH2}$: MWCNT: nHA = 2:1:2 (w/w/w) samples were deposited into a 24-well plate used as a mold. After deposition, the wells were filled with NaOH 2 mol/L bath for 10 minutes. Next, samples were scooped from the 24-well plate mold and rinsed with DI water to remove excess NaOH to avoid changes in the pH of the cell culture medium. Then, samples were challenged using a non-supplemented MEM-α cell culture medium and monitored for 7 days. Either the swelling and degradation properties were assessed

via the equations below (DHIMAN; RAY; PANDA, 2004; NAM et al., 2016; REN et al., 2018):

$$S = 100 * \left[\frac{(M_S - M_D)}{M_S}\right]$$

$$D = 100 * (1 - \left[\frac{(M_M - M_i)}{M_i}\right])$$

where M_S is the weight of the swollen hydrogel, M_D is the weight of the dried hydrogel, M_i is the initial weighted mass before exposure to cell medium, M_M is the mass after cell medium exposure, collected every 24 h for 7 days using MEM-α cell culture medium, S is the swelling degree, and D is the percentage of degraded mass of hydrogels.

To determine *Ms*, the solvent adsorbed on the surface of the hydrogels was carefully removed and monitored over 60 minutes for the swelling test. The dimensions of pure chitosan and Chitosan$_{NH2}$: MWCNT: nHA = 2:1:2 (w/w/w) samples were also monitored for the degradation analysis. All the measurements were performed in triplicates, and the data passed in the Normality test. They were processed using analysis of variance (two–way ANOVA), considering the treatment and time as main parameters, and multiple comparisons of all pairs of groups were made by applying Tukey's correction posttest and parametric analysis. Further, the significance level is considered when $\alpha = 0.05$. The data was treated using the GraphPad Prism 8 program (GraphPad Software, La Jolla, CA, USA).

3.3.4 Thermogravimetry and Differential Thermal Analysis (TG/DTA)

Considering the experiment needs, the same sample preparation method described above was also used for the thermal analysis. Around 100 mg of all samples were placed in an aluminum holder and evaluated by thermogravimetric analyzer STA 449 F3 (NETZSCH) located at Thermal Analysis Laboratory (UNESP Bauru Campus, São Paulo) under the supervision of Dr. Gilbert Bannach. The temperature range was between 25 °C and 900 °C using a temperature ramp of 10 °C/min at room atmosphere. Thermogravimetry analysis uses a microbalance system that monitors mass loss during increasing

temperatures to investigate the degradation of the solvent and organic compounds. Differential Thermal Analysis is also performed during the same experiment using an inert material as the reference sample to monitor significant and slight changes in the thermogravimetric curves (GOMEZ SANCHEZ et al., 2018; PIERÓG; OSTROWSKA-CZUBENKO; GIERSZEWSKA-DRUZYŃSKA, 2012). Both techniques can show differences among the hydrogel formulations regarding the synthesis conditions and overall chemical group formation dynamics.

3.3.5 Scanning Electron Microscopy and Energy Dispersive X-ray Spectroscopy (SEM/EDS)

For these analyses, the chitosan hydrogels (Pure Chitosan, Chitosan$_{NH2}$: MWCNT = 2:1; Chitosan$_{NH2}$: nHA = 1:1, and Chitosan$_{NH2}$: MWCNT: nHA = 2:1:2 w/w) were immersed in ethanol for 18 hours at room temperature immediately after synthesis for dehydration. Next, the samples were rinsed with deionized water several times and kept at room temperature for another 24 hours for complete solvent evaporation. The samples were then cut into 1 mm pieces, fixed with carbon tapes on regular glass slides for microscopy, and investigated with an FEI Quanta 200 scanning electron microscope. The EDS analyses were performed to monitor the presence of Ca and P in the formulations bearing nHA. Hence, the samples with the following w/w ratios were evaluated: Chitosan$_{NH2}$:nHA = 1:1 and Chitosan$_{NH2}$:MWCNT:nHA = 2:1:2. The collected EDS spectra of hydrogels were assessed using an electron beam intensity range between 12.5 KeV and 25 KeV.

3.4 Cell Culture and *in vitro* Tests

3.4.1 Cell Viability and Adhesion evaluation by Colorimetric Assays of MTT and Crystal Violet (CV)

In the same preparation way described in SEM analysis, chitosan hydrogels (Pure Chitosan, Chitosan$_{NH2}$: MWCNT = 1:1, 2:1; Chitosan$_{NH2}$: nHA = 1:1; Chitosan$_{NH2}$: MWCNT: nHA = 2:1:2 w/w) were immersed in ethanol for 18 hours at room temperature immediately after synthesis for dehydration. Next, the samples were rinsed with

deionized water several times and kept at room temperature for another 24 hours for complete solvent evaporation. Afterward, all samples were sterilized using Phoenix AV Plus vertical autoclave, setting the cycle to 40 min at 127° C. Then, all chitosan hydrogel samples were immersed in the cell culture medium (MEM-α, without fetal bovine serum) for the conditioning procedure following the ISO 10993-5 protocol for 24 hours (0.2 g/mL concentration for irregular and porous samples) before treating the cell monolayers. Cell media were filtered using a syringe and a 200 µm-thick filter membrane after the conditioning medium step. The different conditioned cell media challenged $5x10^4$ cells of MC3T3-E1 subclone 4 (ATCC, USA) subconfluent cells in a 96-well plate inside of an incubator at 37 °C and 5% CO_2 atmosphere for 24 h and 72 h, without any media exchange.

The cell mitochondrial activity and adhesion were assessed by MTT and CV (MTT: 3-(4,5-dimethyl thiazolyl-2)-2,5-diphenyltetrazolium bromide; CV: hexamethyl pararosaniline chloride salt) staining tests, respectively. For the MTT assay, the same conditioned culture medium was removed, and fresh α-MEM cell media containing 0.5 mg/mL of MTT salt was added to the wells for another 3 h. Next, the MTT solution and 100 µL of absolute ethanol were removed to complete the staining process before measurements. For the CV assay, the conditioned culture medium was removed, and cells were treated for 5 minutes with an acetic acid solution (2%, w/v) before the CV salt (1%, w/v) incorporation to open the membrane and reach the nuclei content. After another 5 minutes of salt incorporation, cells were rinsed with 100 µL two times with acetic acid (33%, v/v) before measurements. In either stained plate, nuclei and mitochondrial content quantification were assessed by a microplate reader (SYNERGY-HYX multimode reader, BioTek, USA), using λ = 570 nm for MTT and 540 nm for CV measurements. The statistical analysis is plotted using the mean ± standard error deviation (SD) (n = 5). Significant differences were considered when $p < 0.05$. Data were processed using analysis of variance (two–way ANOVA) with multiple comparisons of all pairs of groups, using Tukey's correction posttest and parametric analysis. Further, the significance level was considered when $\alpha = 0.05$. All data were obtained using the GraphPad Prism 8 program (GraphPad Software, La Jolla, CA, USA).

3.4.2 messenger RNA (mRNA) isolation and Reverse Transcription-quantitative Polymerase Chain Reaction (RT-qPCR)

MC3T3-E1 subclone 4 cell lines were harvested and monitored for 3, 7, and 21 days and challenged using the conditioned cell media of $Chitosan_{NH2}$: MWCNT: nHA = 2:1:2 hydrogel, osteogenic medium (10 mmol/L of β-glycerophosphate, 50 µg/mL of Ascorbic Acid, and 0,01 µmol/L of dexamethasone) as a positive control, and pure chitosan hydrogel as a negative control, in which the conditioned cell media was partially exchange every 3 days for cell treatment maintenance. The total mRNA was isolated using Ambion TRIzol Reagent and treated with DNase I enzyme. Complementary DNA (cDNA) synthesis was performed using a High-Capacity cDNA Reverse Transcription Kit following the manufacturer's instructions. RT-qPCR was performed on a total of 10 µL, containing PowerUp™ SYBR™ Green Master Mix 2x (5 µL), 0.4 µM of each primer for amplification, and 50 ng of cDNA, and nuclease-free H_2O. Data were obtained using QuantStudio 3 (Applied Biosystems by Thermo-Fischer, Waltham, Massachusetts, EUA). They were expressed as relative amounts of each target gene normalized considering the n-fold-change expression of genes, here used as housekeeping the β-actin gene, using the cycle threshold (Ct) method. The statistical analysis is plotted using the mean ± standard error deviation (SD) ($n = 3$). Significant differences were considered when $p < 0.05$. Data were processed using analysis of variance (two–way ANOVA) with multiple comparisons of all pairs of groups, using Tukey's correction posttest and parametric analysis. Further, the significance level was considered when $\alpha = 0.05$. All data were obtained using the GraphPad Prism 8 program (GraphPad Software, La Jolla, CA, USA). Below, Table 2 depicts the forward and reverse primer pair, which all were purchased from Integrated DNA Technologies (IDT, Coralville, Iowa, USA) used for the gene expression experiment:

Table 2: Expression Primers Sequences and Polymerase Reaction Cycle Conditions

Gene	Primer	5' – 3' sequence	Reaction's Conditions
Alpl	Forward	TGGTCACAGCAGTTGGTAGC	95° C - 15 s; 62° C
	Reverse	TAGTCACAATGCCCACGGAC	-30 s; 72 ◦C - 30 s
Bmp-2	Forward	GCAAGAACAAAGCAGGACCA	95° C - 15 s; 62° C
	Reverse	TGCTTCTTTATGAGGGCCCA	-30 s; 72 ◦C - 30 s
Col1a1	Forward	TTCTCCTGGCAAAGACGGAC	95° C - 15 s; 62° C
	Reverse	CCATCGGTCATGCTCTCTCC	- 30 s; 72 ◦C - 30 s
Mmp-2	Forward	AACTTTGAGAAGGATGGCAAGT	95° C - 15 s; 62° C
	Reverse	TGCCACCCATGGTAAACAA	- 30 s; 72 ◦C - 30 s
Mmp-9	Forward	TGTGCCCTGGAACTCACACGAC	95° C - 15 s; 62° C
	Reverse	ACGTCGTCCACCTGGTTCACCT	- 30 s; 72 ◦C - 30 s
Ssp1	Forward	TTTGCTTTTGCCTGTTTGGC	95° C - 15 s; 62° C
	Reverse	CAGTCACTTTCACCGGGAGG	- 30 s; 72 ◦C - 30 s
Bglap	Forward	AGCTCAACCCCAATTGTGAC	95° C - 15 s; 62° C
	Reverse	AGCTGTGCCGTCCATACTTT	- 30 s; 72 ◦C - 30 s
Runx-2	Forward	GGACGAGGCAAGAGTTTCA	95° C - 15 s; 62° C
	Reverse	TGGTGCAGAGTTCAGGGAG	- 30 s; 72 ◦C - 30 s
Timp-1	Forward	ATCCTCTTGTTGCTATCACTG	95° C - 15 s; 62° C
	Reverse	GGTCTCGTTGATTTCTGGG	- 30 s; 72 ◦C - 30 s
Timp-2	Forward	GCAACAGGCGTTTTGCAATG	95° C - 15 s; 62° C
	Reverse	CGGAATCCACCTCCTTCTCG	- 30 s; 72 ◦C - 30 s
Tgf-β1	Forward	TCGCTTTGTACAACAGCACC	95° C - 15 s; 62° C
	Reverse	ACTGCTTCCCGAATGTCTGA	- 30 s; 72 ◦C - 30 s
β-actin	Forward	TCTTGGGTATGGAATCCTGTG	95° C - 15 s; 62° C
	Reverse	AGGTCTTTACGGATGTCAACG	- 30 s; 72 ◦C - 30 s

3.4.3 Mineralization Index by Alizarin Red S Staining

MC3T3-E1 subclone-4 cells were harvested for Alizarin Red S staining in 24-well plates for 3, 7, 14, and 21 days. Chitosan$_{NH2}$: MWCNT: nHA = 2:1:2 hydrogel was used as a sample target, the osteogenic medium as a positive control (10 mmol/L of β-glycerophosphate, 50 µg/mL of Ascorbic Acid, and 0,01 µmol/L of dexamethasone), and pure chitosan hydrogel as a negative control. After harvesting, cells were fixed in phosphate-buffered 10% formalin for 30 min, then washed with PBS Buffer (Ca^{2+} and Mg^{2+} free). Afterward, cells were stained with Alizarin-Red S (2%, w/v, pH = 4.1) and left for an extra 45 min covered by aluminum foil. Next, the Alizarin Red S solution was extensively washed with PBS to eliminate non-bonded staining. The stained cells were assessed using an inverted microscope (Axio Vert.A1, Zeiss, Germany), in which images were acquired using a camera Axiocam 503 color (Zeiss, Germany).

3.4.4 Matrix Metalloproteinases (MMPs) Activities by Gelatin Proteolysis-based Zymography Assay

After running the experimental ISO 10993-5 workflow, the conditioned culture media of 3, 7, 14, and 21 days of culture time was centrifuged at 14,000 rpm for 15min to avoid cell debris, and the protein concentration determined by the Lowry method (HARTREE, 1972). The experiment was performed in triplicate. $Chitosan_{NH2}$: MWCNT: nHA = 2:1:2 hydrogel was used as a sample target, the osteogenic medium as a positive control (10 mmol/L of β-glycerophosphate, 50 µg/mL of Ascorbic Acid, and 0,01 µmol/L of dexamethasone), and pure chitosan hydrogel as a negative control. The exact amount of protein was resolved into a 12% polyacrylamide gel containing 4% gelatin, and for its polymerization using as purchased 237 µL of APS and 25 µL of TEMED. Next, polymerized gels containing the samples were placed within an electrophoretic cube set at 120 mA for 4 h using Tris/HCl-SDS 0,1 M, pH 6,8 running buffer. The gelatinolytic activity was determined in the resolved proteins after electrophoretic running. Then, renaturation of samples within the gels was performed using Triton X-100 aqueous solution (2% w/v), incubated for 18 hr in proteolysis buffer (Tris-$CaCl_2$, 5 mmol/L) at 37°C and then stained with Coomassie Blue R-250 dye solution 0.05% for 3 h when the gels were washed in a 30% methanol (v/v) and 10% glacial acetic acid solution (v/v). The opposite staining was obtained in the gels exactly where there was the gelatinolytic activity (bands) of MMP-2 (~62 kDa) and MMP-9 (~84 kDa), and then they were analyzed and quantified using the software ImageJ (Bethesda, MD), following a previous study (LEFEBVRE; PEETERS-JORIS; VAES, 1991).

4. RESULTS AND DISCUSSIONS

4.1 Surface Charge and Particle Size of Functionalized MWCNT

After the functionalization of pristine MWCNT, the first effect of successful functionalization is noticed by achieving an eye-naked colloidal suspension, as displayed below in **Figure 6**:

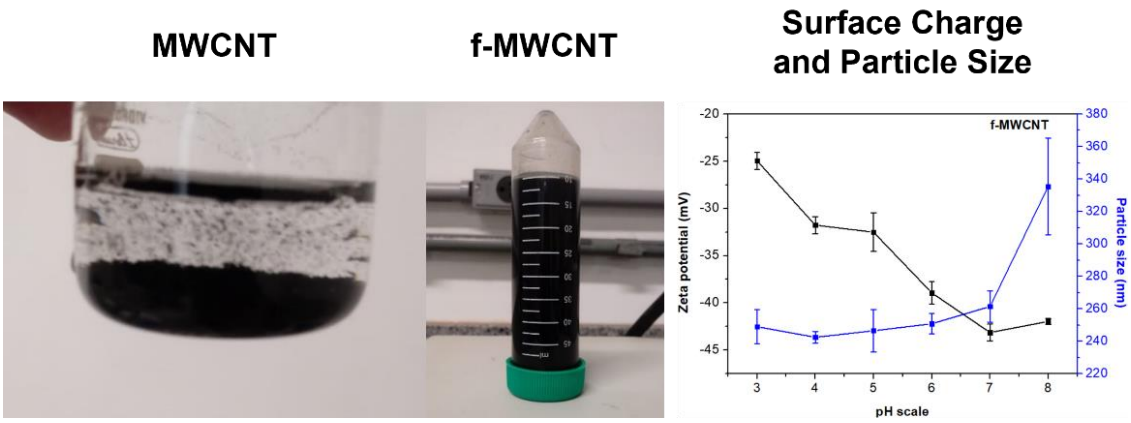

Figure 6: Before and after the functionalization of MWCNT. Zeta potential variation of its surface charges and particle size after the 9-hour functionalization process using an ultrasonic bath and acidic attack by sulfonitric solution (H_2SO_4: HNO_3 = 3:1, v/v) at room temperature.

Regarding the functionalized MWCNT behavior within the pH scale variation, the surface charges increase negatively during the rise of the pH scale until pH = 8. The second effect is related to the MWCNT particle size and its length. The particle size between pHs 3 and 7 suggests they are smaller than those informed by the provider of pristine carbon nanotubes (Length as-purchased: 0.5 – 10 µm), shortening its length as an effect of the functionalization process. After the very first pilot experiments with chitosan, we decided to maintain the f-MWCNT pH solution low, around 3~4, before using it in hydrogel synthesis. Even though the negative surface charge above pH = 5 did not change considerably, it seemed enough to change the MWCNT interaction with chitosan, jeopardizing its dispersion and forming floccule-like clusters instead of a uniform hydrogel. It was experimentally noticed that by adding MWCNT at the same pH value that chitosan is dissolved, and with a slow neutralization of the hydrogels until pH = 6.5, we counter this issue and slowly increase the negative surface charges of f-MWCNT, balancing the interaction with the amine groups from chitosan.

4.2 FTIR Spectroscopy

4.2.1 Compounds Features

Firstly, we start the FTIR spectroscopy investigation with the most relevant spectral regions displayed for pure chitosan, nHA, and MWCNT to identify the functional groups

of each compound. **Figure 7(A)** shows the vibrations between 900 and 1200 cm^{-1}, whereas **Figure 7(B)** shows the vibrations between 1200 and 1800 cm^{-1}. In the following FTIR analyses, these spectral regions will also be debated, and the full spectra of pure compounds will be presented in the Appendix Section (**Fig. A1**).

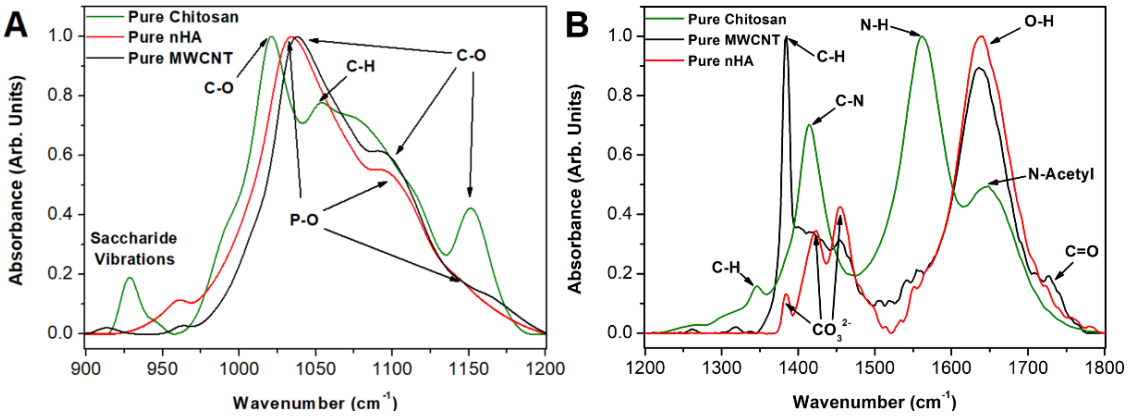

Figure 7: (A) FTIR spectra of pure chitosan, MWCNT, and nHA, between (A) 900 cm^{-1} and 1200 cm^{-1} and (B) the 1800 cm^{-1} – 1200 cm^{-1} spectral region.

In brief, **Fig.7(A)** mainly comprises vibrations from the C-O-C groups either from the chitosan's glycosidic linkages or the MWCNT backbones (BRANCA et al., 2016; MAURICIO-SÁNCHEZ et al., 2018; ŢUCUREANU et al., 2016) and the contributions from phosphate groups from the nHA. For this spectral region, the highest peaks were normalized equal to unity. Meanwhile, the spectral region highlighted in **Fig.7(B)** is mainly formed by stretching vibrations of C=O groups either from chitosan's acetyl groups or the MWCNT's surface (PEDROSA et al., 2010; ŢUCUREANU; MATEI; AVRAM, 2016) and deformations of O-H, N-H, C-H, and C-N groups.(BRANCA et al., 2016; DAI et al., 2012; GUO et al., 2007; LIANG; LI; TIAN, 2016; MARTINS et al., 2020b; PAULINO et al., 2006; ŢUCUREANU et al., 2016; VISWANATHAN; SUNDARAM; MEENAKSHI, 2009) The N-H vibrations have been normalized to a unit for this spectral region. The following FTIR data presented in the main text were normalized, and the assignments shown in the figures are summarized in **Table 3**:

Table 3: Vibrational Bands Of The Compounds Present In Our Hydrogel Formulation

Compound	Chemical Group	Wavenumber (cm^{-1})
Chitosan	N-Acetyl/OH	1645 – 1635
	NH_2	1560
	C-N	1415
	C-H	1345
	C-O-C, C-H	1200 – 900
MWCNT	C=O	1675 – 1665
	C-H	1380
	C-O-C, C-H	1200 – 900
nHA	P-O	1200 – 900
		*800 – 400
		***(Fig. A1)**

4.2.2 Influence of Synthesis Temperature

Firstly, it is important to mention the choice of $Chitosan_{NH2}$: MWCNT = 1:1 (w/w) hydrogel to investigate the temperature synthesis parameter. We judged that the effects of temperature are highlighted when the MWCNT presence properly influences the interactions with chitosan since this condition matches the concentration of NH_2 groups and MWCNT, so as between the polymer and the carbon nanotube backbones. **Figure 8** depicts the most relevant vibrational features of the samples with $Chitosan_{NH2}$: MWCNT = 1:1 (w/w) ratio synthesized either at 20 °C or 37 °C for 3 hours:

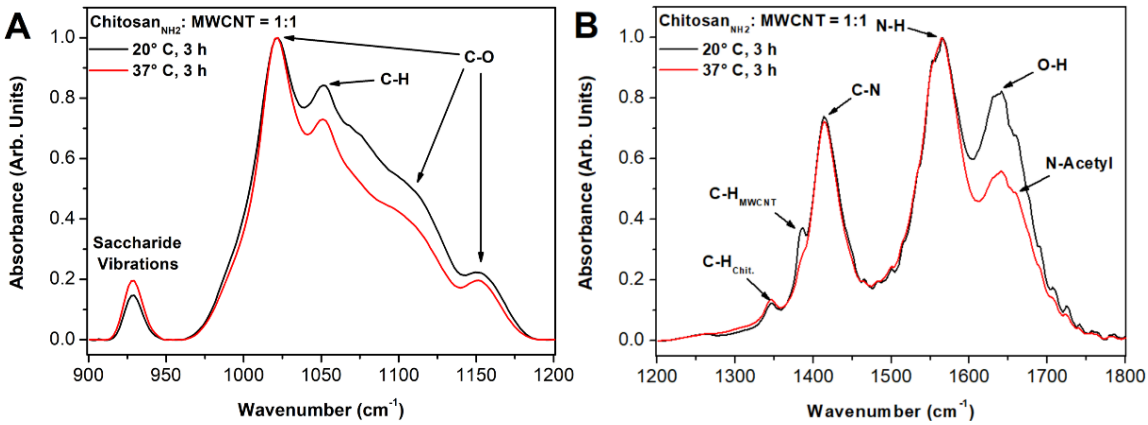

Figure 8: (A) FTIR spectra between 1200 cm^{-1} and 900 cm^{-1} for the samples synthesized at 20° C and 37° C for 3 h. In (B), the spectral region between 1800 cm^{-1} and 1200 cm^{-1} is presented for the same monitored samples.

Despite the superposition of several bands within the region shown in Fig.9(A), one can still notice a narrowing in the C-O vibrations from chitosan and MWCNT in the sample prepared at 37 °C compared to that synthesized at 20 °C. This behavior indicates that at 37 °C, a more efficient dispersion of the chitosan chains occurs, leading to a likely lower degree of interactions involving the polymer backbone. One could argue that this effect also reflects a better dispersion of the nanotubes and the reduction in the nanotube-nanotube interactions. However, considering the position of the highest peak of this spectral region [and in comparison with those depicted in **Figure 7**], it is more likely that chitosan's vibrations are more clearly observed. As for the spectral region displayed in **Fig.8(B)**, the most remarkable difference between the samples is regarding the O-H bending and C-H_{MWCNT} asymmetric bending modes, which are reduced in the sample prepared at 37 °C. Hence, we infer a great participation of the OH groups in the MWCNT/chitosan interactions, which are more efficient at 37 °C. Also, the intensity reduction of C-H_{MWCNT} groups' vibration of carbon backbone indicates that at 37° C, the MWCNTs are indeed more dispersed compared to the synthesis performed at 20° C. This occurs probably due to changes in the chitosan polymeric chains' conformation (JURAK et al., 2019) when temperature increases, improving MWCNT/chitosan interactions. Based on these results, we defined 37 °C as our standard synthesis temperature. One should notice that we did not investigate the temperature effect using hydroxyapatite nanoparticles because the carbon nanotubes are more prone to contribute significantly to the reinforcement (JIAN et al., 2023; MALLAKPOUR; MADANI, 2015; RAHMAN et al., 2024)

4.2.3 Influence of Nanoparticle Concentration

4.2.3.1 Influence of MWCNT Concentration

For the investigation regarding the effects of chitosan hydrogel reinforcement by the reducing and increasing of MWCNT concentration within chitosan hydrogel, we fixed the synthesis temperature at 37 °C and 3 h of synthesis time. We used a multiplying factor of 2 to increase and decrease the MWCNT concentration. Now, turning to the effects of the concentration of nanoparticles on the vibrational properties of the composites, **Figure 9** presents the spectral regions of interest for samples containing $Chitosan_{NH2}$: MWCNT = 1:4, 1:2, 2:1, and 4:1 w/w ratios. The proportional reduction of MWCNT, as seen in

Fig.9(A, B), and the MWCNT concentration increase is shown in **Fig.9(C, D)**. Also, for better comparison, the data from the sample with $Chitosan_{NH2}$: MWCNT = 1:1 reacted for 3 h at 37 °C is reproduced again from **Figure 9**:

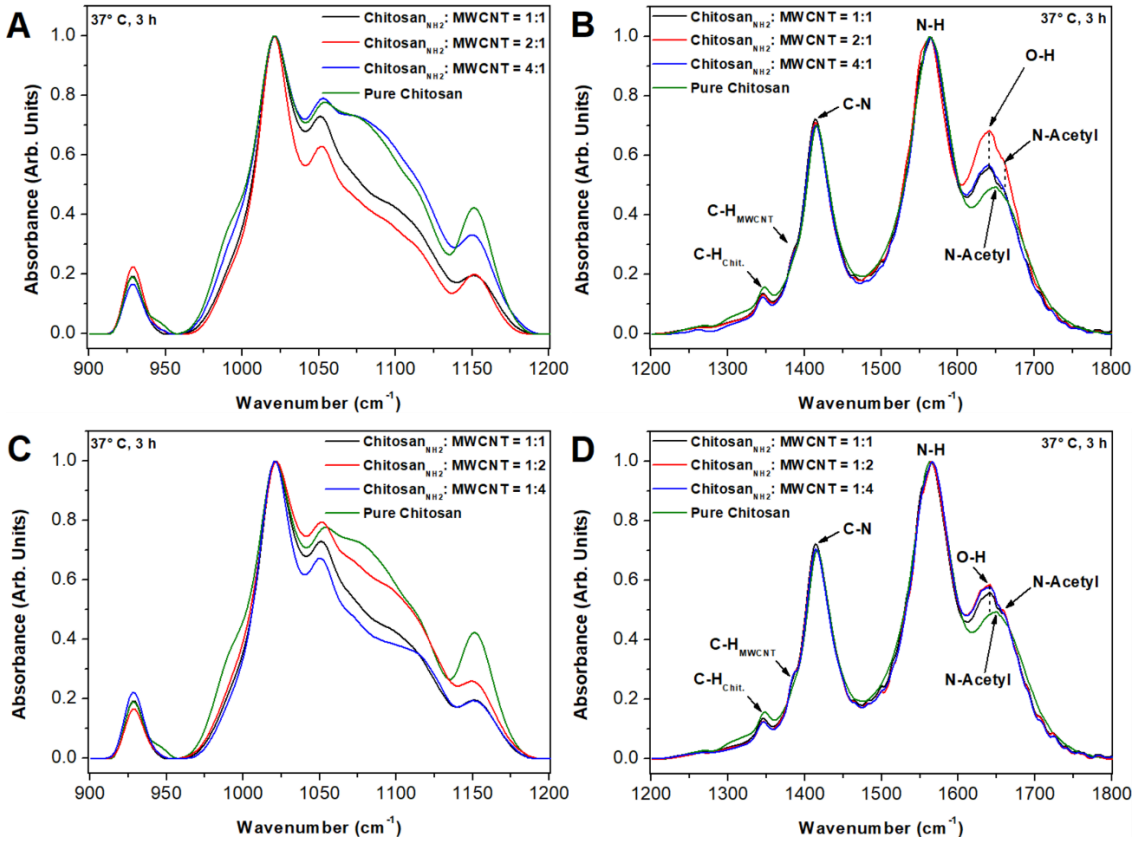

Figure 9: (A – B) FTIR spectra between 900 cm^{-1} – 1200 cm^{-1} and 1800 cm^{-1} – 1200 cm^{-1}, respectively, for the $Chitosan_{NH2}$: MWCNT = 1:1, 2:1, and 4:1, as well as for (B – D) $Chitosan_{NH2}$: MWCNT = 1:1, 1:2, and 1:4 synthesized samples at 37° C for 3 h.

Several remarkable differences occurred among the samples. Between 900 cm^{-1} and 1200 cm^{-1}, the $Chitosan_{NH2}$: MWCNT = 1:1 and 2:1 samples decreased in signal and broadening with the MWCNT concentration reduced, while the excess of chitosan in the sample with $Chitosan_{NH2}$: MWCNT = 4:1 leads to broader bands, very similar to the pure chitosan spectrum. It shows us the strength limit of interactions between the polymer and carbonic backbones regarding the MWCNT concentration. However, despite the better interaction detected in $Chitosan_{NH2}$: MWCNT = 1:4 due to a more prominent intensity decrease, no other relevant conclusion regarding the MWCNT concentration can be reached between 900 cm^{-1} and 1200 cm^{-1} intervals since no tendency is detected while the MWCNT concentration increases.

Moving to the interval between 1200 cm^{-1} and 1800 cm^{-1}, the N-Acetyl vibrational band had an apparent red-shift dislocation from 1650 cm^{-1} to 1660 cm^{-1} or even a solving of vibration for all samples. It indicates that, in case of dislocation of the N-Acetyl band, the chemical environment is more confined, where possible physical adsorption occurs. Otherwise, only an effect of better dispersion has been detected. Considering that while the OH band around 1640 cm^{-1} had similar intensities, both the excess of chitosan and MWCNT concentration ratios, with $Chitosan_{NH2}$: MWCNT = 2:1 differing, there is not much conclusion we can take to this vibration. The same behavior is followed by the N-H, C-N, and $C\text{-}H_{MWCNT}$ vibrational bands, which also had no differences regardless of MWCNT concentration. The only remarkable difference among the synthesis conditions is a minor dislocation to lower frequencies of $C\text{-}H_{Chit.}$ band around 1345 cm^{-1} when compared to the pure chitosan spectrum. It indicates that, regardless of the MWCNT concentrations investigated, forming hydrogen bonds between chitosan and carbon nanotubes. Based on these results and in our discussion, accounting for the known cytotoxicity of MWCNT (DU et al., 2013; KYRIAKIDOU et al., 2020), we defined $Chitosan_{NH2}$: MWCNT = 2:1 as our standard ratio between the polymer and the nanotubes.

4.2.3.2 Influence of Hydroxyapatite Nanoparticles Concentration

The same spectral regions are presented below for composites bearing only chitosan and nHA in w/w ratios of $Chitosan_{NH2}$: nHA = 1:4, 1:2, 1:1, 2:1, and 4:1. For all cases, the syntheses were conducted likewise in the chitosan/MWCNT composites, differing only in the adding of nHA after the pH reaches 6.5 value, to avoid nHA degradation, sensitive to acidic pH values. All the collected spectra regarding the abovementioned chitosan-nHA hydrogels are depicted in **Fig.10(A – D)**.

The differences among the nHA concentrations occurred more significantly compared to the MWCNT case. Between 900 cm^{-1} and 1200 cm^{-1}, the main vibrational difference among synthesized samples, regardless of nHA concentration, is represented by the $Chitosan_{NH2}$: nHA = 2:1, in which both its broadening and intensity are reduced, evidencing the more prone interactions between the polymer backbone and phosphate groups. Meanwhile, all the other had a similar broadening and shape compared to the pure

chitosan sample, making it hard to find any relevant affirmatives due to the formed complex environment, especially for samples with more hydroxyapatite nanoparticles.

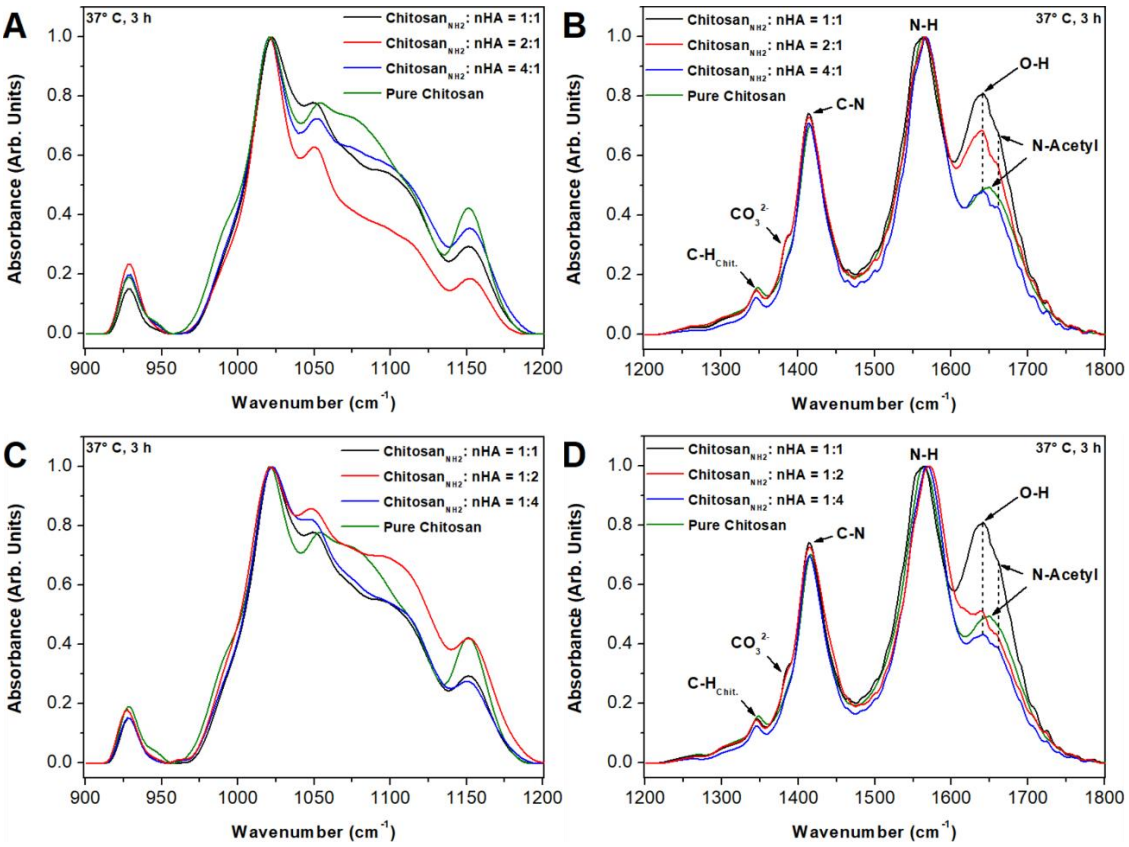

Figure 10: (A – B) FTIR spectra between 900 cm^{-1} – 1200 cm^{-1} and 1800 cm^{-1} – 1200 cm^{-1}, respectively, for the Chitosan$_{NH2}$: nHA = 1:1, 2:1, and 4:1, as well as for (B – D) Chitosan$_{NH2}$: nHA = 1:1, 1:2, and 1:4 synthesized samples at 37° C for 3 h.

However, between 1200 cm^{-1} and 1800 cm^{-1}, more distinguished information on behalf of the nHA concentrations was detected. The dislocation to higher frequencies of the N-Acetyl band around 1650 cm^{-1} to 1660 cm^{-1} is also detected for the chitosan-nHA hydrogel formulations and is now more noticeable due to differences in band intensity. Also interesting is that a tendency in N-Acetyl and OH vibrational bands intensity decrease is noticed, regardless of nHA concentration, indicating OH's participation in interactions with chitosan. Besides, the OH vibration became sharper at higher concentrations of nHA. In the same way, the NH vibrational band appeared as it, but here, it red-shifted as the hydroxyapatite nanoparticle concentrations increased, showing that nHA potentially better interacts with chitosan through amine groups. Last, the indicative formation of hydrogen bonds is apparently not easy to form between chitosan and nHA

compared to those chitosan hydrogel interacting with MWCNT, detected only for the $Chitosan_{NH2}$: nHA = 1:4 ratio.

Considering the more significant interactions were detected for those chitosan hydrogels with higher concentrations, we selected the $Chitosan_{NH2}$: nHA = 1:1 as our standard ratio between the polymer and apatite nanoparticles. We mainly wanted to follow our strategy to match the estimated amine group in chitosan. One could argue that the interaction between the polymer backbone and phosphate groups was stronger at $Chitosan_{NH2}$: nHA = 2:1. Also, others can point out that $Chitosan_{NH2}$: nHA = 1:1 condition will not respect the desired matching with remaining available amine groups present in $Chitosan_{NH2}$: MWCNT = 2:1 chosen as one of our synthesis standards. However, we do not have a linear and clear tendency for either excess chitosan or nHA, and based on our findings regarding the well-interaction between chitosan and high concentrations of nHA, we decided to maintain the nHA concentration as high as possible.

4.2.4 Influence of Synthesis Time

Next, we evaluated the effects of time on the interactions between chitosan and either MWCNT or nHA. In **Fig. 11(A, B)**, the evolution of the FTIR spectra for the sample with $Chitosan_{NH2}$: MWCNT = 2:1 after 0, 3, and 6h of synthesis is presented (note that the 0h data simply refers to a physical mixture). In **Fig. 11(C, D)**, similar figures are shown for the sample with $Chitosan_{NH2}$: nHA = 1:1. Between 0 and 3h, both the MWCNT- and nHA-bearing systems experience a fast narrowing of the vibrations displayed in (A, C) as well as a shift to lower frequencies in the highest peaks within the spectral region. Even though the 0 h spectra data represents the physical mixture, it could indicate the formation of hydrogen bonds over time among the compounds present in the selected standards hydrogel formulation.

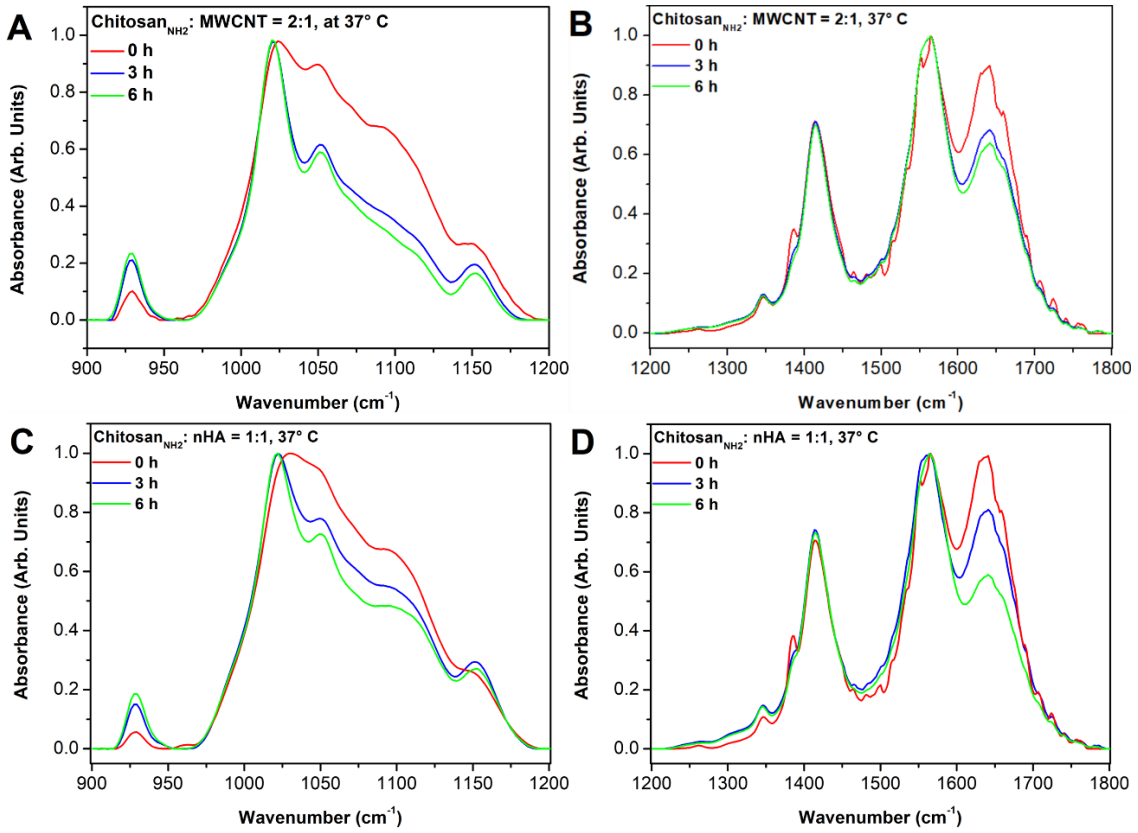

Figure 11: FTIR spectra of Chitosan$_{NH2}$: MWCNT = 2:1, as well as for Chitosan$_{NH2}$: nHA = 1:1 synthesized samples at 37° C monitored between 0 h and 3 h, illustrating the spectral interval between (A – C) 1200 cm^{-1} and 900 cm^{-1}, and (B – D) the spectral region between 1800 cm^{-1} and 1200 cm^{-1}.

By comparing these data with those shown in **Fig. 7(A)**, it is then clear that, over time, the vibrational contributions from MWCNT and nHA are gradually covered by those from the polymer due to the dispersion of the nanoparticles. Additionally, the time-dependent drop in the OH vibrations in both systems confirms that these groups are strongly involved in the interactions between the chitosan polymer, the apatite nanoparticles, and the carbon nanotubes. Besides, it is also clear that after 3 h of synthesis, only minor changes occur in shape and intensity on the Chitosan$_{NH2}$: MWCNT = 2:1 and Chitosan$_{NH2}$: nHA = 1:1 spectra. Considering this, we determined that the optimal time to achieve good stability is 3 h to use in the composite synthesis, our standard time parameter, as already presented in all our results.

Finally, guided by the above-discussed results, we conceived a composite containing chitosan, MWCNT, and nHA with a w/w/w ratio of Chitosan$_{NH2}$: MWCNT: nHA = 2:1:2. Firstly, **Fig. 12(A)** shows the FTIR spectra between 900 cm^{-1} and 1200 cm^{-}

[1] of the 3-hour MWCNT- and nHA bearing systems and the composite hydrogel at 37 °C, for a better comparison in the interaction phenomena:

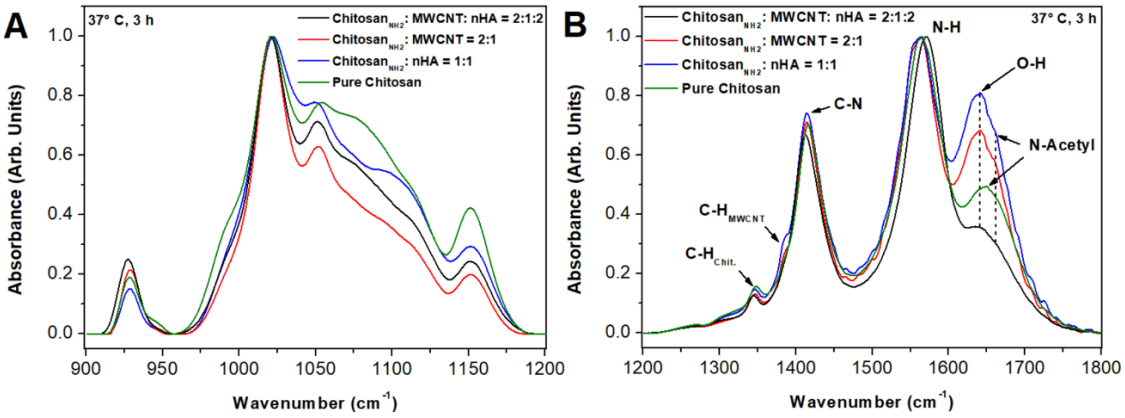

Figure 12: FTIR spectra comparison between the selected hydrogel formulation and the gathered composite one at 37°C and 3 h of synthesis time. In (A), spectra of compound separated and gathered synthesized chitosan hydrogels, between 900 cm^{-1} and 1200 cm^{-1}, as well as for (B) 1800 cm^{-1} and 1200 cm^{-1}.

Despite the peak intensity loss, the main remarkable differences here occur around 950 cm^{-1}. A blue-shift dislocation is noticed on the chitosan saccharide chain vibration, indicating the formation of hydrogen bonds when MWCNT and nHA coexist within the polymeric matrix. Noteworthy, such dislocation effect was only detected for the Chitosan$_{NH2}$: MWCNT: nHA = 2:1:2 hydrogel synthesis condition among all the investigated formulations investigated in this work. Between 1200 cm^{-1} and 1800 cm^{-1}, **Fig. 12(B)** compares the FTIR vibrations from the final composite with the systems bearing either MWCNT or nHA. The collected data from the composite had the most remarkable differences from our infrared spectroscopy investigation.

Interestingly, while the previous data already suggested strong participation of the OH groups either from MWCNT or nHA in their interactions with chitosan, the results from the composite allow us to confirm that such interactions are even stronger when MWCNT and nHA coexist in chitosan hydrogel. Also, a red-shift dislocation and narrowing of the N-H band around 1550 cm^{-1} is now clearly detected, indicating the formation of physical adsorption involving amine groups. Note that such an effect was considered where the nHA-bearing systems had their apatite concentration exceeding the amine groups from chitosan. Furthermore, the bands around 1425 and 1345 cm^{-1} were assigned to C-N and C-H$_{Chit.}$ bands are shifted to lower frequencies in the full composite

compared to the systems bearing MWCNT or nHA. Over time, the chitosan network is dispersed in the material, and the chemical environment around chitosan monomers is reinforced and structured. Meanwhile, the OH groups on the surface of both nanoparticles interact with the amine groups from the polymer via hydrogen bonds, thus forming a dynamic network. Therefore, it seems that MWCNT and nHA improve the formation of hydrogen bonds among the compounds when they coexist, which suggests an intrinsic synergy between MWCNT and nHA when embedded in polymeric chains (JYOTI et al., 2021; KUMAR; KUMAR; KUMAR, 2021; WANG et al., 2015).

4.3 Scanning Electron Microscopy and Energy Dispersive Spectrometry (SEM/EDS)

The morphological and compositional features of pure chitosan and the systems with $Chitosan_{NH2}$: MWCNT = 2:1, $Chitosan_{NH2}$: nHA = 1:1, and $Chitosan_{NH2}$: MWCNT: nHA = 2:1:2 (w/w ratios) were evaluated with SEM as shown in **Fig. 14**:

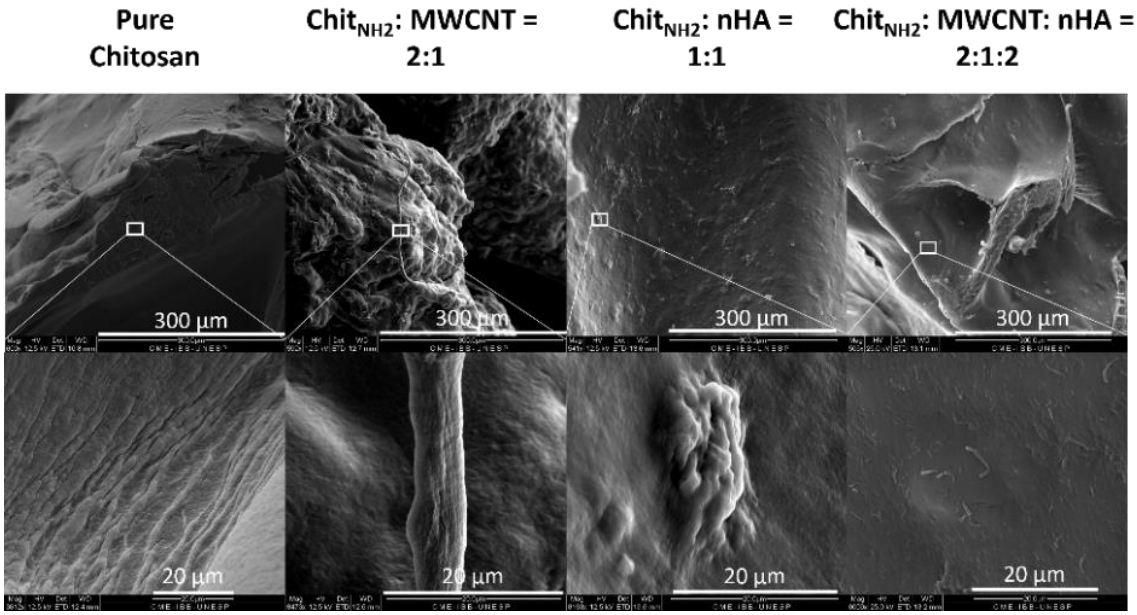

Figure 13: Morphology evaluation and surface features of all synthesized chitosan hydrogel formulations using scanning electron microscopy technique in different magnifications, as well as the atomic percentage content of the mineralized hydrogels.

The systems comprise structures ranging from 300 µm to 20 µm in all cases. With higher magnifications, it is possible to observe rugous-like for pure chitosan, fibrous-like

for Chitosan$_{NH2}$: MWCNT = 2:1, granule-like features for Chitosan$_{NH2}$: nHA = 1:1 hydrogels, and for Chitosan$_{NH2}$: MWCNT: nHA = 2:1:2 composite, the spatial distribution indicate a merged nanoparticle-like features. Also, we resort to EDS analyses to evaluate the Ca/P ratios in the nHA-bearing systems, and Table 4 shows the EDS spectrum and quantification of the atomic percentage content of the chitosan mineralized hydrogels:

Table 4: Energy X-Ray Dispersive Spectroscopy of The Mineralized Hydrogels

Sample	Element	Weight (%)	Atomic (%)
Chitosan$_{NH2}$: nHA = 1:1 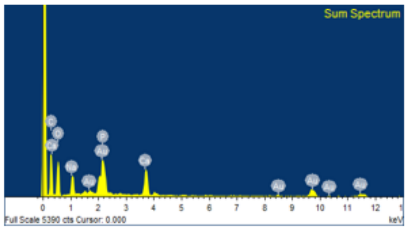	$C_{(k)}$	39.29	53.45
	$O_{(k)}$	36.90	37.69
	$Na_{(k)}$	8.07	5.74
	$Ca_{(k)}$	3.45	1.41
	$P_{(k)}$	1.58	0.83
	$Au_{(k)}$	10.71	0.89
Chitosan$_{NH2}$: MWCNT: nHA = 2:1:2 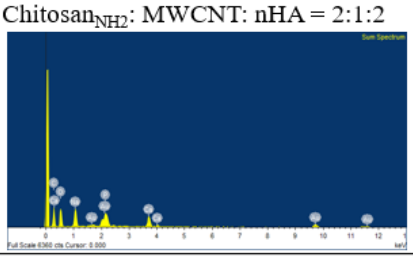	$C_{(k)}$	40.67	55.67
	$O_{(k)}$	36.26	37.29
	$Na_{(k)}$	4.52	3.23
	$Ca_{(k)}$	4.17	1.71
	$P_{(k)}$	2.01	1.07
	$Au_{(k)}$	12.33	1.03

We determined that for the Chitosan$_{NH2}$: nHA = 1:1 sample, Ca/P = 1.69, and for the full composite, Ca/P = 1.59. Note that both values are within the expected values for hydroxyapatite (TAVONI et al., 2021) stable apatite crystals, considering the experimental errors of both the synthesis and the EDS analysis. Therefore, it also confirms that the nHA is not degraded during the formation of the composites.

4.4 Thermal Analyses (TG and DTA), Swelling Tests, and Degradation Analysis

4.4.1 TG/DTA and Swelling Tests

From the first onset on the TGA curves, shown in **Fig.14(A)**, we observe that MWCNT holds a larger content of water in comparison with nHAP. Namely, the mass losses around 150 °C of pure chitosan and the sample with Chitosan$_{NH2}$: MWCNT = 2:1 were 33% and

30%, respectively, whereas the sample with Chitosan$_{NH2}$:nHA = 1:1 presented a mass loss of 12% at the same temperature. It is probably due to hydrogel mineralization by hydroxyapatite nanoparticles, which are more prone to interacting with chitosan than MWCNT when nHA concentration is higher, as demonstrated by the FTIR analysis. Meanwhile, the full composite (Chitosan$_{NH2}$: MWCNT = 2:1:2) also presented a 30% mass loss at 150 °C. Considering **Fig. 14(B)**, which depicts the DTA analyses, the peak around 130° C slightly shifts to a lower temperature for the carbon nanotube samples. Such endothermic peak dislocation indicates that water retention in the samples is directly affected by MWCNT interaction with chitosan, even though the difference between the mass loss is only 3%.

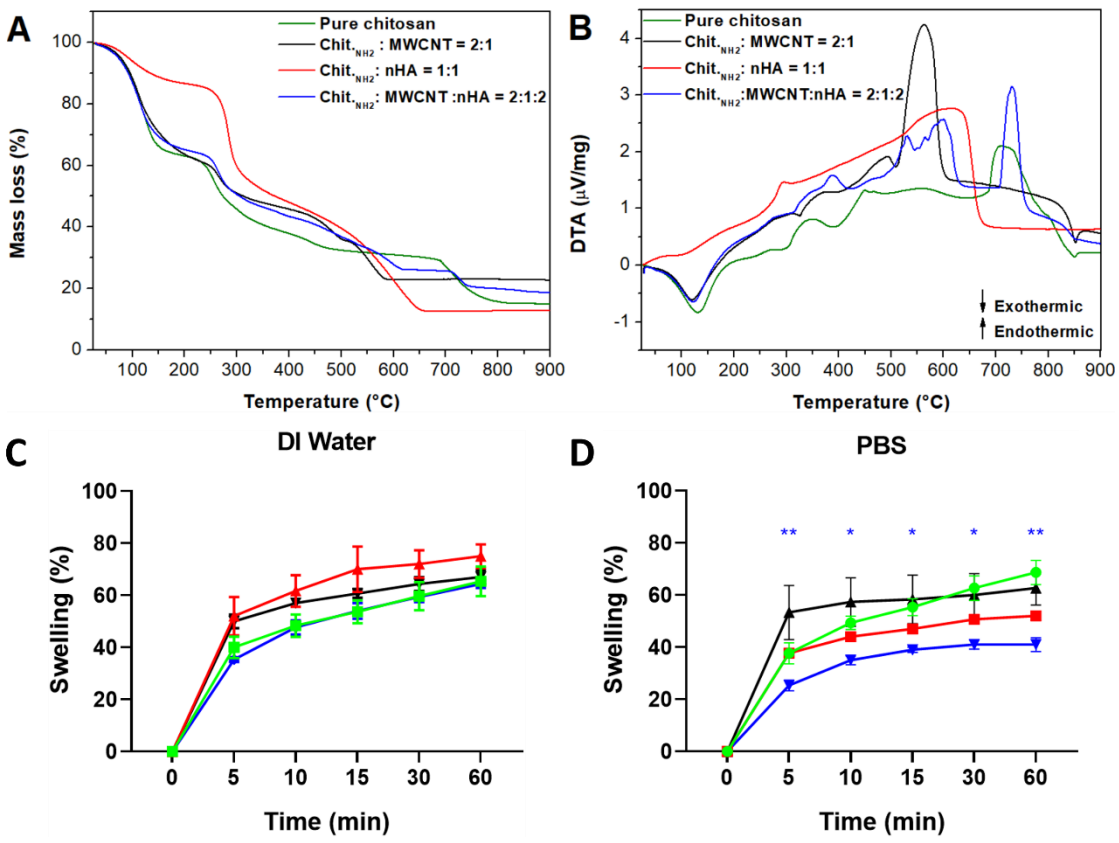

Figure 14: (A) Thermogravimetry and (B) Differential Thermal Analysis (TGA/DTA) of all the chitosan hydrogel conditions, where the investigated temperature range is between 25 °C and 900 °C, with an air-room atmosphere and a 10 °C/minute temperature ramp. Also, we show the swelling properties of chitosan hydrogels when challenged with (C) deionized water [DI] and (D) PBS [10 mmol/L, pH – 7.4]. The statistical analysis was obtained using n=3, where all samples passed Tukey's normalization test and were evaluated by Two-Way ANOVA for the quantitative swelling test for comparison regarding time and compound concentration, where $\alpha = 0.05$, and p*<0.05 and p**< 0.01 were considered significant.

Next, moving to higher temperatures in the thermal analysis, a second relevant mass loss event between 250° C and 350° C occurred for all the samples, which are 25% for Chitosan$_{NH2}$:nHA = 1:1 and around 10% for the other samples. The endothermic peaks in such temperature range are related to the depolymerization of chitosan chains, associated with the degradation of amine or N-acetyl groups (CARSON et al., 2009; ROGINA; IVANKOVI; IVANKOVI, 2013; TÜRK et al., 2018). From 400° C to 650° C, the exothermic peaks around 550 °C refer to the burning of residual organic groups for pure chitosan and functional groups containing oxygen (OH and COOH) from MWCNT and (PO_4 and OH) nHA. (CHATTERJEE; LEE; WOOA, 2010; LIANG; LI; TIAN, 2016; RATH et al., 2012a; TÜRK et al., 2018). Here, we have a remarkable change in the burning profile of Chitosan$_{NH2}$: MWCNT: nHA = 2:1:2 hydrogel. The broad exothermic peaks shown at the DTA curves from the MWCNT- and nHA bearing systems became solved into minor ones. Interestingly, the presence of nHA in the full composite allows for maintaining a degradation peak above 700 °C from pure chitosan hydrogel (TÜRK et al., 2018), which was lost in the system only bearing the nanotubes.

Fig. 14(C) presents the short-term swelling tests of all synthesized hydrogel formulations. The experiments were conducted either in deionized water or 10 mmol/L PBS. In **Fig. 14(C, D)**, the swelling test quantification reveals that all dried samples initially demonstrated rapid, short-term hydration regardless of the solvent type, increasing by 25% to 50% where the hydrogels present more evident distinguishment when challenged with PBS 10 mmol/L. After 5 minutes, the hydration pace slowed, but the samples swelled proportionally over time. No significant differences were observed when hydrogels were challenged with DI water. However, formulations containing nHA showed considerable differences under PBS conditions due to ionic charge perturbation in the modification sites, even though only the full composite is considered statistically relevant compared to pure chitosan hydrogel. Also, the swelling tests provide insights regarding solvent uptaking, showing that its feature could be essential for future applications where chitosan hydrogels should quickly internalize cells to host them safely before their proliferation and differentiation.

Let us analyze the swelling and thermal properties in a broad overview based only on the samples containing nHA in the first place. From the thermal perspective, the composite shows higher water content based on the presented mass loss values around 130° C, while the nHA-bearing hydrogel has the lowest. In the swelling analysis, the

$Chitosan_{NH2}$: nHA = 1:1 sample corroborates with it when challenged by the PBS solution, while the composite shows the opposite behavior. The interaction between chitosan and nHA seems prone enough to be sensitive to water recruiting regulation since its swelling rate was significantly high during the DI water swelling monitoring. On the other hand, the composite swelling rate was even more sensitive to this after the PBS challenge. Now, bringing the spectral data set with these results, both the indicative of formed physical adsorption and hydrogen bonding formation when MWCNT and nHA are coexisting within chitosan hydrogel could explain such features of the composite. Meanwhile, hydroxyapatite nanoparticle concentration was high enough to induce changes in the thermal and swelling features of nHA-bearing hydrogel but not necessarily from the spectral point of view, which was only in the samples having nHA excess. Expanding our discussion by looking at the other analyzed hydrogels, the thermal analysis shows that the exothermic peak present only in pure chitosan and composite around 700° C could indicate MWCNT and nHA interactions preference, leading carbon nanotubes play guidance for nHA deposition along the MWCNT carbon backbone structure (CANCIAN et al., 2016). Besides, the composite SEM analysis with higher magnifications also suggests this, where those particle-like shapes indicate and highlight morphologically such synergistic effects between MWCNT and nHA.

Based on these comments, our initial hypothesis regarding the theoretical composite network formation (see **Fig.4 and 5**) was not that accurate, and a close approach of what occurs at the end of 3 hours of synthesis and using 37 °C temperature, of chitosan-MWCNT-nHA reinforced hydrogel is depicted below in **Figure 15**:

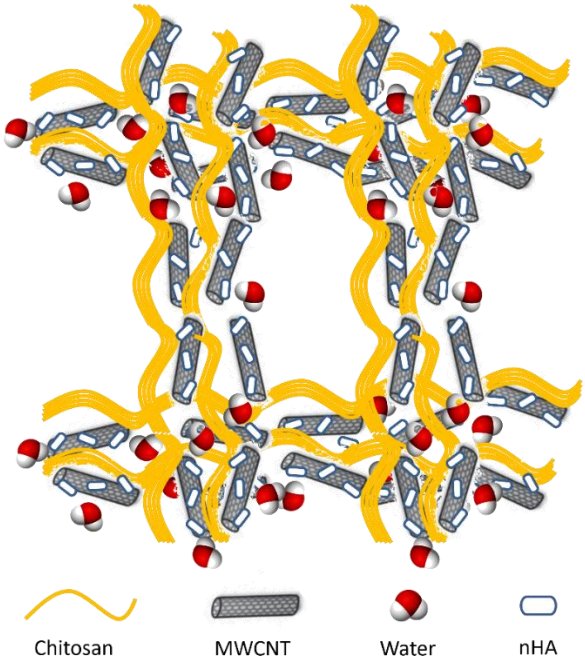

Figure 15: More reliable approach chitosan-reinforced hydrogel network conformation by MWCNT and nHA nanoparticles.

4.4.2 Long-Term Degradation Assay

Before leading the Chitosan$_{NH2}$: MWCNT: nHA = 2:1:2 hydrogel to the gene expression to investigate the differentiation and ECM, we performed a degradation assay using MEM-α cell culture medium. Next, **Figure 16** shows the pure chitosan and composite hydrogel monitoring for 7 days:

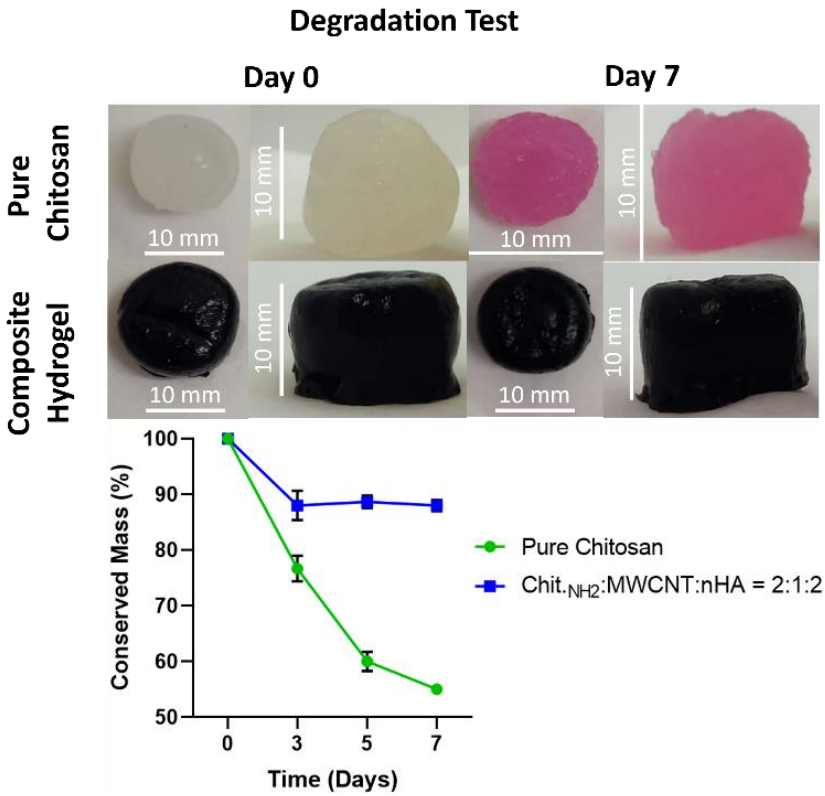

Figure 16: Degradation monitoring of Pure chitosan and Chitosan$_{NH2}$: MWCNT: nHA = 2:1:2 synthesized hydrogels for 7 days using 37° C temperature controlled by warming bath and immersed in MEM-α cell culture medium.

As shown above, the long-term degradation test shows that on Day 3, both hydrogels had a significant mass loss of around 25% and 12% for pure chitosan and Chitosan$_{NH2}$: MWCNT: nHA = 2:1:2 hydrogels, respectively. However, between Day 3 and 7, the composite hydrogel remained stable with no mass loss variation for the rest of the evaluation period. It shows that the chitosan reinforcement by MWCNT and nHA assisted in hydrogel conservation. Meanwhile, pure chitosan hydrogel kept losing its mass at 20% between days 3 and 5 and another 5% on day 7. Note that on Day 7, an error bar is absent due to the complete collapse of 2 of 3 samples triplicate, indicating the fragile structure of pure chitosan hydrogel for longer embedding in cell culture medium since it was not modified with MWCNT and nHA. Regarding Chitosan$_{NH2}$: MWCNT: nHA = 2:1:2 hydrogel, there was an indication of starting to lose its shape and structure during the solvent removal process of mass monitoring after Day 7, explaining no longer degradation monitoring data. It also means that for its potential applicability as a bio-ink, greater stability must be achieved for native bone tissue surrounding a lesioned area to replace the biomaterial at the correct pace.

4.5 *in vitro* Properties

4.5.1 Adhesion and Viability of Pre-Osteoblast Cells Screen Test

After physicochemical analyses, the composites were 24-hour incubated in α-MEM cell culture media to conditionate as preconized by the ISO 10933-5 guidelines. Afterward, the conditioned media were used to further subject pre-osteoblast cells (MC3T3-E1) for 24 h and 72 h to evaluate whether the released molecules in cell media were able to affect osteoblast adhesion and its cytotoxicity (mitochondrial activity), as shown in **Fig. 17**.

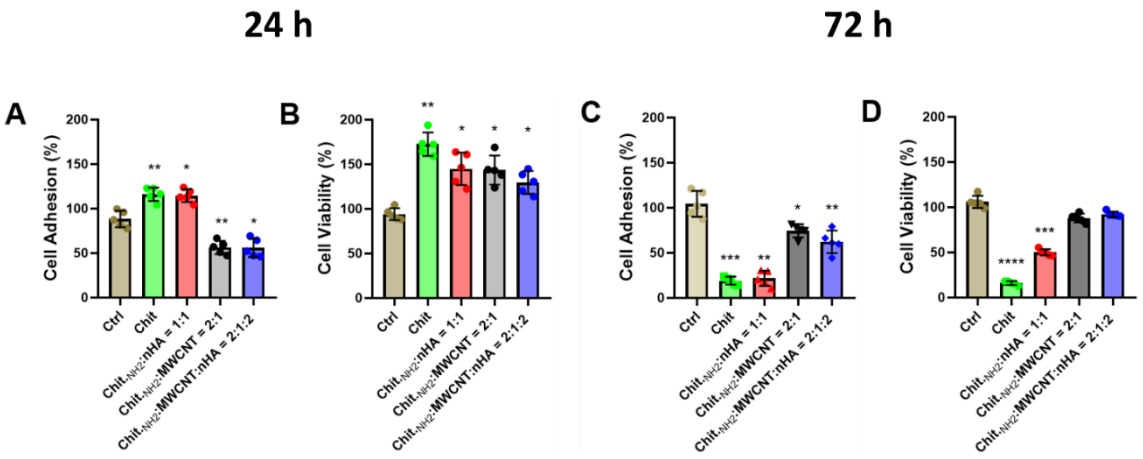

Figure 17: Cell adhesion (Crystal-Violet staining) and viability (MTT staining) challenging the MC3T3-E1 pre-osteoblast line with 24-hour α-MEM pre-conditioned cell culture media using colorimetric evaluation and compared against control groups between 24 h and 72 h time points. Statistical analysis was obtained using n=5, where all samples passed Tukey's normalization test. It was evaluated by regular ANOVA for the quantitative swelling test and cell investigation, respectively, where α = 0.05, Tukey normality test, and p*<0.05, p**<0.01, p***<0.001, and p****<0.0001 was considered significant.

At 24 hours, pure chitosan and $Chitosan_{NH2}$: nHA = 1:1 conditioned cell media exhibits an increased cell adhesion and mitochondrial activity, while $Chitosan_{NH2}$: MWCNT = 2:1 and $Chitosan_{NH2}$: MWCNT: nHA = 2:1:2 presented a significant effect on cell viability and adhesion. On the other hand, at 72 hours, cell adhesion and mitochondrial activity decreased substantially for pure chitosan. They remained low for $Chitosan_{NH2}$: nHA = 1:1. Conversely, the adhesion and mitochondrial activity of cells

treated with Chitosan$_{NH2}$: MWCNT = 2:1 and Chitosan$_{NH2}$: MWCNT: nHA = 2:1:2 conditioned media, demonstrated being very close to the performance of osteoblast adhering on the polystyrene, here used as a positive control. In turn, at least considering an indirect strategy to challenge the cells, HA and MWCNT seem to improve chitosan's biocompatibility. Based on our findings, molecules released from chitosan hydrogel formulations may negatively impact the metabolism of osteoblasts. It could be because these formulations potentially uptake nutrients from the media during the conditioning step, compromising cell viability.

In contrast, for the other hydrogel-conditioned cell media, released MWCNT molecules may lead to low cell adhesion of pre-osteoblast cells. This effect is likely due to the cytotoxicity of MWCNTs, as described previously, and simultaneously enhanced mitochondrial activity to compensate for low cell adherence as a survival mechanism (FUJITA et al., 2020). At 72 hours, since the cell media is not refreshed during this period, the nutrient concentration reaches its limit, explaining the low performance of the conditioned cell media with pure chitosan and Chitosan$_{NH2}$: nHA = 1:1 hydrogels. However, the observed robustness in adhesion and viability of pre-osteoblast cell layers treated with Chitosan$_{NH2}$: MWCNT = 2:1 and Chitosan$_{NH2}$: MWCNT: nHA = 2:1:2 hydrogels at 72 hours requires further explanation. This suggests another perspective: the specific properties of MWCNTs, such as their structure, surface area, and interaction with other components in the hydrogel, might play a crucial role. Additionally, the smaller diameter of these MWCNTs could facilitate cellular uptake, reducing cytotoxicity and thereby enhancing cell viability and adhesion over time.

4.5.2 Proliferation, Differentiation, and Extracellular Matrix Remodeling Gene Markers Monitoring

4.5.2.1 Proliferation

After the cell adhesion and mitochondrial activity of MC3T3-E1 cell line evaluation, we harvested the pre-osteoblasts for the conditioned media treatment to monitor the proliferation phenomena. It regards the effects of the released byproducts from the synthesized hydrogels using the pre-conditioning step qPCR per the ISO 10993-5 guidelines by RT-qPCR monitoring. We evaluated the Cyclin-dependent Kinases (CDK-2, -4, and -6), Cyclin-dependent Kinase Inhibitor (p15), and Focal Adhesion Kinase

(FAK) gene markers. All of these kinase monitoring bring insights into the cell cycle regarding the proliferation behavior of the pre-osteoblast, as shown in **Figure 18:**

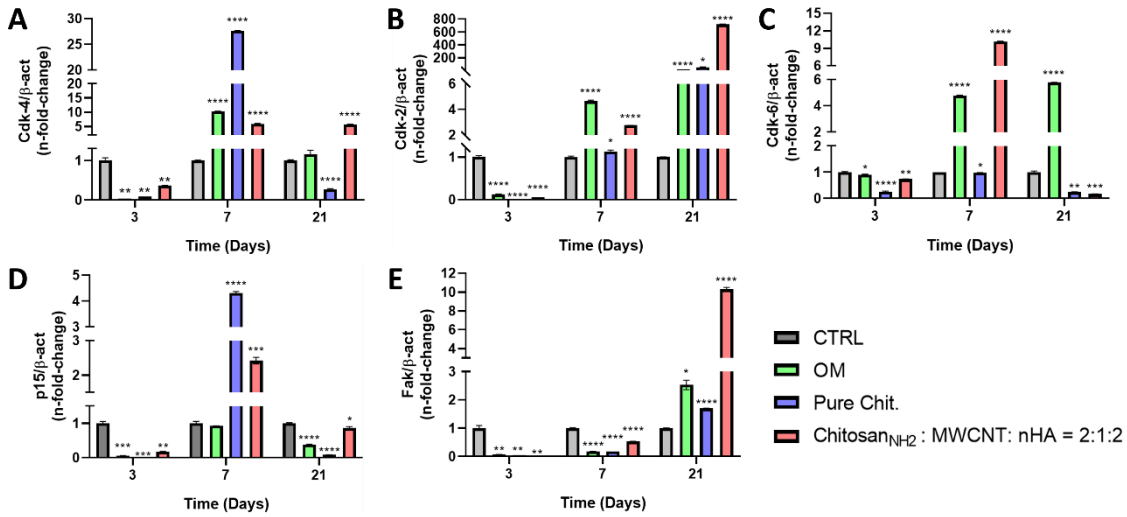

Figure 18: n-fold-change gene expression of differentiation markers, using β-actin as housekeeping: (A) Cdk-4, (B) Cdk-2, (C) Cdk-6, (D) p15, and (E) Fak, evaluated by RT-qPCR during 3, 7, 14, and 21 days. Statistical analysis was obtained using n=3, where all samples passed Tukey's normalization test and were evaluated by Two-Way ANOVA, where $\alpha = 0.05$, and p*<0.05, p**<0.01, p***<0.001, and p****<0.0001 was considered significant.

Firstly, let us discuss the monitoring overtime of Cdk gene expressions after pre-osteoblast treatment by the conditioned cell media by synthesized hydrogels, as shown in **Fig. 18 (A – C)**. Cdk-4 expression reached the highest peak of activity on Day 7 for all the treatments, especially for the pure chitosan group, followed by the composite hydrogel data that remained increased on Day 21, about 27 and 10 fold-change, respectively. Next, Cdk-6 showed a similar result on Day 7, where the osteogenic medium treatment showed high activity in the late period of gene expression, also noticing the downstream expression for the composite hydrogel groups simultaneously. Meanwhile, the Cdk-2 expression presented the highest values among the investigated CDK genes on Day 21, with about 200 fold-change for osteogenic media and pure chitosan-treated groups and 800 fold-change for the composite hydrogel. Moving to the inhibitor of CDK, the p15 gene expression trend closely followed the CDK-4 expression, even though it had a diminished intensity of only about 4.5 fold-change. Lastly, the FAK gene expression

showed a later activity only on Day 21, highlighting the composite hydrogel treatment with about 10 fold-change in intensity activity.

As mentioned in the introduction, the investigated CDK's gene markers are crucial in cell cycle regulation. CDK-2 partners with cyclin E and A to control the G1 to S phase transition, while CDK-4 and CDK-6, in association with cyclin D, are pivotal for the early G1 phase progression. Various extracellular signals, including growth factors and ECM components, tightly regulate the expression levels and activities of these CDKs. CDK-2 is typically activated later in the cell cycle (G1/S phase), while CDK-4 and CDK-6 are involved earlier, suggesting that the changes in the ECM induced by the hydrogels could impact the initial stages of cell cycle entry and proliferation. Looking at our data set of CDK gene expressions, the conditioned cell media by the samples' behavior according to expectations, highlighting the osteogenic media and the composite hydrogel, where both early and late CDK markers indicate that the pre-osteoblast proliferation is occurring managed by p15 gene. The p15 CDK's inhibitor binds to CDK4/6-cyclin D complexes. It acts similar as a tumor suppressor by inducing cell cycle arrest at the G1 phase. One could argue that the upregulation of p15 would suggest an anti-proliferative response, potentially in reaction to toxic byproducts or unfavorable conditions caused by the hydrogel components, and conversely, its downregulation could indicate a pro-proliferative environment. However, since the expression of all investigated CDK genes is higher than that of p15, it seems more prone to controlling proliferation activity.

Another critical insight about the proliferation relies on the FAK gene expression. FAK is a non-receptor protein tyrosine kinase that integrates signals from the ECM to regulate cell migration, proliferation, and survival. FAK activation and its downstream signaling, involving pathways like PI3K/AKT and MAPK, can enhance cyclin D1 expression, promoting G1 phase progression and cellular proliferation. In response to the different hydrogel conditions, FAK may modulate how cells interact with their surroundings, influencing the proliferative signaling cascades to cell rearrangement in the bone matrix, especially in the results of the composite hydrogel on Day 21. FAK activation may further impact this balance by mediating downstream signaling that affects cyclin expression and CDK activity. Modifications in bone ECM caused by different hydrogel formulations might alter FAK signaling, either promoting or inhibiting cell proliferation.

4.5.2.2 Differentiation

In order to evaluate the differentiation mechanism, we harvested the pre-osteoblasts and subjected them to the conditioned media separately to further allow gene expression analyses by qPCR per the ISO 10993-5 guidelines. Then, we show the evaluation of Alkaline Phosphatase (Alp), Transforming Growth Factor Beta 2 (Tgf-β2), Runt-related transcription factor 2 (Runx2), Osteopontin (Opn), Osteocalcin (Bglap), and Collagen Type I Alpha 1 (Col1a1) genes. These osteogenic gene markers are essential to drive osteogenic phenotype for up to 21 days, as shown in **Figure 19**:

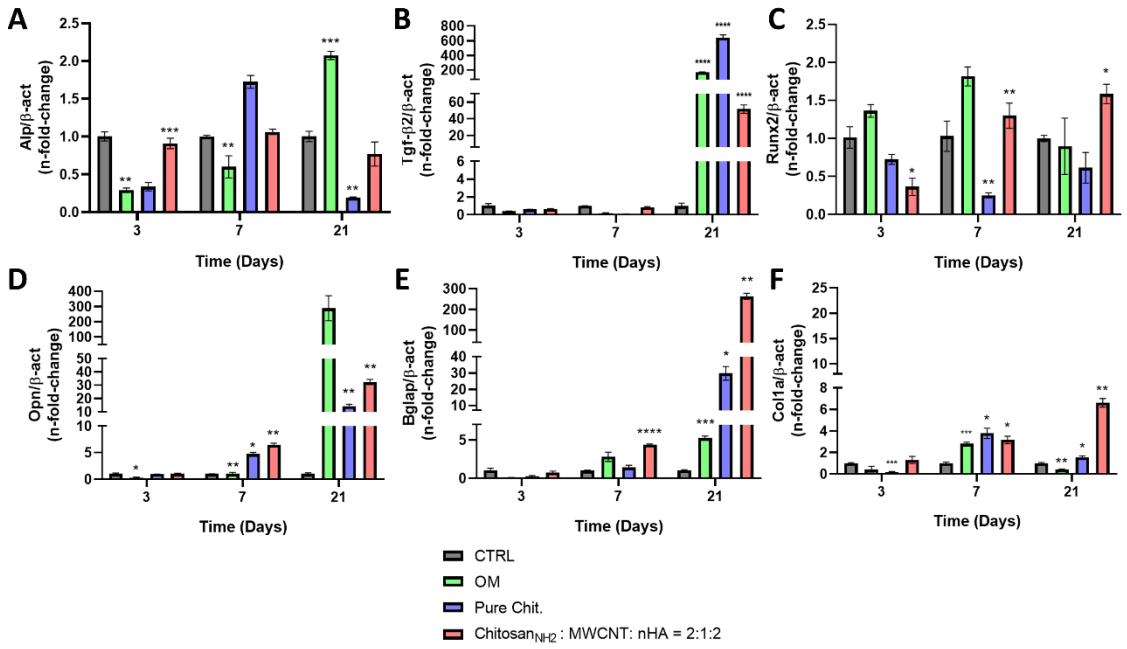

Figure 19: n-fold-change gene expression of differentiation markers, using β-actin as a housekeeping: (A) Alp, (B) Tgf-β2, (C) Runx2, (D) Opn, (E) Bglap, and (F) Col1a1, evaluated by RT-qPCR during 3, 7, 14, and 21 days. Statistical analysis was obtained using n=3, where all samples passed Tukey's normalization test and were evaluated by Two-Way ANOVA, where $\alpha = 0.05$, and p*<0.05, p**<0.01, p***<0.001, and p****<0.0001 was considered significant.

Fig. 19(A) shows the Alp gene expression by the challenged pre-osteoblast cells with the conditioned cell media by pure and composite hydrogels. Notably, the osteogenic medium is used as a positive control of the osteoblast differentiation, and it increased Alp expression, while pure chitosan showed a high expression peak on day 7, which decreased afterward. The composite treatment changes in osteoblasts presented no significant

changes compared with the control group during the monitored period, showing that its molecules do not interfere with the Alp marker expression. **Fig 19(B)** shows the results regarding Tgf- β2 expression, which only has significant changes in its expression after 21 days of treatment. Surprisingly, the increases were about 200-, 600-, and 60-fold changes for osteogenic medium, pure chitosan, and composite cell treatment, respectively. In this case, it seems that the MWCNT and nHA released molecules from the composite drive the expression of Tgf- β2 compared to pure chitosan, even though the increase is remarkable and significantly higher than the control group. For Runx2 expression [**Fig. 19(C)**], the increased strength occurred similarly to that detected in Alp. Cells treated with osteogenic medium were almost 2 times higher than control on Day 7, pure chitosan remained low for the whole period, and the composite had the best performance among them, increasing the Runx2 expression by 1.5 times at Day 21. Considering the pure and composite hydrogel formulations, MWCNT and nHA byproducts positively affected the slightly Runx2 gene expression.

Fig. 19(D) shows the significant expression of Opn started on Day 7, reaching about 250-, 10-, and 30-fold change on Day 21 for osteogenic medium, pure chitosan, and composite cell treatment, respectively. Here, the effects of MWCNT and nHA molecules on cells were 3 times higher than those of pure chitosan. In the same way, in **Fig. 19(E)**, the osteocalcin (Bglap) gene expression also started on Day 7, where the osteogenic medium and the composite treatment had a remarkable increase until Day 21, highlighting the composite treatment that improved osteocalcin expression by about 250 times higher than control. Finally, the Col1a1 expression is shown in **Fig. 19(F)**, where osteogenic medium and pure chitosan had about 4 and 15 times, respectively. Meanwhile, the composite treatment had a later significant expression of Col1a1 only on Day 21.

The regulation of ALP, TGF- β2, RUNX2, osteopontin, osteocalcin, and COL1A1 in MC3T3 pre-osteoblasts involves a complex interplay of transcription factors, signaling pathways, and feedback mechanisms. RUNX2 is central to this regulatory network, influencing the expression of ALP, OPN, BGLAP, and COL1A1. Indeed, our differentiation data set corroborated it, especially when looking at pure chitosan and composite treatments. Even though RUNX2 did not have the overexpression as the others, its influence on the expression of osteopontin, osteocalcin, and COL1A1 has been remarkably noticeable (KOMORI, 2019). Such a higher expression of these genes shows

that MWCNT and nHA and their respective released byproducts to the cell culture media significantly impact the modulation of pre-osteoblast differentiation. Also, one of the reasons that could lead to the low increase in Runx2 expression is the high expression of TGF- β2 and BMP-2(GOMATHI et al., 2020; JANN et al., 2020). There is a loop between these two genes where RUNX2 upregulates TGF-β2, and its reduced gene expression can explain the TGF-β2 high gene activity. However, Osterix, Mapk, and Smads family gene expression investigations are required to ensure it (CARREIRA et al., 2014; GE et al., 2009; LI et al., 2022).

As noticed, RUNX2 is pivotal in osteoblast differentiation by directing the commitment of multipotent mesenchymal cells to the osteoblastic lineage and regulating the expression of various osteoblast-specific genes. RUNX2 activates the transcription of ALP, OPN, BGLAP, and COL1A1, which are crucial for different stages of osteoblast differentiation. Also, in this regard, RUNX2-deficit leads to a complete lack of bone formation, affecting osteoblast activity and making it a central integrative node in the osteogenic signaling network. Also, its secreted levels reach a maximum in immature osteoblasts and are down-regulated in mature ones, making it a good marker for early detecting differentiation events (KOMORI, 2010, 2019). In turn, BGLAP is a non-collagenous protein secreted by osteoblasts and is considered a late marker of osteoblast differentiation by regulating bone mineralization and energy metabolism (KARSENTY; FERRON, 2012). BGLAP expression is enhanced by RUNX2 activity during the late stages of differentiation, indicating mature osteoblast activity. The BMP pathway also regulates BGLAP and is responsive to hormonal signals such as vitamin D and insulin (KARSENTY, 2017). Then, BGLAP's role extends beyond bone metabolism, implicating it in systemic energy regulation.

Meanwhile, osteopontin is a multifunctional glycoprotein involved in bone remodeling and cell-matrix interactions. It bridges osteoblasts and the mineralized matrix, playing a significant role in endocrine regulation and the early stages of mineralization (SI et al., 2020). OPN expression is upregulated by RUNX2 and is involved in the adhesion of osteoblasts to the bone matrix. OPN is regulated by integrin and CD44 signaling pathways, which are influenced by TGF-β and BMP signaling, underlining its role in the cellular responses during bone formation (VANCEA; SERBAN; FODOR, 2021).

Additionally, Transforming Growth Factor Beta 2 (TGF-β2) is a member of the TGF-β superfamily involved in regulating cell proliferation, differentiation, and ECM production (LI et al., 2022). Tgf-β2 signaling through the Smad pathway interacts with other pathways, such as BMP and/or Wnt, integrating various signals to promote osteoblast differentiation. TGF-β2-related role expands to maintaining the balance between osteoblast and osteoclast activity, which is critical for bone remodeling (JANN et al., 2020). TGF-β2 can trigger autocrine signaling in osteoblasts and potentially the Runx2 gene activity, thereby influencing the expression of COL1A1 and ALP. ALP is one of the earliest osteoblast differentiation markers. It is an enzyme that hydrolyzes phosphate esters, providing inorganic phosphate necessary for hydroxyapatite crystal formation, a crucial component of bone mineralization (VIMALRAJ, 2020). Alp expression is directly upregulated by RUNX2 and further enhanced during osteoblast maturation. (LIU et al., 2021). COL1A1 is a significant component of the bone ECM, providing structural support for mineral deposition. Runx2 and Tgf-β2 regulate COL1A1 expression, continuously expressed throughout osteoblast differentiation (AMARASEKARA; KIM; RHO, 2021). The regulation of COL1A1 by TGF-β, BMP, and Wnt signaling pathways ensures proper ECM formation and mineralization, which is crucial for bone strength and integrity. It is also essential for forming the organic bone matrix as a scaffold for hydroxyapatite crystals (CARREIRA et al., 2014).

4.5.2.3 Extracellular Matrix Remodeling: Gene Expression

Next, to understand whether these new formulations could modulate ECM remodeling, we have evaluated two approaches: gene expression of biomarkers of ECM remodeling and the activity of MMPs. Also, in this scenario, Bone morphogenic protein 2 (Bmp-2), Bone sialoprotein (Bsp), and Tissue inhibitor of matrix metalloproteinase (Timp-1 and Timp-2) were investigated. The Bmp-2 and Bsp genes can also be related to pre-osteoblast differentiation, although they also play an essential role in ECM remodeling and mineralization. BMP-2 is a growth factor in the TGF-β superfamily, playing a necessary role in bone formation and osteoblast differentiation. It induces the expression of osteogenic markers and stimulates the production of ECM proteins. Bmp-2 signaling occurs via Smad-dependent and Smad-independent pathways, leading to the transcription

of osteogenic genes (CARREIRA et al., 2014; WAGLEY et al., 2020). Bmp-2 upregulates the expression of crucial ECM components, including collagen type I, osteopontin, and osteocalcin. It enhances the expression of Mmps, particularly MMP-2 and MMP-9, facilitating ECM degradation necessary for cell migration and tissue remodeling (LIN et al., 2020).

Besides, the role of BMP-2 in forming other tissues, such as cardiac and neuronal, is reported elsewhere (HALLORAN; DURBANO; NOHE, 2020). Another essential protein related to the ECM and regulated by BMP-2, BSP, is a non-collagenous protein highly expressed in mineralized tissues. It has a high affinity for hydroxyapatite, promoting ECM mineralization. BSP facilitates the nucleation of hydroxyapatite crystals, which are critical for bone mineralization. It interacts with integrins, influencing cell adhesion, migration, and signaling pathways involved in osteoblast differentiation. Bmp-2 and other osteogenic signals regulate Bsp expression, integrating the processes of ECM remodeling and mineral deposition (CHAVEZ et al., 2023).

MMP-2 and MMP-9 are gelatinases involved in the degradation of collagen and gelatin, critical for ECM remodeling. They are produced as inactive proenzymes and activated extracellularly. MMP-2 and MMP-9 are gelatinases involved in the degradation of collagen and gelatin, critical for ECM remodeling. MMP-2 primarily degrades type IV collagen, a significant basement membrane component, facilitating cell migration. Mmp-9 degrades type I and type IV collagen, playing a role in the initial and later stages of bone formation (KHOSWANTO, 2023; LI; TAY; YIU, 2020). The activity of MMP-2 and MMP-9 is essential for removing ECM barriers, allowing osteoblasts to proliferate and differentiate. TIMP-1 and TIMP-2 are natural inhibitors of Mmps, controlling ECM degradation by binding to active MMPs and preventing their proteolytic activity (PRIDEAUX et al., 2015; XI et al., 2020). Timp-2 specifically inhibits MMP-2 and also regulates the activation of pro-MMP-2. The balance between MMPs and TIMPs is critical for controlled ECM remodeling, ensuring proper osteoblast function and bone formation (SHIBUTANI et al., 1999). Next, **Figure 20** illustrates the differentiation gene expression markers monitored for 21 days of the treated pre-osteoblast cells.

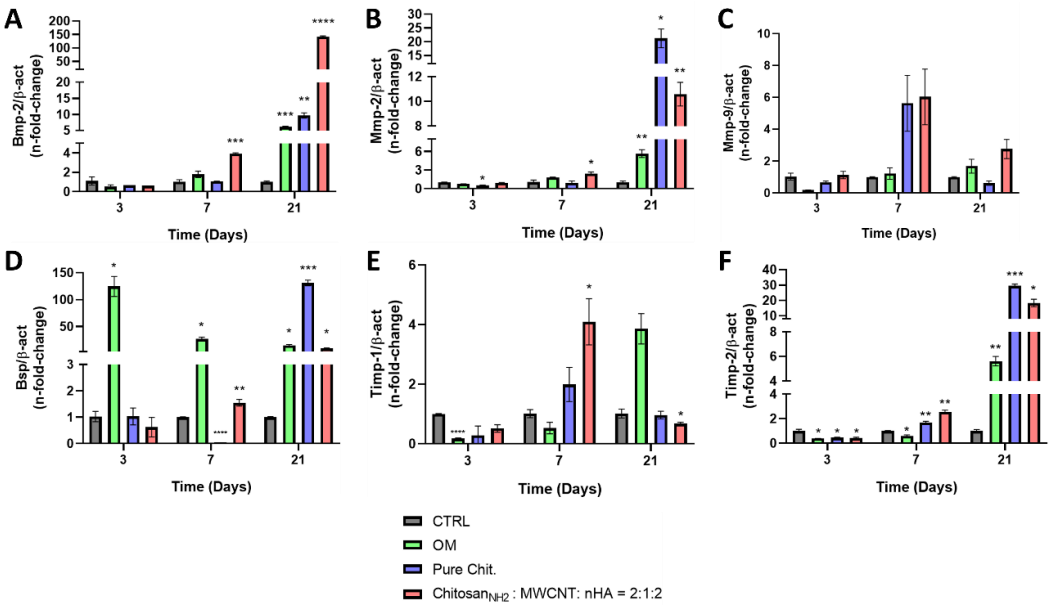

Figure 20: n-fold-change gene expression of ECM remodeling gene markers, using β-actin as housekeeping: (A) Bmp-2, (B) Mmp-2, (C) Mmp-9, (D) Bsp, (E) Timp-1, and (F) Timp-2, evaluated by RT-qPCR during 3, 7, 14, and 21 days. Statistical analysis was obtained using n=3, where all samples passed Tukey's normalization test and were evaluated by Two-Way ANOVA, where $\alpha = 0.05$, and p*<0.05, p**<0.01, p***<0.001, and p****<0.0001 was considered significant.

Fig. 20(A) shows the Bmp-2 gene expression, poorly expressed on Day 3, with a slight increase on Day 7, and overexpressed on Day 21, which remarkably, the composite hydrogel had almost 125 times higher expression than the control group, and about 10 times higher than the pure chitosan and osteogenic medium. The direct influence of Bmp-2 in Mmp-2 and Mmp-9 expression is also suggested in their gene expression, depicted in **Fig. 20 (B, C)**. Mmp-2 was only overexpressed on Day 21 when the pure chitosan treatment showed about a 25-fold change, and the composite treatment also presented remarkable results. Regarding the Mmp-9, no statistical significance was detected up to 21 days, even though on Day 7, the pure chitosan and composite hydrogel treatment was shown to be about 6 times higher than the control group, also highlighting the composite performance on Day 21, which expression remained increase about five times higher than control. Besides, it is interesting to note that Bmp-2 and Mmp-2 seem to affect osteoblasts directly.

Regarding Bsp gene expression [**Fig. 20(D)],** osteogenic medium treatment has the most significant effect in its expression, at about 125-fold change on Day 3, which decreased to 25-fold on Day 21. Pure chitosan and composites treatment significantly

increased up to Day 21, highlighting hydrogel with no modification, which reached about 125-fold change. Additionally, the composite treatment affected the Bsp expression gene on Day 21, which remained highly expressed at the same level as the osteogenic medium. **Fig. 20 (E, F)** brings the expression of tissue inhibitors of metalloproteinases Timp-1 and Timp-2, which are changed up to 21 days and reinforces their relevance along osteoblast responding to chitosan-based hydrogels and it certainly affects bone remodeling during bone regeneration. Interestingly, it seems there is a positive correlation with the expression data obtained from the Mmps, where the expression of both Timp-1 and Timp-2 proportionally responds to the expression of Mmp-9.

In light of the comprehensive gene expression profile, several key genes stand out for their ability to influence others. Among these, BMP-2, TGF-β2, osteocalcin, osteopontin, BSP, MMP-2, and TIMP-2 are highlighted. BMP-2 promotes the expression of MMP-2 and MMP-9 (GORDON et al., 2009), which is crucial for ECM remodeling and the balance between MMPs and TIMPs. Notably, MMP-9 and its regulator TIMP-1 showed limited expression in our study. MMP-2 activity is finely regulated by cytokines like TGF-β2 and its inhibitor TIMP-2 (DEHNAVI et al., 2009). The balance between MMP-2 and TIMP-2 is critical for controlled ECM degradation and remodeling. TGF-β2 influences TIMP-2 expression and other cytokines, ensuring controlled matrix remodeling by modulating MMP-2 activity (DEHNAVI et al., 2009; ELDRED et al., 2012). TGF-β2 also stimulates and regulates BMP-2 (TOWNSEND et al., 2011), initiating preosteoblast differentiation into mature osteoblasts with assistance from osteocalcin, responding to calcium and phosphate ions crucial for bone mineralization.

TGF-β2 signaling is pivotal in upregulating gene expression during osteoblast differentiation, including osteopontin (NEUMANN et al., 2014). Osteopontin expression, stimulated by BMP-2 and TGF-β2, positively impacts osteogenic signals that upregulate osteocalcin expression, facilitating bone resorption and remodeling involving osteoclasts. BMP-2 and TGF-β2 also increase BSP expression, which is crucial for osteoblast adhesion to the bone matrix. This process involves osteogenic markers such as osteocalcin, osteopontin, and BSP, which play essential roles in bone matrix mineralization. Osteocalcin binds to hydroxyapatite, while BSP aids nucleation into mineral crystals (CHAVEZ et al., 2023; HUNTER; GOLDBERG, 1993).

Osteopontin, either early or late expressed in osteoblast differentiation, is also involved in cell adhesion, signaling, and bone remodeling, entering again into a loop with the ECM remodeling (DEPALLE et al., 2021). These are the feedback loops we believe take place where all overexpressed genes influence others' regulation. Interestingly, a conditioned medium by pure chitosan hydrogel and its reinforcement by MWCNT and nHA for bone application can induce positive cell signaling and regulation.

Considering our findings regarding the proliferation, differentiation, and ECM remodeling gene expression investigations, we hypothesize that a dynamic and active homogeneous bone cell population may present a heterogeneous phenotype. In a way where intercellular interaction may guarantee subpopulations of pre-osteoblasts phenotype-different induced by the respective treatment when using the conditioned cell media, remarkably noticed in the chitosan-MWCNT-nHA hydrogel. Our dataset indicates that cells are proliferating and differentiating concomitantly, governed by the high dynamic activity of metalloproteinases controlling bone ECM's remodeling and inducing its mineralization index, as demonstrated below. Such features are highly desirable and almost mandatory for the accurate recapitulation of the microenvironment from the point of view of bone regeneration (SHAIKH et al., 2023).

Looking for future potential applications of our composite hydrogel such as in additive manufacture techniques, all the previous investigations of proliferation, differentiation, and extracellular gene expression triggered by the conditioned cell media treatment following ISO 10993-5 guidelines, can: **(i)** screen potential biomaterial candidates for bio-ink application before cell incorporation, considering how its byproducts affect cell machinery; and **(ii)** since the conditioning of cell medium induces positive responses in cells, the very same medium can be used within now with the cell-laden biomaterial culture, to the improve cell adaption within scaffolds, in a similar way that many researchers do with stem cells growth and differentiation using media conditioning. Thus, we conceived the QP-BioScreen workflow based on both the indirect contact test by ISO 10993-5 guidelines and gene expression monitoring by RT-qPCR, which can provide long-term insights about potential biomaterial safety for bioink use and whether its released byproducts will affect cell proliferation and differentiation.

4.5.3 Metalloproteinase Activity

In addition to monitoring the gene expression of ECM remodeling-related genes, we now evaluated the Mmp-2 and -9 activities using the zymography assay to check whether those MMPs participate effectively in matrix remodeling in response to the hydrogels assessed here. **Figure 21** shows the inverted-colored gelatin-based gels of the conditioned media collected from cells up to Days 3, 7, 14, and 21. **Fig. 21(A)** shows the zymography gels with MMP activity spots corresponding to its gelatinolytic effect. Specifically, pro-Mmp-9 and Mmp-9 isoforms were detected between 92 and 86 KDa, and the pro-Mmp-2 and Mmp-2, between 76 and 62 KDa (KALEV-ALTMAN et al., 2022; WOOD et al., 2023). We can notice that regardless of the day of treatment, the activity of Mmp-9 was low compared to the Mmp-2. It corroborated with the monitored gene expression data where only Mmp-2 had significant expression.

Regarding the activity of gelatinase content of samples conditioned media, **Fig. 21(B)** shows that its quantification had only a significantly reduced difference in pure chitosan conditioned media gelatinase content for the Mmp-9. For the Mmp-2, augmented activity was noticed up to Day 21 for the osteogenic medium, pure chitosan, and composite-conditioned media gelatinase content, even though it was not statistically significant. Thus, we can suggest that although lower expressed by challenged pre-osteoblasts, Mmp-9 gelatinases in the samples' conditioned media are active and participate in ECM remodeling. Meanwhile, the overexpression of Mmp-2 shows that its activity is close to the control groups, differing only on Day 21.

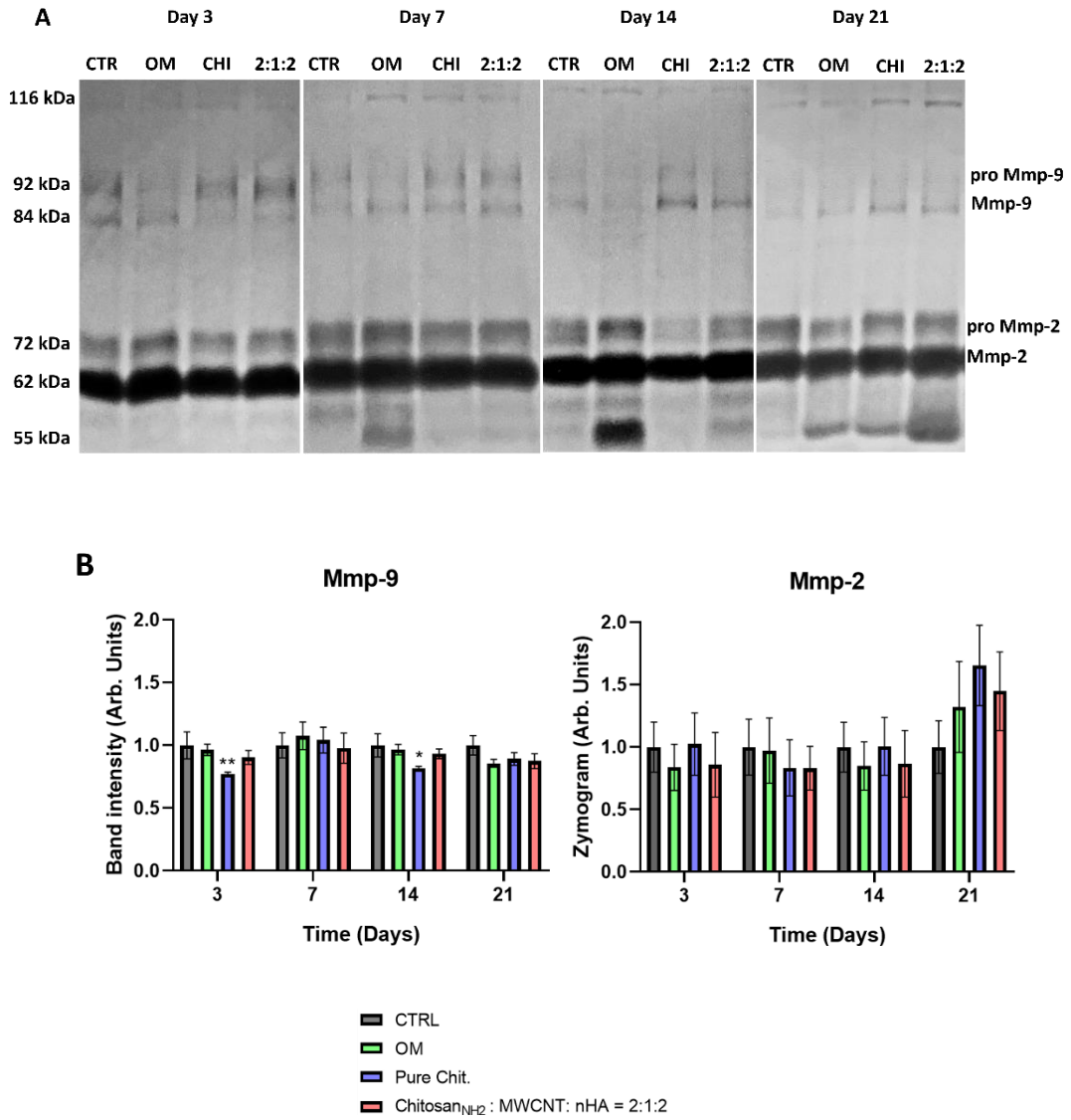

Figure 21: Metalloproteinase activities were evaluated using Zymography. The activities of both MMP2 and MMP9 were analyzed using (A) gelatin-containing gels—the zymogram depicting differences in (pro) MMP-2 and (pro)MMP-9 isoforms, and its respective (B) zymogram quantification of the identified bands.

Finally, zymography revealed unexpected protein bands at 116 kDa and 55 kDa across all investigated groups. The 116 kDa band likely represents MMP-9 complexes with other proteins, increasing its apparent molecular weight through interactions with tissue inhibitors of metalloproteinases (TIMPs) or other extracellular matrix (ECM) components (La Rocca et al., 2004; Oum'Hamed et al., 2004; Pucci-Minafra et al., 2001). The 55 kDa band may correspond to other MMP family members or different gelatinases, such as MMP-3 (Stromelysin-1), known for collagenase activity and degradation of proteoglycans and fibronectin (Chin; Murphy; Werb, 1985; Okada; Nagase; Harris, 1986). Importantly, MMP-3 can induce MMP-9 and MMP-2 and vice versa, playing a crucial role in connective tissues and stretch-induced modulation of osteoblast

mineralization (Chin; Murphy; Werb, 1985; Jansen et al., 2006; Ye et al., 1996). MMP-3 appeared in zymography from Day 7 onwards, initially in a conditioned osteogenic medium, decreasing gradually until Day 21. Conversely, composite conditioned media showed increased MMP-3 levels between Day 14 and 21, consistent with gene expression data and other MMP mappings in zymography, indicating its involvement in ECM remodeling alongside MMP-2 and MMP-9.

4.5.4 Mineralization

After investigating the differentiation and ECM remodeling gene expression, the conditioned cell media by pure chitosan and composite hydrogel were submitted to the pre-osteoblast cells to distinguish whether mineralization is affected, illustrated in **Figure 22**. Our data shows progressive mineralization between Day 3 and Day 21 for all treated groups, although the control group achieved lower than others regarding the calcium deposits. As expected, the ECM mineralization by cells treated with the osteogenic medium presented the better-concentrating calcium nodule regions stained by Alizarin Red S salt. However, the results showed that cells treated with the conditioned medium by pure chitosan and composite hydrogel achieved higher mineralization than the control. Remarkably, the composite hydrogel treatment also presented significant mineralization, with more distributed calcium nodule regions when compared with osteogenic medium, even though it is probably less concentrated in calcium content. Besides, it becomes clear that the conditioned medium by composite hydrogels containing MWCNT and nHA facilitated the calcium deposition compared to pure chitosan treatment. Noteworthy, we overcame some limitations in quantifying calcium optical density and handling the sample of Day 14. In the first case, the cell layer detached completely, and the cells were mixed entirely with media during the quantification protocol, which did not allow us to perform the calcium quantification protocol adequately.

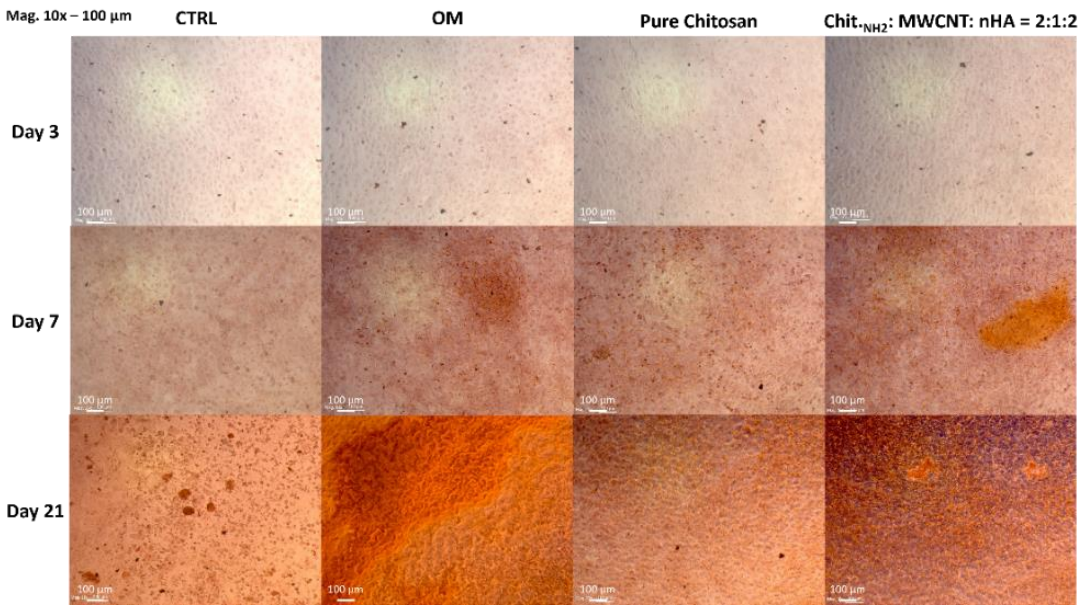

Figure 22: Optical microscopy for mineralization monitoring of MC3T3-E1 cells after culture with respective conditioned cell media, where CTRL = Control, OM = Osteogenic Media. Magnification: 10x.

5. CONCLUSION

This study successfully developed a cell-free chitosan hydrogel reinforced with multi-walled carbon nanotubes (MWCNT) and hydroxyapatite nanoparticles (nHA) for application in bone tissue engineering. The negative charges from MWCNTs obtained through an acid attack and ultrasonication process and the synthesized hydroxyapatite nanoparticles were successfully incorporated within the chitosan matrix, as confirmed by FTIR spectroscopy, which identified the dynamic interaction among the compounds. The hydrogels demonstrated good short-term swelling properties in deionized water and phosphate-buffered saline (PBS), although improving the hydrogel long-term degradation rates with cell culture medium is necessary. The thermogravimetric analysis further indicates that MWCNT and hydroxyapatite nanoparticles prefer interacting with each other compared to chitosan when coexisting during the formation of the composite hydrogel. Morphological analyses using Scanning Electron Microscopy (SEM) and Energy Dispersive Spectroscopy (EDS) quantification of Ca/P ratios of hydrogel containing hydroxyapatite showed the distribution of stable apatite crystals within chitosan hydrogel, indicating successful integration of nHA either in the presence or not of MWCNT. At the same time, biocompatibility tests using ISO 10933-5 guidelines

revealed high cell viability and firm adhesion of MC3T3-E1 pre-osteoblasts, underscoring the hydrogel's potential to support osteoblast activity and bone tissue regeneration. Gene expression analysis demonstrated upregulation of key osteogenic gene markers, suggesting that the hydrogel promotes osteoblast differentiation and extracellular matrix remodeling, supported by the confirmation of matrix metalloproteinases (MMPs) activity, which is crucial for ECM remodeling. We labeled such complementary approaches as Quarantine Protocol for Cell-free Bio-ink (QP-BioScreen), also extendable to other bio-ink formulations, where the chitosan-MWCNT-nHA hydrogel was demonstrated to be environmentally safe for 21 days. After monitoring, such protocol can address further assistance with 3D-cell-laden scaffold applications, where using a conditioned cell culture medium by the same cell-free hydrogel can potentially speed up cell adaptation, proliferation, and differentiation.

6. APPENDIX SECTION

6.1 Appendix 1 - Full FTIR Spectra of Pure Chitosan, MWCNT, and nHA

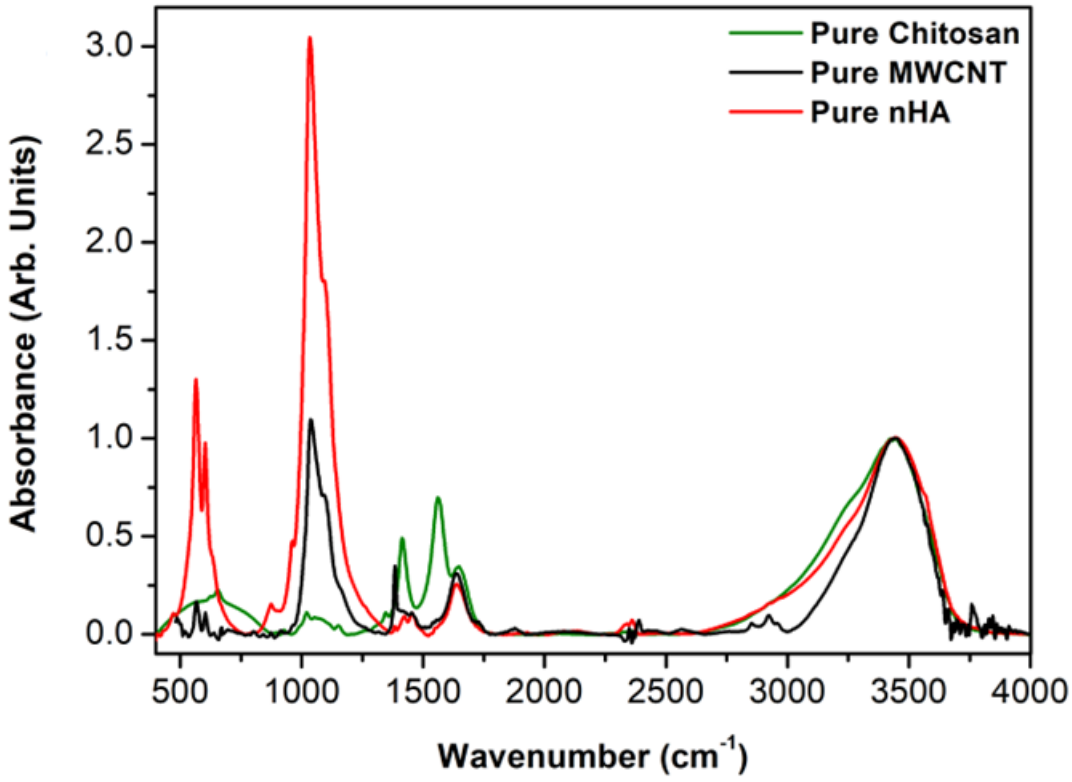

Figure A1: FTIR spectra of pure chitosan, MWCNT, and nHA, between (A) 500 cm^{-1} and 4000 cm^{-1}.

6.2 Appendix 2 – Studying Abroad Program at Wake Forest Institute for Regenerative Medicine

This section partially reproduced the submitted and approved activity report to the São Paulo Research Foundation (FAPESP) regarding all the PhD candidate research activities at Wake Forest Institute for Regenerative Medicine (Winston-Salem, North Carolina, USA) under the supervision of Dr. Sang Jin Lee, Dr. James J. Yoo, Dr. Shay Soker, and Dr. Anthony Atala. We will skip the background information extensively approached in the Introduction Section. This report could only be produced by all the WFIRM team members who provided adequate training, true teamwork, and cooperation: Seunggyu Jeon, Oreoluwa Alonge, Ms. Adit Mehta, Ms. Josua Cheng, Dr. Jun Tae Huh, Dr. Wonwoo Jeong, Dr. Joshua Scott Copus, Dr. Sean Murphy, Dr. Thomas Schupe, Dr. Colin Bishop, Dr. Hyun-Wook Kang, Dr. Sang Jin Lee, Dr. Shay Soker, and Dr. Anthony Atala. Most importantly, the information here remains protected by a non-disclosure agreement between the PhD candidate and WFIRM, remains confidential, and will only be included in this thesis after the approval of the WFIRM supervisors. Otherwise, it will be removed accordingly.

Before the development of the body-on-a-chip approach presented below, a liver-on-a-chip study was currently under development as part of the training period and was published due to his direct contribution (HUH et al., 2024). In parallel, the same chip design was used, but three tissue-derived spheroids are now being incorporated to start the integration of biosensors to test the feasibility of a body-on-a-chip approach.

COVER PAGE

Scientific report

Main Project

BONEInk: Synthesis and characterization of chitosan cross-linked with multi-walled carbon nanotubes and hydroxyapatite nanoparticles decorated with RGD peptides to potential application in 3D-bioprinting technique

(Grant number: 2019/09735-0)

Complete training in additive manufacturing techniques: from the development of a bone bioink for extrusion bioprinting to the integration of microfabricated bioreactors and biosensors

Bolsa Estágio Pesquisa no Exterior (BEPE)

(Grant number: 2021/11291-2)

João Paulo Ruiz Lucio de Lima Parra

Graduate student

Advisors:

Dr. Anthony Atala
Dr. Sang Jin Lee
Dr. Shay Soker
Dr. James J. Yoo

Initial considerations

The grant proposal submitted for the BEPE scholarship funding was suggested by Dr. Anthony Atala in the middle of 2020 when Dr. Willian Zambuzzi started to check about the possibility of performing the Visiting Research Scholar Program at the Wake Forest Institute for Regenerative Medicine (WFIRM). Due to the COVID-19 pandemic travel restrictions, the student's arrival date was postponed to February 2022. Meanwhile, the ongoing study with the biomaterial based on a poly-ϵ-caprolactone (PCL) and β-tricalcium phosphate (β-TCP) to promote osteoconductive/osteoinductive bone scaffolds was finished. With that, finding a new potential biomaterial to achieve the same properties from scratch was necessary. Besides, to learn and become well-trained in all aspects of printing and bioprinting, Dr. Atala also conducted the graduate student to work with three other remarkable researchers at WFIRM, as follows: 1. Dr. Sang Jin Lee, Professor and manager of the Bioprinting core focused on the development of strategies for *in situ* tissue regeneration in terms of mechanism of host cell recruitment, cell sourcing, cellular and molecular roles in cell differentiation, navigational cues, and niche signals, and a tissue-specific intelligent biomaterial system from the perspective of regenerative medicine and tissue engineering; 2. Dr. James J. Yoo, Associate Director and author of over 150 scientific publications, has filed over 30 patent applications. He is also a member of many national and international scientific societies and serves as a consultant to various scientific journals; and 3. Dr. Shay Soker, whose research group has published a manuscript describing, for the first time, the making of functional small human livers from progenitor cells. Using a similar approach, his lab developed small, 3D tissue constructs (organoids) for testing new drugs without testing in animals. In this way, the present scientific report is divided into three main categories that cover all the mentioned background scenarios: i) Training period for bioprinting familiarization and equipment-independent operation; ii) Development of sensor-integrated body-on-a-chip for real-time liver organoid monitoring, and iii) Development of a bone-specific nano clay-dECM composite bioink. The total training period was four months, between February 15th and May 15th, while the starting point of the two other projects was followed after the training ended.

1) The 4-month training period for bioprinting techniques familiarization for equipment-independent operation

In order to become an independent user of all necessary devices/techniques to start the project, it was essential to perform a training period as recommended by all the advisors. They conducted the student in an ongoing body-on-a-chip/biosensors project, encompassing the sought needs regarding studying abroad primary purpose: learning all the aspects of 3D-bioprinting techniques.

Briefly, body-on-a-chip devices are systems developed to recapitulate the micro-environment of the human body physiology using 3D-cell constructs embedded in a bioink within a bioreactor and inserted in a perfusion system (SKARDAL et al., 2017; SUNG et al., 2019). The bioreactor is responsible for the 3D-cell construct's maturation, and it is coupled to a pneumatic pump that flows the cell media from a reservoir to the chip. The summit goals of a body-on-a-chip platform are to speed up the discovery of new drugs, replace animal models, and evaluate specific medications for patients, personalizing the treatment to reduce side effects in chemotherapy, for instance (PICOLLET-D'HAHAN et al., 2021; SKARDAL et al., 2020; WILLIAMSON et al., 2013). Below, Fig.2 depicts all the necessary steps to achieve the body-on-a-chip platform developed in WFIRM:

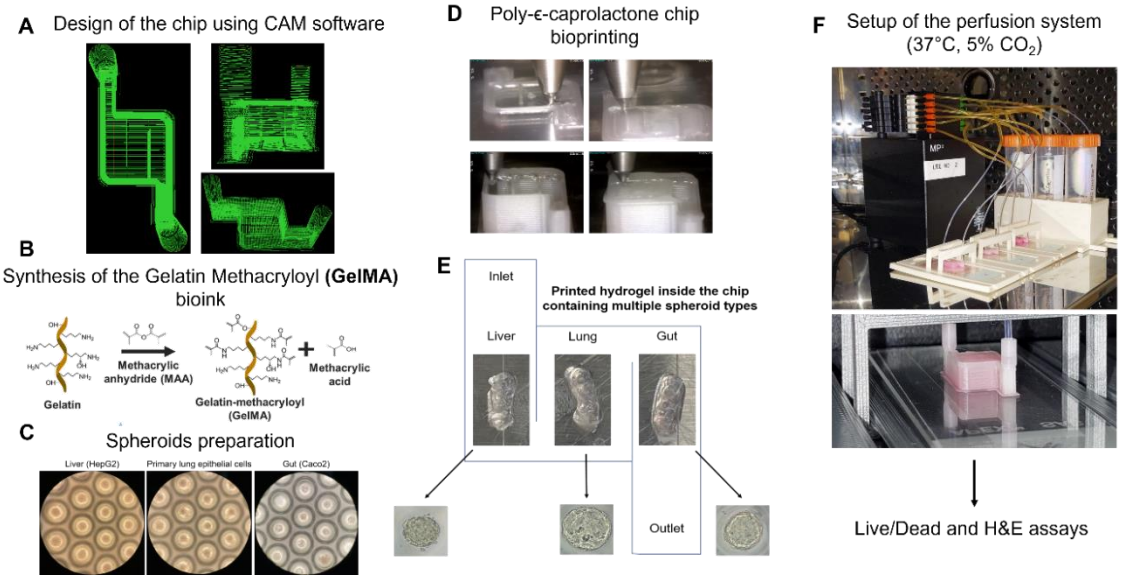

Figure 1: Overview of the applied bioprinting methodology to obtain a body-on-a-chip device to evaluate the system feasibility and cell survival before the tissue/drug interaction study. (A) Design of the layer-by-layer construct (drawn by Jun Tae Huh) deposition using the WFIRM's CAM software followed by the (B) gelatin methacryloyl (GelMA) and (C) multiple 3D cell constructs preparation. After the components are

ready to go, the three spheroids types are embedded in the GelMA bio-ink and placed into multiple printing syringes at 18 °C, aligned, and bio-printed using a 600-diameter nozzle diameter to preserve the cell integrity, as shown by (D) and (E). In (F), the PCL chips containing the multiple spheroid types are set up in a perfusion system in a cell incubator at 37°C and 5% CO_2 atmosphere and were evaluated by Live/Death and H&E assays.

Three main blocks of procedures were performed to obtain the final body-on-a-chip prototype, inserted in a perfusion system, and placed in an incubator at 37°C, 5% CO_2 atmosphere for a 28-day cell viability evaluation.

In the first block, depicted in Fig.1A-C, it was necessary to start with the prototype design using CAM software, synthesize the GelMA bioink, and prepare the three spheroid types. Initially, the CAM software (CODECoding, Fig.1A) was used to concept a liver-on-a-chip design, which was also one of the ongoing projects at WFIRM before the student arrived. The prototype design was leveraged with no adaptations for the body-on-a-chip approach once the difference between an organ-on-a-chip and a body-on-a-chip is only the number of spheroid/organoid types. The approach has an inlet and an outlet with three inner micro-channels to enable the cell media to flow through where the cell-laden bioink is entirely deposited within the micro-channels.

Regarding the GelMA bio-ink synthesis shown in Fig.1B, 10g of gelatin type A 300 bloom from porcine is dissolved in 0.5 M carbonate-bicarbonate buffer at 37 °C (SHIRAHAMA et al., 2016). After the dissolution, a methacrylic anhydride was added to interact with the hydroxyl and amine groups present in the gelatin structure. After 2 hours, Dulbecco's PBS (dPBS) was added to the solution to stop the reaction, and the sample was dialyzed for three days and lyophilized for another five days before use. According to the team optimization process, the desired degree of substitution (amine/hydroxyl for methacrylic groups) was 80% to achieve a correct stiffness after cross-linking the material. The modification of methacrylic acid groups was confirmed by NMR spectroscopy after the GelMA synthesis.

Cells of the liver (HepG2), lung (primary human cells), and gut (Caco2) were cultured using an Organoid Formation Media (OFM: DMEM-HG cell media + 10% FBS + 10 µg/mL of rat tail collagen + 1 µg/mL + 10 µg/mL of gentamycin) to build the spheroids. The cell density for the three types was $7x10^6$ million for every 3 wells of a 6-well plate. To give the 3D form of the spheroid structures, a Corning® 600/500 bottom round black with clear bottom ultra-low attachment was used after mixing the cells with

the OFM, shown in Fig.1C. They were maturated for four days in an incubator at 37°C, 5% CO_2 atmosphere and gently resuspended from the 6-well plate before incorporating the GelMA bio-ink. After the spheroids maturation period, 10% (v/v) of glycerol was dissolved in a phenol red-free DMEM-HG cell media solution and mixed with 0.3% (w/v) of hyaluronic acid, 3.5% (w/v) of GelMA, 3% (w/v) of gelatin type A 300g bloom, and 0.2% (w/v) of Lithium phenyl-2,4,6-trimethylbenzoylphosphinate (LAP) photoinitiator in a warm-shaker at 45°C for 30 minutes. While the bioink solution remained warm, the liver, lung, and gut spheroids were gently mixed with the bioink and rapidly cooled down in an ice bath so the thermo-sensitive property of GelMA can avoid spheroids precipitation and maintain them well-distributed. Next, the bio-ink was ready to be printed within the chip and cross-linked, and it was maintained colled over the whole printing, which will be explained in the second block of procedures.

Secondly, it is depicted in Fig.1D, E that the stacked chip prototype was printed layer-by-layer using the Integrated Tissue/Organ Printer (ITOP). The ITOP system is a micro extrusion device built *in situ* at WFIRM, containing an XYZ-stage and multi-cartridges with micro-nozzles inside a closed chamber (KANG et al., 2016). One of the cartridges has a metal syringe involved by a heating jacket responsible for printing thermo-sensitive polymers such as poly-ε-caprolactone (PCL), and another has a cooling jacket to control the gelation of the bio-inks. In this approach, we used a melted PCL (40000 – 50000K) to build the chip, which was heated at around 80°C, allowing the extrusion process. For the bio-ink printing, the syringe was inserted in the cooling jacket at 18°C, maintaining the desired gelation properties during the deposition within the chip. After the spheroids printing, the bioink was cross-linked by UV light with an intensity of 200 mW/cm^2 for 10 seconds, where the outcome scheme is shown in Fig.2E. Then, the PCL coverage continued to the inlet and outlet formation, closing the chip and finishing the printing process around 30 minutes. The PCL and bio-ink syringes nozzle sizes were carefully selected to print PCL with high resolution and avoid spheroids damage, 300 µm and 610 µm, respectively.

Finally, the third block of procedures was setting the printed chips in a perfusion system and the 28-day cell viability evaluation of the liver, lung, and gut spheroids through the Live/Dead and H&E assays, depicted in Fig.1F. The chips were connected with a peristaltic pump (ESI® MP-2 set with 2 RPM, 10 µL/min) inside an incubator at 37 °C 5% CO_2 atmosphere. Afterward, for the Live/Dead assay, the cross-linked bioinks

were removed from the chips and conducted to a phenol red-free DMEM-HG cell media containing calcein-AM and ethidium heterodimer-1 fluorescent dyes. Samples reacted for 30 minutes before obtaining the confocal images and performing the cell counting. For the H&E assay, the samples were fixed with 4 % paraformaldehyde (v/v) before the execution of the staining protocol. Both data are presented below in Fig.2:

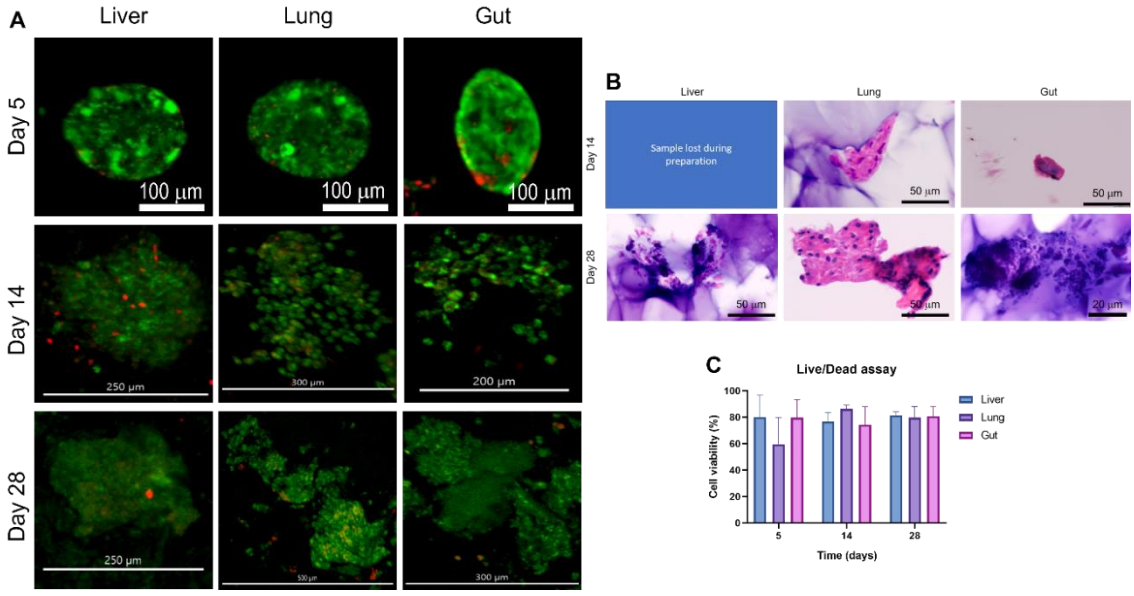

Figure 2: (A) Live (green) / Dead (red) assay performed using an OLYMPUS confocal microscope using the calcein-AM and ethidium-homodimer stains. The spheroids (liver, lung, and gut) were kept embedded in the GelMA bioink and maturated in phenol-red free DMEM high glucose cell media for 30 minutes in a cell incubator at 37°C 5% CO_2 atmosphere before the analysis. In (B) and (C), it is depicted the Hematoxylin/Eosin (H&E) stain assay for the extracellular matrix, cytoplasm, and nuclei evaluation of the three spheroids types and the output of Live/Dead assay cell counting, respectively.

Fig.2A shows the confocal images of the stained liver, lung, and gut spheroids over 28 days of cell viability evaluation. The increase in the spheroids' size over time can be noticed, which indicates that the bio-ink formulation works appropriately and allows cell spreading and proliferation. In this stage, the goal was to check the chip design feasibility before testing any drug exposure and its relation with the specific biomarkers secretion by each spheroid type. Fig.2B shows the H&E assay images of day 14 and day 28, which also depict the increase of the spheroids over time and corroborate with the Live/Dead assay data and the cell counting in Fig.2C, all presenting good cell viability of around 80% during the whole 28-day evaluation period. Thus, it is indicative that our platform is feasible to maturate multiple spheroid types and can be tested under drug exposure.

However, we faced some limitations during both experiments' sample processing and data collection. Despite the detected cell proliferation in the three spheroid types seen in the confocal images, their 3D-round shape was lost over time, which is undesirable. Spheroids must grow equally and at the same pace to compare drug-challenged and control groups. We believe this issue occurred because the spheroids were not well-mixed and did not have good distribution within the bioink, allowing spheroid agglomeration. This issue was also confirmed in the H&E images, highlighted by the merged nuclei and cellular matrix at the lung spheroid on day 28. Also, liver spheroids on day 14 were lost due to technical issues. Besides, concerning layer-by-layer PCL chip fabrication, a few leaks were detected occasionally batch-to-batch, probably due to a not well-stacked chip portion that might cause micro-defects.

One of the state-of-the-art aims in the body-on-a-chip research field is real-time monitoring and automatized perfusion system and data collection during the experiment. Usually, the experiments are performed by collecting the cell media daily for biomarker secretion, followed by the ELISA assays for quantification. This step was also the last goal to achieve in the training period, but the biomarker data presented significant fluctuations. To overcome these challenges, the student contributed to the body-on-a-chip project at WFIRM, sharing his experience with biosensors and developing the integration of DNA probes for real-time monitoring. Silver electrodes were used to immobilize the biosensors and inserted into the perfusion system to monitor the released biomarkers concentration using electrochemistry workstations. In this way, the advisors opted to integrate them, adapt the approach to overcome the leaking problem, and optimize several other chip design parameters, which will be explained in the next section.

2) Development of sensor-integrated body-on-a-chip for real-time organoid monitoring

As mentioned in the previous section, we opted to improve the system by fixing recurrent issues and improving the system features. For instance, a pilot study (data not shown) based on monitoring the secreted biomarkers using just the liver spheroids through ELISA kits was revealed to be a more costly and hard-to-handle method of the necessity of daily cell medium change and collection (100 microcentrifuges vials and 15 conical tubes per day). Also, even though the cell viability data showed healthy spheroids, the ELISA assays detected a considerable fluctuation in the secreted biomarkers concentrations.

Besides, the biomarker pilot study using ELISA kits was not performed in real-time but after the experiment.

Considering the lack of information about the environment (cell media pH, temperature, conductivity, hypoxia, etc.) and the monitorization of biological features, we integrated commercial sensors and biosensors for the complete real-time monitoring of liver spheroids. In case of success, the team will expand the capability of our platform to other spheroids types to monitor the biomarkers for each one using multiple organoid-specific biosensor stations, providing precise information on 3D-cell constructs using a microfluidic approach. This step is necessary before starting the drug-tissue interaction in pharmacy-kinetic studies, as we were doing with the PCL chip in the first place.

Three main necessary steps to improve and optimize our approach were required: **(i)** pre-fabricate the bioreactor, sensor housing, and media reservoir to hold the biosensors using DLP printing instead of micro-extruded PCL to avoid the cell media leaking problems with layer-by-layer stacking; **(ii)** production of silver electrodes using inkjet printing followed by the aptamer immobilization onto the surface; and **(iii)** assemble the pre-fabricated components in the perfusion system using micro-pumps, and evaluation of the biosensor immobilization using electrochemistry workstation.

2.1) Pre-fabrication of the bioreactor, sensor housing, and media reservoir by DLP printing

As mentioned, we pre-fabricated the body-on-a-chip components using DLP printing to improve our approach and avoid the leaking problems presented in the PCL-based chip. Below, Fig.3 shows the CAD designs of the bioreactor (Fig.3A), sensor housing (Fig.3B), and media reservoir (Fig.3C). All of them were drawn using both SolidWorks and Fusion 360 software. Designs were manufactured using DLP FormLabs Form 3+ printer and FormLabs BioMed Clear biocompatible resin. The bioreactor design was entirely adapted from the PCL version, and it was only necessary to keep the three channels open for bio-ink printing. After this, the chip was covered with PCL and passed the leaking-proof test successfully, as Fig.3D shows.

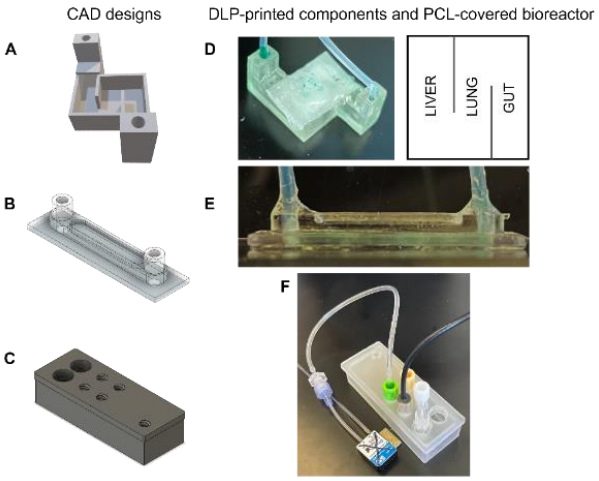

Figure 3: Overview of the used design and the applied DLP printing technique to obtain pre-fabricated body-on-a-chip components for the leaking-proof test before setting the perfusion system in the incubator and challenging our approach in a specific spheroid/drug interaction study. In (A), (B), and (C), the CAD designs of the bioreactor, sensor housing, and media reservoir are shown, respectively (A: drawn by Joshua S. Copus; B and C: Joshua Cheng). In (D), (E), and (F), the high-resolution DLP printing outcomes are depicted.

The sensor housing design was conceived with the following considerations: the shape and coverage of the silver layer printed in the glass slide, injection cell media in the chamber, and flow speed to allow detection through the immobilized aptamers. It is worth mentioning that the aptamers must be immobilized on the silver electrode, and then the pre-fabricated sensor housing is fixed with UV glue. Fig.3E shows the fixed sensor housing on a glass slide under the leaking test using a pneumatic pump at 2 RPM (10 µL/min), considering the ideal speed to obtain a dynamic system and allowing the biomarker detection; no issues occurred. Also, the design shape was printed slightly oval to avoid any disturbance in the flow.

The media reservoir, depicted in Fig.3F, was designed with a 15 mL total volume to have enough media for a day without exchanges. This amount of volume was calculated based on the previous PCL's chip approach, which is enough to keep the ideal spheroids' maturation. Besides, the reservoir lid was designed to have universal connectors to plug the commercial sensors (glucose-lactate, pH, temperature, conductivity, hypoxia) to monitor the cell media quality in real time. This device feature can prevent the lack of ideal spheroid nutrition. In parallel, the team worked on producing silver electrodes using

inkjet printing and an aptamer immobilization protocol before the sensor housing fixation and the perfusion system assembly.

2.2) Production of silver electrodes using inkjet printing followed aptamer immobilization onto the surface

Initially, we needed to develop a printability protocol for the inkjet printer to identify the printing resolution limit once the printer was out of operation for a few years. With the remote help of the former researcher at WFIRM, Dr. Ashkan Shafiee, and the MicroFab company, we learned that the correct way to design any desired pattern is through a bitmap extension file. Bitmap files are black-and-white pictures recognizable by the printer, and the white portion is printed. Thus, the printability protocol was designed using Microsoft Paint software based on squares, circles, and non-straight angle shapes followed by the printed pattern, as shown in Fig.4A. An adhesion test was also designed to evaluate the interaction of the silver ink with the substrate (glass slide). Fig.4B shows the quantification analysis to determine the deviations between the design and the printed outcome. The inkjet printer JetLab 4 has a specific camera to check the printed layer morphology. Also, the camera movement is controlled with a micrometer precision, which allows us to quantify the pattern sizes by measuring the distance between the edges. As expected, smaller sizes had higher errors, meaning the determined cutoff point in printer resolution was above 1 mm.

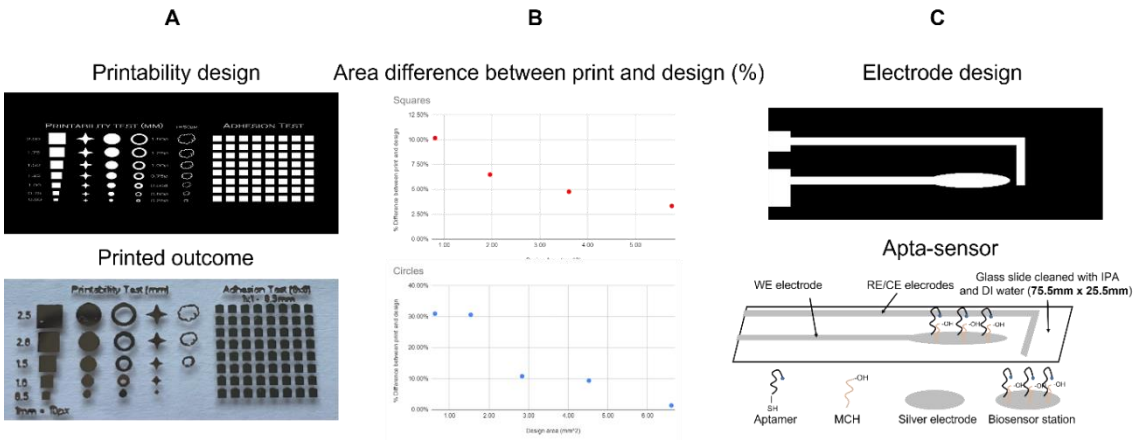

Figure 4: In (A), the developed printability design for MicroFab© JetLab 4 inkjet printer to check the printer resolution limitation and the printing outcome are depicted. As presented in (B), significant deviations were detected as long as the shape decreased. Finally, in (C), the oval-shaped design considering the flow pathway of the silver electrode and the aptamer-based biosensor preparation scheme is shown.

Several steps are necessary to prepare before starting the printing process. First, the surface must be well-cleaned to improve the ink droplet adhesion due to the necessity

to control the substrate's hydrophilic properties (SHAFIEE et al., 2019). We established a simple cleaning protocol by washing the glass slide using pure isopropyl alcohol (IPA) and deionized water (DI) for 10 seconds each step. Second, controlling droplet formation is essential to obtain the desired resolution. As previously mentioned, the formation of one ink droplet is mainly controlled by time to determine the piezoelectric crystal vibration precisely, and it is divided into five secondary intervals: rise 1, dwell, fall, rise 2, and echo, in a millisecond order. Another critical parameter to control the ink droplet formation is the applied voltage, which is responsible for the angle and speed at which the droplet will form and hit the stage where the substrate is placed. About the stage, it was warmed at 70 °C before printing to avoid ink blur during its movement. Afterward, the electrode pattern, represented in Fig.4C, can be printed and conducted in a sintering furnace to evaporate the ink solvent and attach the silver layer to the glass slide substrate. The electrode design was conceived to have the same oval shape as the sensor housing, having two separate lines with a three-electrode system attached to an electrochemical workstation: the working electrode that will receive the liver-specific biosensor station and reference and counter electrodes will allow the signal formation subtracting media background and close the circuit. Section 2.3 briefly describes the aptamer's detection mechanism and data collection, such as the step-by-step immobilization process.

After printing the electrodes, they were sintered at different temperatures for 30 minutes and evaluated by scanning electron microscopy (SEM) for morphology analysis to check the adhesion and grain formation, as shown below in Fig.5:

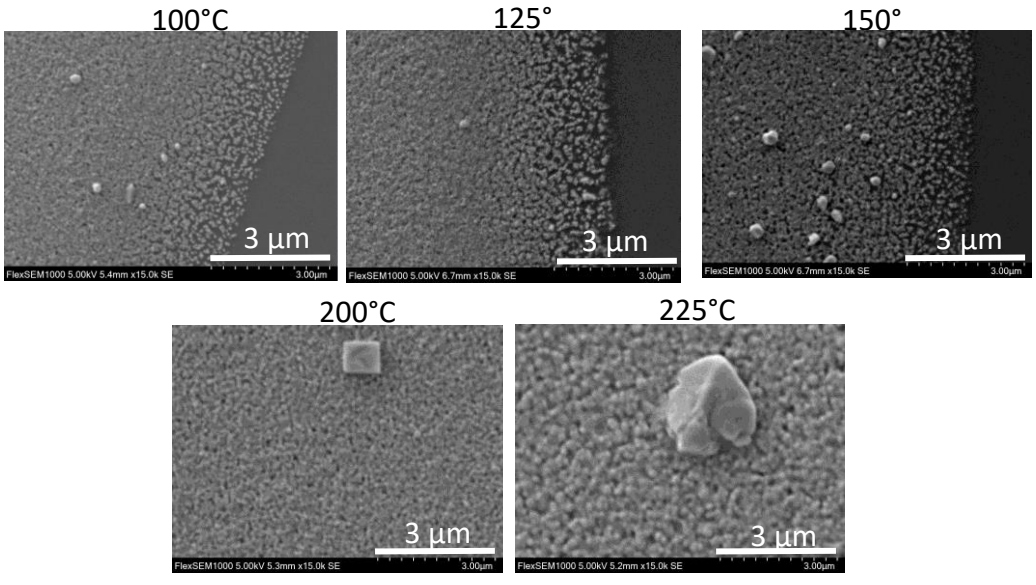

Figure 5: Different sintering times of the electrode silver layer are represented. The silver grain formation follows the same trend once the baking temperature increases. Samples were cured in a furnace and analyzed by scanning electron microscopy (SEM) at the same magnification (15.000x) using a Hitachi SU1000 SEM flex 490-1 model after a 5-nm thickness gold layer deposition.

As expected, as the temperature increased, the silver nanoparticle ink (30% - 40% v/v, Sigma-Aldrich) merged during the sintering process, which resulted in a grain size as well. Thus, we opted to use the 225°C sintering temperature to produce our electrodes for two main reasons: as the grain size is large enough in this condition, this can increase surface roughness, which is desirable to improve the aptamer immobilization. Also, the silver layer proved well-attached to the glass slide after checking in the adhesion test, performed using a 3M double-sided tape. Besides, the produced electrodes were submersed into the cell media for 72 hours, and silver only came out if the scratch was severe. However, the silver electrodes should be handled carefully to avoid creating micro defects or unwanted scratches, especially when set in wet conditions (perfusion system) and if the aptamers are already immobilized onto it. Next, the assembly of the perfusion system and the data acquisition will be presented.

2.3) Aptamer biosensor preparation and the assembly of the pre-fabricated components in the perfusion system

The aptamer immobilization process is the last part of the procedure before assembling all the components into the automated perfusion system. Briefly, aptamers are DNA/RNA probes produced by systematic evolution ligands by exponential enrichment (SELEX), which uses a random DNA library to expose it to a desired target and selects sequences that interact only with the respective analyte (OHUCHI, 2012; WANG et al., 2014). Chemical modifications in the aptamers structures were necessary to transform them into a biosensor: thiol group fixed in 5’ and a methylene blue red/rox probe in the 3’ edges. Once the goal is to check the feasibility of our approach using liver spheroids first to expand it to the other after, high-specific aptamers were purchased (Base Pair Biotechnology, nt = 39) for human serum albumin detection, biomarker secreted by the 3D-shaped HepG2 cells. Fig.7 shows how the detection mechanism of the HSA-specific aptamer and signal collecting works:

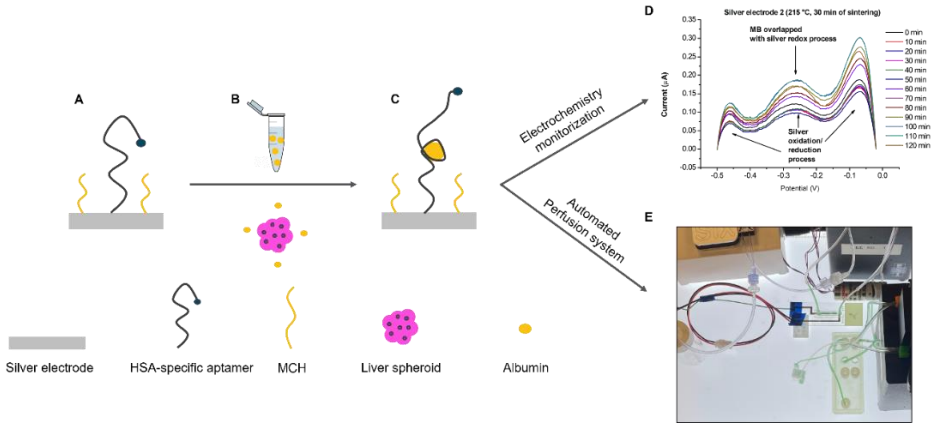

Figure 6: (A) Live (green) / Dead (red) assay performed using a HITACHI confocal microscope using the calcein-AM and ethidium-homodimer stains. The spheroids (liver, lung, and gut) were kept embedded in the GelMA bioink and maturated in phenol-red free DMEM high glucose cell media for 30 minutes in a cell incubator at 37°C 5% CO_2 atmosphere before the analysis. In (B) and (C), it is depicted the Hematoxylin/Eosin (H&E) stain assay for the extracellular matrix, cytoplasm, and nuclei evaluation of the three spheroids types and the output of Live/Dead assay cell counting, respectively.

After printing and sintering the silver electrodes, the final concentration of 1 µM of HSA-specific aptamer solution was prepared from a stock solution with a folding buffer. Next, the solution was heated at 95 °C for 5 minutes, cooled to room temperature, and mixed at a 1:1 (v/v) ratio with a 10 mM TCEP-reducing buffer (BondBreaker®, Thermo Fischer) for 10 minutes to break the formed disulfide bonds among the aptamers to improve its immobilization. Afterward, aptamers were remixed with the folding buffer + 1 mM of $MgCl_2$ and immobilized onto the silver-based working electrode for 16 hours. In sequence, the silver electrode was rinsed with PBS to remove the unbonded aptamer, and 3 mM of self-assembled monolayer (6-mercapto-hexanol, MCH, Sigma-Aldrich) was added to organize the aptamers, as presented in Fig.6A. Finally, the apta-sensor is ready to be tested, and it was attached to the 3-electrode connectors of the electrochemical workstation for the real-time biomarker monitoring.

The last performed experiment related to this project was the HSA biomarker detection and assembling of the perfusion system. HSA protein (Sigma-Aldrich) was diluted in PBS in different concentrations (1 ng/mL – 100 ng/mL) and monitored over 2 hours, shown in Fig.6B. Fig.6C and 6D represent how the signal is produced: HSA protein has a high affinity by the DNA conformation, and due to a strong interaction, moves the methylene blue redox probe away from the electrode layer. Then, the signal decreases when the potentiostat applies the voltage to measure the currents because the electron

transfer between the labeled aptamer probe and the silver layer is difficult (INAM et al., 2022; ZHANG et al., 2007). However, the generated data presented interferent signals in -0.07V and -0.45V regions due to the oxidation and reduction process from the silver layer near the excitation potential of the methylene blue probe, around -0.25V. The ideal experimental condition should not have interferent signals overlapping the methylene blue peak (PARRA et al., 2018), so the albumin quantification was considered unreliable. Such results demonstrated the necessity to change the silver metallic ink to gold to overcome this issue once gold is considered more inert to silver's oxidation and reduction events (ABREGO-MARTINEZ et al., 2022; LEE; JANG, 2020; OBERHAUS; FRENSE; BECKMANN, 2020; TOH et al., 2014). The main reason for using silver ink in the first place was the availability of WFIRM's reagent stock and the low costs compared to gold. At least, we could check the changes in the current intensity, which indicates that the apta-sensor approach works to monitor human serum albumin. Even though we faced this issue, the leaking-proof test and the automated media injection in the perfusion system were successful after the assembly, as depicted in Fig.6E.

Due to the ending of the 1-year visiting research scholar program, it was not possible to participate in the next steps of this project, but the team will perform: (i) the change of the silver metallic ink for gold; (ii) repeat the albumin quantification to obtain a calibration curve to correlate the current intensity with the albumin concentration over time; (iii) set the perfusion system with the liver spheroid within the bioreactor and monitor the secreted biomarkers concentration in real-time using the sensor housing and automated measurements; (iv) after validating with liver spheroids with and without drug exposure, and expand the spheroid types as well as the biosensor stations to study the complete pharmaco-kinetics profile monitoring multiple spheroid types in parallel and real-time. Section 3 will describe all the progress made regarding developing a bone bioink project based on Laponite-RD and GelMA.

3) Development of a bone-specific nano clay-GelMA composite bioink

As mentioned in the initial considerations, finding and developing a new bioink synthesis from scratch was challenging due to the postponement of the student's arrival due to the COVID-19 pandemic scenario. During the training, the student and Dr. Lee discussed several potential materials for developing a novel bioink approach, which was decided

by a methacrylate-decellularized bone extracellular matrix (bone dECM-MA) - Laponite nano clay formulation. The strategy behind this choice was based on the interesting properties of both compounds regarding stem cell differentiation: bone dECM-MA and Laponite are reported in the literature as osteoinductive materials enabling cell differentiation after metabolization (AMIRAZAD; DADASHPOUR; ZARGHAMI, 2022b; JIN et al., 2017).

Bone dECM has critical organic compounds such as proteoglycans, cytokines, RGD motifs, and other biochemical cues that precisely recapitulate the ideal cell microenvironment (AMIRAZAD; DADASHPOUR; ZARGHAMI, 2022a). Laponite-RD can organize itself after hydration with a “house-of-cards” structure that can improve the embedding of the mentioned dECM biomolecules in the bioink. Also, bone cells can degrade Laponite-RD nanodisks into orthosilicic acid byproducts, one of the responsible for inducing bone cell differentiation (TOMÁS; ALVES; RODRIGUES, 2018; ZANDI et al., 2021). These properties gathered in a bioink formulation were considered powerful to be tested as a cell-laden biomaterial. However, the methacrylation process of the bone dECM has not yet been optimized in Dr. Lee’s research group due to the very complex structure of bone dECM, which is difficult to digest and modify appropriately. While another teammate determined the methacrylate optimization conditions, we started the bioink formulation synthesized with GelMA. Its structure and mechanical properties are similar to the bone dECM despite lacking essential biomolecules (ADIB et al., 2020a; DONG et al., 2021). Thus, the bioink formulation containing GelMA was synthesized and considered our positive control group for future comparison and replacement by bone dECM-MA, despite the lack of the essential biochemical cues features.

The GelMA-Laponite bioink synthesis was performed as Figure 7 shows:

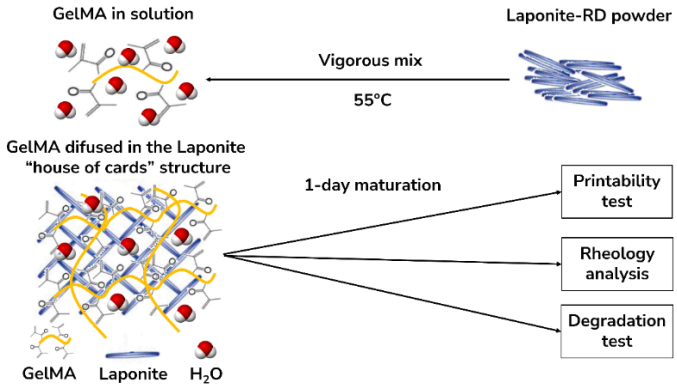

Figure 7: Laponite/GelMA bioink synthesis scheme and the characterization techniques.

GelMA and LAP photoinitiator (0.2%, w/v) was diluted using DI water at different concentrations (0.5% to 2%, w/v) in a warm shaker at 55 °C for 1 hour. After obtaining a clear solution, a GelMA solution was stirred for 2 hours in a pre-heated and covered becker with aluminum foil at 37 °C to prevent GelMA coagulation and unwanted cross-linking sites. Then, Laponite powder (4% to 6%) was slowly incorporated into the GelMA solution to well-distribute the nano clays and well-form the "house-of-cards" structure. However, the synthesis was very sensitive and challenging to be established and optimized. The "house-of-cards" structure is formed through negative and positive charge interactions presented on the Laponite disk face and edges after its hydration, respectively. The speed rotation must be as fast as possible to avoid structure formation, but due to the high concentrations of Laponite, it can jeopardize GelMA diffusion. Clogs in the printing syringes and inconstant flow rate were often recurrent until the optimized synthesis protocol was achieved. Then, we needed to reduce the Laponite amount and increase the GelMA in the bioink formulation.

After the synthesis, the bioink formulations were maturated at room temperature, protected from light for at least 1 day before use (AU et al., 2015), and conducted to the printability, rheology, and degradation analysis. Below, Fig.8A and 8B show the design and printed outcomes of the printability test:

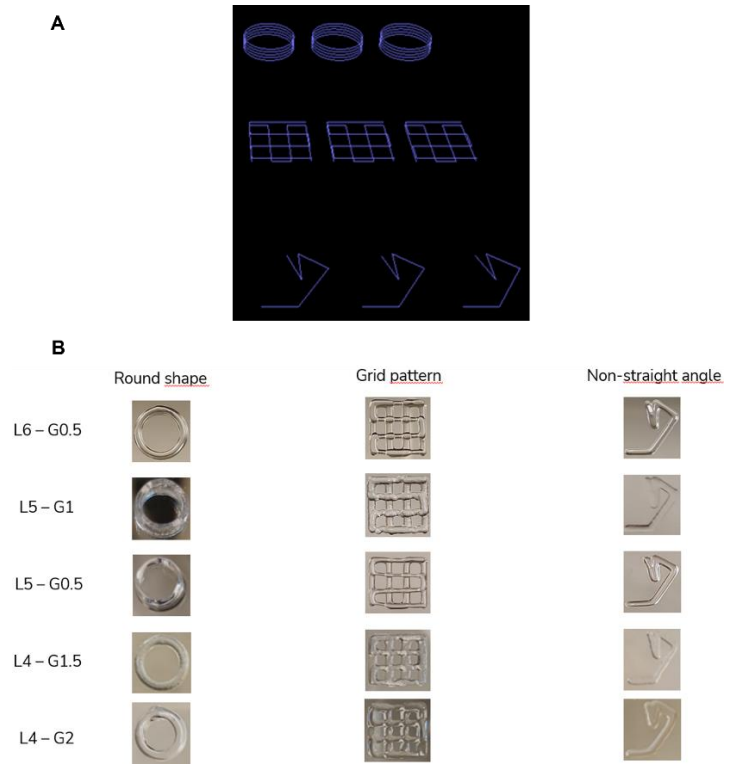

Figure 8: (A) The design of Dr. Lee's group printability protocol (Drawn by Gregory Gillespie using the CODECoding CAM program). In (B), the printed outcome of different bioink formulations. Samples were printed using the ITOP printer, 330 µm nozzle size, and a cooling jacket for gelation control at 25 °C and 18 °C for lower and higher GelMA concentrations, respectively. A humidifier was used to maintain the samples hydrated. LX%(w/v) - GY% (w/v) = L6-G0.5, L5-G1, L5-G0.5, L4-G1.5, and L4-G2, where LX = Laponite concentration and GX = GelMA concentration.

All these printable bio-ink formulations were selected based on the well-achieved resolution and labeled as LX%(w/v) - GY% (w/v) = L6-G0.5, L5-G1, L5-G0.5, L4-G1.5, and L4-G2, and carried to the degradation using DMEM – high glucose cell media for 28 days as shown by Fig. 9A:

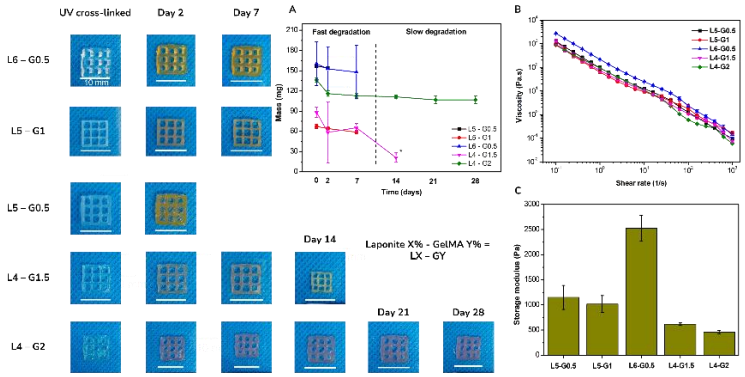

Figure 9: (A) Degradation test using non-tissue Petri dishes containing DMEM-HG cell media evaluated for 28 days in an incubator at 37 °C 5% CO_2 atmosphere and mass loss quantification over time. The mass

of the samples was recorded right after printing and on days 2, 7, 14, 21, and 28. Before the measurements, samples were dried with a paper wipe until no more water came out. In (B) and (C), the viscosity and storage modulus were collected after cross-linking the samples using a Discovery HR-2 rheometer with a 40 mm 1° angled circular plate at the same printing temperature, depending on each bioink formulation.

The contribution of the cross-linking effect provided by a higher GelMA amount in the bioink formulation is evidenced in the degradation analysis. GelMA maintains Laponite's "house-of-cards" structure, slowing bio-ink degradation considerably, which was our primary goal in this project. Also, we investigated the rheology properties of the cross-linked bioinks, such as viscosity and storage modulus, depicted in Fig. 10B and 10C. The viscosity shows a shear-thinning behavior of all investigated formulations, which means the ability to lose the structure during the material compression and recover the original format before the extrusion (ADIB et al., 2020b), also demonstrated by printability analysis. Besides, once the Laponite was considerably higher than GelMA, a higher storage modulus was expected in those bioink formulations. However, the cross-linking was not significant enough to affect the bio-inks storage modulus.

Unfortunately, due to the 1-year visiting research scholar program's ending, it was not possible to incorporate steam cells and study their viability, proliferation, and differentiation. Also, the team did not achieve a well-optimized methacrylate protocol for bone dECM, which was revealed to be very complex and challenging to handle. The following steps of this project will be: (i) synthesize and characterize one more bioink formulation, L4-G2.5, trying to improve the slower degradation property of the bioink even more; (ii) incorporate within the bioink pre-osteoblast and stem cells and check the differentiation rate and osteoinductive feature of our bone bioink; (iii) molecular biology and histology studies for a well-mapping of gene expression and tissue organization, respectively; and (iv) *in vivo* studies in craniofacial/bony lesions of rats for our bioink validation.

4) Conclusion

3D-bioprinting is a multi-disciplinary and vast field with a broad spectrum of techniques emerging to improve regeneration and assist new strategies for patient recovery. All advisors' outstanding mentorship allowed the student to learn all aspects of 3D-bioprinting to apply in his ongoing project in Brazil. Extrusion, inkjet, and vat

photopolymerization techniques were successfully explored by working on two relevant projects: contributing to integrating a real-time monitoring system based on biosensors into body-on-a-chip devices and the development of a novel bone bioink using bone GelMA and Laponite nano clays to a further substitution to bone dECM-MA. Despite all the challenges, the advisors considered the general research progress pace relevant for a 1-year program, as demonstrated by the four advisor's performance statements attached to this scientific report. Besides, a strong collaboration between Dr. Zambuzzi's lab and all the advisors was established and will be maintained thanks to this opportunity granted by FAPESP. At WFIRM, the student also could train and mentor other students in biosensor development as a mutual exchange for the 3D-bioprinting training provided by all the advisors. Now, the student will transfer and share the acquired abilities with Dr. Zambuzzi's lab mates through multiple training sessions and apply them in his ongoing project in Brazil, also supported by FAPESP, expanding the capability of Dr. Zambuzzi's research group to apply additive manufacturing and explore new intelligent biomaterials suitable to be applied in 3D-Bioprinting.

7. REFERENCES

ABREGO-MARTINEZ, J. C. et al. Aptamer-based electrochemical biosensor for rapid detection of SARS-CoV-2: Nanoscale electrode-aptamer-SARS-CoV-2 imaging by photo-induced force microscopy. **Biosensors and Bioelectronics**, v. 195, 1 jan. 2022.

ADIB, A. A. et al. Direct-write 3D printing and characterization of a GelMA-based biomaterial for intracorporeal tissue. **Biofabrication**, v. 12, n. 4, 2020a.

AMANI, J. et al. Cyclin-dependent kinase inhibitors (CDKIs) and the DNA damage response: The link between signaling pathways and cancer. **DNA Repair**, v. 102, n. March, p. 103103, 2021.

AMARASEKARA, D. S.; KIM, S.; RHO, J. Regulation of osteoblast differentiation by cytokine networks. **International Journal of Molecular Sciences**, v. 22, n. 6, p. 1–16, 2021.

AMIRAZAD, H.; DADASHPOUR, M.; ZARGHAMI, N. Application of decellularized bone matrix as a bioscaffold in bone tissue engineering. **Journal of Biological Engineering**, v. 16, n. 1, p. 1–18, 2022a.

AMIRAZAD, H.; DADASHPOUR, M.; ZARGHAMI, N. **Application of decellularized bone matrix as a bioscaffold in bone tissue engineering**. **Journal of Biological Engineering**BioMed Central Ltd, , 1 dez. 2022b.

ASGHAR, U. S. et al. Systematic Review of Molecular Biomarkers Predictive of Resistance to CDK4/6 Inhibition in Metastatic Breast Cancer. **JCO Precision Oncology**, n. 6, p. 1–13, 2022.

ASHAMMAKHI, N. et al. Advancing Frontiers in Bone Bioprinting. **Advanced Healthcare Materials**, v. 8, n. 7, p. 1–24, 2019.

AU, P. I. et al. Behaviour of laponite gels: Rheology, ageing, pH effect and phase state in the presence of dispersant. **Chemical Engineering Research and Design**, v. 101, p. 65–73, 2015.

BARTHELEMI, S. et al. Mechanical forces-induced human osteoblasts differentiation involves MMP-2/♪MMP-13/MT1-MMP Proteolytic Cascade. **Journal of Cellular Biochemistry**, v. 113, n. 3, p. 760–772, 2012.

BERGERON, E. et al. Differentiation of preosteoblasts using a delivery system with BMPs and bioactive glass microspheres. **Journal of Materials Science: Materials in Medicine**, v. 18, n. 2, p. 255–263, 2007.

BRANCA, C. et al. Role of the OH and NH vibrational groups in polysaccharide-nanocomposite interactions: A FTIR-ATR study on chitosan and chitosan/clay films. **Polymer**, v. 99, p. 614–622, 2016.

CARREIRA, A. C. et al. Bone Morphogenetic Proteins: Structure, biological function

and therapeutic applications. **Archives of Biochemistry and Biophysics**, v. 561, p. 64–73, 2014.

CARROW, J. K.; GAHARWAR, A. K. Bioinspired polymeric nanocomposites for regenerative medicine. **Macromolecular Chemistry and Physics**, v. 216, n. 3, p. 248–264, 1 fev. 2015.

CARSON, L. et al. Synthesis and characterization of chitosan-carbon nanotube composites. **Materials Letters**, v. 63, n. 6–7, p. 617–620, 2009.

CÉLIO, C. J. et al. Epigenetic Differences Arise in Endothelial Cells Responding to Cobalt–Chromium. **Journal of Functional Biomaterials**, v. 14, n. 3, 2023.

CHATTERJEE, S.; LEE, M. W.; WOOA, S. H. Adsorption of congo red by chitosan hydrogel beads impregnated with carbon nanotubes. **Bioresource Technology**, v. 101, n. 6, p. 1800–1806, 2010.

CHAVEZ, M. B. et al. Bone Sialoprotein Is Critical for Alveolar Bone Healing in Mice. **Journal of Dental Research**, v. 102, n. 2, p. 187–196, 2023.

CHEN, L. et al. Synthesis and characterization of chitosan-multiwalled carbon nanotubes/hydroxyapatite nanocomposites for bone tissue engineering. **Journal of Materials Science: Materials in Medicine**, v. 24, n. 8, p. 1843–1851, 2013.

CHEN, W. et al. Bone regeneration using mmp-cleavable peptides-based hydrogels. **Gels**, v. 7, n. 4, 2021.

CHEW, K. K. et al. Reinforcement of calcium phosphate cement with multi-walled carbon nanotubes and bovine serum albumin for injectable bone substitute applications. **Journal of the Mechanical Behavior of Biomedical Materials**, v. 4, n. 3, p. 331–339, 2011.

CHRANIUK, M. et al. The Preliminary Assessment of New Biomaterials Necessitates a Comparison of Direct and Indirect Cytotoxicity Methodological Approaches. **Polymers**, v. 14, n. 21, 2022.

DAI, B. et al. Schiff base-chitosan grafted multiwal led carbon nanotubes as a novel solid-phase extraction adsorbent for determination of heavy metal by ICP-MS. **Journal of Hazardous Materials**, v. 219–220, p. 103–110, 2012.

DAI, C. et al. Three-Dimensional High-Porosity Chitosan/Honeycomb Porous Carbon/Hydroxyapatite Scaffold with Enhanced Osteoinductivity for Bone Regeneration. **ACS Biomaterials Science and Engineering**, v. 6, n. 1, p. 575–586, 2020a.

DAI, C. et al. Three-Dimensional High-Porosity Chitosan/Honeycomb Porous Carbon/Hydroxyapatite Scaffold with Enhanced Osteoinductivity for Bone Regeneration. **ACS Biomaterials Science and Engineering**, v. 6, n. 1, p. 575–586, 13 jan. 2020b.

DE ALMEIDA, G. S. et al. Development of cobalt Co-doped monetites for bone regeneration. **Journal of Biomedical Materials Research**, v. 112, n. 1, p. e35319, 2024.

DEHNAVI, E. et al. The effect of TGF-β 2 on MMP-2 production and activity in highly metastatic human bladder carcinoma cell line 5637. **Cancer Investigation**, v. 27, n. 5, p. 568–574, 2009.

DEMIRTAŞ, T. T.; IRMAK, G.; GÜMÜŞDERELIOĞLU, M. A bioprintable form of chitosan hydrogel for bone tissue engineering. **Biofabrication**, v. 9, n. 3, 13 jul. 2017.

DEPALLE, B. et al. Osteopontin regulates type I collagen fibril formation in bone tissue. **Acta Biomaterialia**, v. 120, p. 194–202, 2021.

DHIMAN, H. K.; RAY, A. R.; PANDA, A. K. Characterization and evaluation of chitosan matrix for in vitro growth of MCF-7 breast cancer cell lines. **Biomaterials**, 2004.

DONG, L. et al. Facile extrusion 3D printing of gelatine methacrylate/Laponite nanocomposite hydrogel with high concentration nanoclay for bone tissue regeneration. **International Journal of Biological Macromolecules**, v. 188, p. 72–81, 1 out. 2021.

DU, J. et al. Understanding the toxicity of carbon nanotubes in the environment is crucial to the control of nanomaterials in producing and processing and the assessment of health risk for human: A review. **Environmental Toxicology and Pharmacology**, v. 36, n. 2, p. 451–462, 2013.

ELDRED, J. A. et al. MMP2 activity is critical for TGFβ2-induced matrix contraction-implications for fibrosis. **Investigative Ophthalmology and Visual Science**, v. 53, n. 7, p. 4085–4098, 2012.

FÅHRAEUS, R.; P.LANE, D. The p16INK4a tumour suppressor protein inhibits αvβ3 integrin-mediated cell spreading on vitronectin by blocking PKC-dependent localization of αvβ3 to focal contacts. **The EMBO Journal**, v. 18, n. 8, p. 2106–2118, 1999.

FERNANDES, C. J. DA C. et al. Titanium-Enriched Medium Promotes Environment-Induced Epigenetic Machinery Changes in Human Endothelial Cells. **Journal of Functional Biomaterials**, v. 14, n. 3, 2023.

FRISCH, E. et al. Preclinical in vitro evaluation of implantable materials: conventional approaches, new models and future directions. **Frontiers in Bioengineering and Biotechnology**, v. 11, n. July, p. 1–15, 2023.

FUJITA, K. et al. Cytotoxicity profiles of multi-walled carbon nanotubes with different physico-chemical properties. **Toxicology Mechanisms and Methods**, v. 30, n. 7, p. 477–489, 2020.

GEMINI-PIPERNI, S. et al. Cellular behavior as a dynamic field for exploring bone

bioengineering: A closer look at cell-biomaterial interface. **Archives of Biochemistry and Biophysics**, v. 561, p. 88–98, 2014.

GHOLIZADEH, S. et al. Preparation and characterization of novel functionalized multiwalled carbon nanotubes/chitosan/β-Glycerophosphate scaffolds for bone tissue engineering. **International Journal of Biological Macromolecules**, v. 97, p. 365–372, 2017.

GIULIANI, A. et al. Could the enrichment of a biomaterial with conditioned medium or extracellular vesicles modify bone-remodeling kinetics during a defect healing? Evaluations on rat calvaria with synchrotron-based microtomography. **Applied Sciences (Switzerland)**, v. 10, n. 7, 2020.

GOMATHI, K. et al. Regulation of Runx2 by post-translational modifications in osteoblast differentiation. **Life Sciences**, v. 245, n. December 2019, 2020.

GOMES, A. M. et al. Nanohydroxyapatite-Coated Titanium Surface Increases Vascular Endothelial Cells Distinct Signaling Responding to High Glucose Concentration. **Journal of Functional Biomaterials**, v. 14, n. 4, 2023.

GOMEZ SANCHEZ, A. et al. Chitosan-hydroxyapatite nanocomposites: Effect of interfacial layer on mechanical and dielectric properties. **Materials Chemistry and Physics**, v. 217, n. November 2017, p. 151–159, 2018.

GORDON, K. J. et al. Bone morphogenetic proteins induce pancreatic cancer cell invasiveness through a Smad1-dependent mechanism that involves matrix metalloproteinase-2. **Carcinogenesis**, v. 30, n. 2, p. 238–248, 2009.

GRUBER, S.; NICKEL, A. Toxic or not toxic? The specifications of the standard ISO 10993-5 are not explicit enough to yield comparable results in the cytotoxicity assessment of an identical medical device. **Frontiers in Medical Technology**, v. 5, n. June, p. 1–14, 2023.

GUNGOR-OZKERIM, P. S. et al. **Bioinks for 3D bioprinting: An overview**. **Biomaterials Science**Royal Society of Chemistry, , 1 maio 2018.

GUO, L. et al. Adsorption of essential micronutrients by carbon nanotubes and the implications for nanotoxicity testing. **Small**, v. 4, n. 6, p. 721–727, 2008.

GUO, Z. et al. Antifungal properties of Schiff bases of chitosan, N-substituted chitosan and quaternized chitosan. **Carbohydrate Research**, v. 342, n. 10, p. 1329–1332, 2007.

GUSTAVSSON, J. et al. Ion reactivity of calcium-deficient hydroxyapatite in standard cell culture media. **Acta Biomaterialia**, v. 7, n. 12, p. 4242–4252, 2011.

HALLORAN, D.; DURBANO, H. W.; NOHE, A. Developmental review bone morphogenetic protein-2 in development and bone homeostasis. **Journal of Developmental Biology**, v. 8, n. 3, p. 28–30, 2020.

HART, N. H. et al. Biological basis of bone strength: Anatomy, physiology and measurement. **Journal of Musculoskeletal Neuronal Interactions**, v. 20, n. 3, p. 347–371, 2020.

HARTREE, E. F. Determination of Protein: A Modification of the Lowry Method that Gives a Linear Photometric Response. **Analytical Biochemistry**, v. 48, n. 0, p. 422–427, 1972.

HARUN, W. S. W. et al. A comprehensive review of hydroxyapatite-based coatings adhesion on metallic biomaterials. **Ceramics International**, v. 44, n. 2, p. 1250–1268, 2018.

HEID, S.; BOCCACCINI, A. R. Advancing bioinks for 3D bioprinting using reactive fillers: A review. **Acta Biomaterialia**, v. 113, p. 1–22, 2020.

HUH, J. T. et al. 3D Bioprinted Liver-on-a-Chip for Drug Cytotoxicity Screening. **Tissue Engineering - Part A**, v. 00, n. 00, p. 1–9, 2024.

HUNTER, G. K.; GOLDBERG, H. A. Nucleation of hydroxyapatite by bone sialoprotein. **Proceedings of the National Academy of Sciences of the United States of America**, v. 90, n. 18, p. 8562–8565, 1993.

INAM, A. K. M. S. et al. An Aptasensor Based on a Flexible Screen-Printed Silver Electrode for the Rapid Detection of Chlorpyrifos. **Sensors**, v. 22, n. 7, 1 abr. 2022.

JANN, J. et al. Influence of the TGF-β superfamily on osteoclasts/osteoblasts balance in physiological and pathological bone conditions. **International Journal of Molecular Sciences**, v. 21, n. 20, p. 1–58, 2020.

JANSEN, J. H. et al. Stretch-induced modulation of matrix metalloproteinases in mineralizing osteoblast via extracellular signal-regulated kinase-1/2. **Journal of Orthopaedic Research**, v. 24, n. 7, p. 1480–1488, 2006.

JIAN, Y. et al. Biological MWCNT/chitosan composite coating with outstanding anti-corrosion property for implants. **Colloids and Surfaces B: Biointerfaces**, v. 225, n. February, p. 113227, 2023.

JIN, Y. et al. Self-Supporting Nanoclay as Internal Scaffold Material for Direct Printing of Soft Hydrogel Composite Structures in Air. **ACS Applied Materials and Interfaces**, v. 9, n. 20, p. 17456–17465, 2017.

JURAK, M. et al. Temperature-dependent interactions in the chitosan/cyclosporine A system at liquid–air interface. **Journal of Thermal Analysis and Calorimetry**, v. 138, n. 6, p. 4513–4521, 2019.

JYOTI, J. et al. Improved nanomechanical and in-vitro biocompatibility of graphene oxide-carbon nanotube hydroxyapatite hybrid composites by synergistic effect. **Journal of the Mechanical Behavior of Biomedical Materials**, v. 117, n. February, p. 104376, 2021.

KALEV-ALTMAN, R. et al. The gelatinases, matrix metalloproteinases 2 and 9, play individual roles in skeleton development. **Matrix Biology**, v. 113, p. 100–121, 2022.

KANG, H. W. et al. A 3D bioprinting system to produce human-scale tissue constructs with structural integrity. **Nature Biotechnology**, v. 34, n. 3, p. 312–319, 2016.

KARSENTY, G. UPDATE on the BIOLOGY of OSTEOCALCIN. **Endocrine Practice**, v. 23, n. 10, p. 1270–1274, 2017.

KARSENTY, G.; FERRON, M. The contribution of bone to whole-organism physiology. **Nature**, v. 481, n. 7381, p. 314–320, 2012.

KESELOWSKY, B. G.; GARCÍA, A. J. Surface chemistry modulates integrin binding to direct cell adhesion and function. **Transactions - 7th World Biomaterials Congress**, p. 369, 2004.

KHOSWANTO, C. Role of matrix metalloproteinases in bone regeneration: Narrative review. **Journal of Oral Biology and Craniofacial Research**, v. 13, n. 5, p. 539–543, 2023.

KLIMEK, K. et al. "false" cytotoxicity of ions-adsorbing hydroxyapatite - Corrected method of cytotoxicity evaluation for ceramics of high specific surface area. **Materials Science and Engineering C**, v. 65, p. 70–79, 2016.

KOHLI, N. et al. Bone remodelling in vitro: Where are we headed?: -A review on the current understanding of physiological bone remodelling and inflammation and the strategies for testing biomaterials in vitro. **Bone**, v. 110, p. 38–46, 2018.

KOMORI, T. Regulation of osteoblast and odontoblast differentiation by RUNX2. **Journal of Oral Biosciences**, v. 52, n. 1, p. 22–25, 2010.

KOMORI, T. Regulation of proliferation, differentiation and functions of osteoblasts by runx2. **International Journal of Molecular Sciences**, v. 20, n. 7, 2019.

KOVRLIJA, I. et al. Challenging applicability of ISO 10993-5 for calcium phosphate biomaterials evaluation: Towards more accurate in vitro cytotoxicity assessment. **Biomaterials Advances**, v. 160, n. April, 2024.

KUMAR, M.; KUMAR, R.; KUMAR, S. Synergistic effect of carbon nanotubes and nano-hydroxyapatite on mechanical properties of polyetheretherketone based hybrid nanocomposites. **Polymers and Polymer Composites**, v. 29, n. 9, p. 1365–1376, 2021.

KYRIAKIDOU, K. et al. In vitro cytotoxicity assessment of pristine and carboxyl-functionalized MWCNTs. **Food and Chemical Toxicology**, v. 141, n. April, p. 111374, 2020.

LA ROCCA, G. et al. Zymographic detection and clinical correlations of MMP-2 and MMP-9 in breast cancer sera. **British Journal of Cancer**, v. 90, n. 7, p. 1414–1421,

2004.

LEE, Y. G.; JANG, A. Effect of the working and counter/quasi-reference electrode relative area ratio of silver sensor electrodes on voltammetric detection of Pb(II). **Journal of Industrial and Engineering Chemistry**, v. 81, p. 67–70, 2020.

LEFEBVRE, V.; PEETERS-JORIS, C.; VAES, G. Production of gelatin-degrading matrix metalloproteinases ('type IV collagenases') and inhibitors by articular chondrocytes during their dedifferentiation by serial subcultures and under stimulation by interleukin-1 and tumor necrosis factor α. **BBA - Molecular Cell Research**, v. 1094, n. 1, p. 8–18, 1991.

LI, C. et al. Hydroxyapatite based biocomposite scaffold: A highly biocompatible material for bone regeneration. **Saudi Journal of Biological Sciences**, v. 27, n. 8, p. 2143–2148, 2020a.

LI, C. et al. Hydroxyapatite based biocomposite scaffold: A highly biocompatible material for bone regeneration. **Saudi Journal of Biological Sciences**, v. 27, n. 8, p. 2143–2148, 1 ago. 2020b.

LI, J. et al. TGF-β2 and TGF-β1 differentially regulate the odontogenic and osteogenic differentiation of mesenchymal stem cells. **Archives of Oral Biology**, v. 135, n. November 2021, p. 105357, 2022.

LI, K.; TAY, F. R.; YIU, C. K. Y. The past, present and future perspectives of matrix metalloproteinase inhibitors. **Pharmacology and Therapeutics**, v. 207, p. 107465, 2020.

LI, P. et al. Promoting proliferation and differentiation of pre-osteoblasts MC3T3-E1 cells under combined mechanical and electrical stimulation. **Journal of Biomedical Nanotechnology**, v. 15, n. 5, p. 921–929, 2019.

LIANG, S.; LI, G.; TIAN, R. Multi-walled carbon nanotubes functionalized with a ultrahigh fraction of carboxyl and hydroxyl groups by ultrasound-assisted oxidation. **Journal of Materials Science**, v. 51, n. 7, p. 3513–3524, 2016.

LIN, X. et al. The Bone Extracellular Matrix in Bone Formation and Regeneration. **Frontiers in Pharmacology**, v. 11, n. May, p. 1–15, 2020.

LIU, X. W. et al. Effects of rutin on osteoblast MC3T3-E1 differentiation, alp activity and runx2 protein expression. **European Journal of Histochemistry**, v. 65, n. 1, p. 1–6, 2021.

MACHADO, M. I. P. et al. Cobalt-chromium-enriched medium ameliorates shear-stressed endothelial cell performance. **Journal of Trace Elements in Medicine and Biology**, v. 54, n. March, p. 163–171, 2019.

MALLAKPOUR, S.; MADANI, M. Effects of glucose-functionalized multiwalled carbon nanotubes on the structural, mechanical, and thermal properties of chitosan nanocomposite films. **Journal of Applied Polymer Science**, v. 132, n. 23, p. 1–9, 2015.

MARTINS, M. L. et al. Development and characterization of a new bio-nanocomposite (bio-NCP) for diagnosis and treatment of breast cancer. **Journal of Alloys and Compounds**, v. 584, p. 514–519, 2014.

MARTINS, M. L. et al. Glucose is an active chemical agent on degradation of hydroxyapatite nanostructure. **Materials Chemistry and Physics**, v. 240, n. September 2019, p. 122–166, 2020a.

MARTINS, M. L. et al. Immobilization of Paclitaxel on Hydroxyapatite for Breast Cancer Investigations. **Langmuir**, v. 36, n. 30, p. 8723–8732, 2020b.

MARTINS, M. L. et al. Immobilization of Paclitaxel on Hydroxyapatite for Breast Cancer Investigations. **Langmuir**, v. 36, n. 30, p. 8723–8732, 4 ago. 2020c.

MAURICIO-SÁNCHEZ, R. A. et al. FTIR spectroscopy studies on the spontaneous neutralization of chitosan acetate films by moisture conditioning. **Vibrational Spectroscopy**, v. 94, p. 1–6, 2018.

MAVROPOULOS, E. et al. **Biocompatibility of carbonated hydroxyapatite nanoparticles with different crystallinities**. Key Engineering Materials. **Anais**...Trans Tech Publications Ltd, 2012.

MISHRA, Y. G.; MANAVATHI, B. Focal adhesion dynamics in cellular function and disease. **Cellular Signalling**, v. 85, n. May, p. 110046, 2021.

MYGIND, T. et al. Mesenchymal stem cell ingrowth and differentiation on coralline hydroxyapatite scaffolds. **Biomaterials**, v. 28, n. 6, p. 1036–1047, 2007.

NAKAMURA, T. et al. Tissue-nonspecific alkaline phosphatase promotes the osteogenic differentiation of osteoprogenitor cells. **Biochemical and Biophysical Research Communications**, v. 524, n. 3, p. 702–709, 2020.

NAM, C. et al. Increased Hydrogel Swelling Induced by Absorption of Small Molecules. n. May, 2016.

NAZEER, M. A. et al. 3D printed poly(lactic acid) scaffolds modified with chitosan and hydroxyapatite for bone repair applications. **Materials Today Communications**, v. 25, n. April, p. 101515, 2020.

NEUMANN, C. et al. Osteopontin is induced by TGF-β2 and regulates metabolic cell activity in cultured human optic nerve head astrocytes. **PLoS ONE**, v. 9, n. 4, 2014.

O'CONNELL, M. (MICHAEL J. . **Carbon nanotubes : properties and applications**. [s.l.] CRC/Taylor & Francis, 2006.

OBERHAUS, F. V.; FRENSE, D.; BECKMANN, D. Immobilization techniques for aptamers on gold electrodes for the electrochemical detection of proteins: A review. **Biosensors**, v. 10, n. 5, 2020.

OHUCHI, S. Cell-SELEX Technology. **BioResearch Open Access**, v. 1, n. 6, p. 265–272, 2012.

OJEDA, E. et al. Nanometric Hydroxyapatite Particles as Active Ingredient for Bioinks: A Review. **Macromol**, v. 2, n. 1, p. 20–29, 2022.

OLIVEIRA, C. S.; LEEUWENBURGH, S.; MANO, J. F. New insights into the biomimetic design and biomedical applications of bioengineered bone microenvironments. **APL Bioengineering**, v. 5, n. 4, 2021.

ORGANIZATION, I. S. **Biological evaluation of medical devices - Part 12: Tests for in vitro cytotoxicity. International Standard Organization**Geneva, 2012.

PAN, M. H. et al. 3,5,3′,4′,5′ -Pentamethoxystilbene (MR-5), a synthetically methoxylated analogue of resveratrol, inhibits growth and induces G1 cell cycle arrest of human breast carcinoma MCF-7 Cells. **Journal of Agricultural and Food Chemistry**, v. 58, n. 1, p. 226–234, 2010.

PARK, J. H. et al. The effect of BMP-mimetic peptide tethering bioinks on the differentiation of dental pulp stem cells (DPSCs) in 3D bioprinted dental constructs. **Biofabrication**, v. 12, n. 3, 1 jul. 2020.

PARRA, J. P. R. L. L. et al. Using an Electrochemical Aptasensor to Early Detect Prostate Specific and Free Prostate Specific Antigens Released by Cancer Cells. **Electroanalysis**, v. 30, n. 12, p. 2869–2877, 2018.

PAULINO, A. T. et al. Characterization of chitosan and chitin produced from silkworm crysalides. **Carbohydrate Polymers**, v. 64, n. 1, p. 98–103, 2006.

PEDROSA, V. A. et al. Enhanced stability of enzyme organophosphate hydrolase interfaced on the carbon nanotubes. **Colloids and Surfaces B: Biointerfaces**, v. 77, n. 1, p. 69–74, 2010.

PEETERS-JORIS, C.; HAMMANI, K.; SINGER, C. F. Differential regulation of MMP-13 (collagenase-3) and MMP-3 (stromelysin-1) in mouse calvariae. **Biochimica et Biophysica Acta - Molecular Cell Research**, v. 1405, n. 1–3, p. 14–28, 1998.

PICOLLET-D'HAHAN, N. et al. Multiorgan-on-a-Chip: A Systemic Approach To Model and Decipher Inter-Organ Communication. **Trends in Biotechnology**, v. 39, n. 8, p. 788–810, 2021.

PIERÓG, M.; OSTROWSKA-CZUBENKO, J.; GIERSZEWSKA-DRUZYŃSKA, M. Thermal degradation of double crosslinked hydrogel chitosan membranes. **Progress on Chemistry and Application of Chitin and its Derivatives**, v. 2012, p. 67–74, 2012.

PRAMANIK, N. et al. Chemical Synthesis, Characterization, and Biocompatibility Study of Hydroxyapatite/Chitosan Phosphate Nanocomposite for Bone Tissue Engineering Applications. **International Journal of Biomaterials**, v. 2009, p. 1–8, 2009.

PRIDEAUX, M. et al. MMP and TIMP temporal gene expression during

osteocytogenesis. **Gene Expression Patterns**, v. 18, n. 1–2, p. 29–36, 2015.

PRZEKORA, A. The summary of the most important cell-biomaterial interactions that need to be considered during in vitro biocompatibility testing of bone scaffolds for tissue engineering applications. **Materials Science and Engineering C**, v. 97, n. January, p. 1036–1051, 2019.

PUCCI-MINAFRA, I. et al. Zymographic analysis of circulating and tissue forms of colon carcinoma gelatinase A (MMP-2) and B (MMP-9) separated by mono- and two-dimensional electrophoresis. **Matrix Biology**, v. 20, n. 7, p. 419–427, 2001.

RAHMAN, S. F. et al. Effect of graphite, graphene oxide, and multi-walled carbon nanotubes on the physicochemical characteristics and biocompatibility of chitosan/hyaluronic acid/hydroxyapatite scaffolds for tissue engineering applications. **Journal of Science: Advanced Materials and Devices**, v. 9, n. 2, p. 100719, 2024.

RAIS, A. et al. A review on regulation of cell cycle by extracellular matrix. **International Journal of Biological Macromolecules**, v. 232, n. November 2022, p. 123426, 2023.

RAMESH, N.; MORATTI, S. C.; DIAS, G. J. **Hydroxyapatite–polymer biocomposites for bone regeneration: A review of current trends**. **Journal of Biomedical Materials Research - Part B Applied Biomaterials**John Wiley and Sons Inc., , 1 jul. 2018.

RATH, P. C. et al. Multiwalled carbon nanotubes reinforced Hydroxyapatite-chitosan composite coating on Ti metal: Corrosion and mechanical properties. **Journal of the American Ceramic Society**, v. 95, n. 9, p. 2725–2731, 2012a.

RATH, P. C. et al. **Multiwalled carbon nanotubes reinforced Hydroxyapatite-chitosan composite coating on Ti metal: Corrosion and mechanical properties**. Journal of the American Ceramic Society. **Anais**...set. 2012b.

REN, B. et al. Injectable polysaccharide hydrogel embedded with hydroxyapatite and calcium carbonate for drug delivery and bone tissue engineering. **International Journal of Biological Macromolecules**, v. 118, p. 1257–1266, 2018.

ROGINA, A.; IVANKOVI, M.; IVANKOVI, H. Preparation and characterization of nano-hydroxyapatite within chitosan matrix. v. 33, p. 4539–4544, 2013.

SADAT-SHOJAI, M. METHODS FOR NANOSIZED HYDROXYAPATITE WITH DIVERSE STRUCTURES et al. Synthesis methods for nanosized hydroxyapatite with diverse structures. **Acta Biomaterialia**, v. 9, n. 8, p. 7591–7621, 2013.

SADEGHIANMARYAN, A. et al. Fabrication of chitosan/alginate/hydroxyapatite hybrid scaffolds using 3D printing and impregnating techniques for potential cartilage regeneration. **International Journal of Biological Macromolecules**, v. 204, n. January, p. 62–75, 2022.

SANCHEZ, A. G. et al. Chitosan-hydroxyapatite-MWCNTs nanocomposite patch for bone tissue engineering applications. **Materials Today Communications**, v. 28, 1 set. 2021.

SHAFIEE, A. et al. Physics of bioprinting. **Applied Physics Reviews**, v. 6, n. 2, 2019.

SHAIKH, A. et al. Cell cycle regulators and bone: development and regeneration. **Cell and Bioscience**, v. 13, n. 1, p. 1–9, 2023.

SHIBUTANI, T. et al. Tissue inhibitors of metalloproteinases (TIMP-1 and TIMP-2) stimulate osteoclastic bone resorption. **Journal of Bone and Mineral Metabolism**, v. 17, n. 4, p. 245–251, 1999.

SHIRAHAMA, H. et al. Precise tuning of facile one-pot gelatin methacryloyl (GelMA) synthesis. **Scientific Reports**, v. 6, 9 ago. 2016.

SI, J. et al. Osteopontin in Bone Metabolism and Bone Diseases. **Medical Science Monitor**, v. 26, p. 1–9, 2020.

SKARDAL, A. et al. Multi-tissue interactions in an integrated three-tissue organ-on-a-chip platform. **Scientific Reports**, v. 7, n. 1, p. 1–16, 2017.

SKARDAL, A. et al. Drug compound screening in single and integrated multi-organoid body-on-a-chip systems. **Biofabrication**, v. 12, n. 2, 2020.

SMOLINSKÁ, V.; BOHÁČ, M.; DANIŠOVIČ, Ľ. Current Status of the Applications of Conditioned Media Derived from Mesenchymal Stem Cells for Regenerative Medicine. **Physiological Research**, v. 72, p. S233–S245, 2023.

SUNG, J. H. et al. **Recent Advances in Body-on-a-Chip Systems**. **Analytical Chemistry**American Chemical Society, , 2 jan. 2019.

TAVONI, M. et al. Bioactive calcium phosphate-based composites for bone regeneration. **Journal of Composites Science**, v. 5, n. 9, 2021.

TOH, H. S. et al. Chemical interactions between silver nanoparticles and thiols: A comparison of mercaptohexanol against cysteine. **Science China Chemistry**, v. 57, n. 9, p. 1199–1210, 2014.

TOMÁS, H.; ALVES, C. S.; RODRIGUES, J. **Laponite®: A key nanoplatform for biomedical applications? Nanomedicine: Nanotechnology, Biology, and Medicine**Elsevier Inc., , 1 out. 2018.

TOMASZEWSKA, E. et al. Trabecular bone parameters, TIMP-2, MMP-8, MMP-13, VEGF expression and immunolocalization in bone and cartilage in newborn offspring prenatally exposed to fumonisins. **International Journal of Molecular Sciences**, v. 22, n. 22, 2021.

TOUANI, F. K. et al. Pharmacological Preconditioning Improves the Viability and Proangiogenic Paracrine Function of Hydrogel-Encapsulated Mesenchymal Stromal Cells. **Stem Cells International**, v. 2021, 2021.

TOWNSEND, T. A. et al. BMP-2 and TGFβ2 shared pathways regulate endocardial cell transformation. **Cells Tissues Organs**, v. 194, n. 1, p. 1–12, 2011.

ŢUCUREANU, V. et al. Critical Reviews in Analytical Chemistry FTIR Spectroscopy for Carbon Family Study FTIR Spectroscopy for Carbon Family Study. **Critical Reviews in Analytical Chemistry**, v. 46, n. 6, p. 502–520, 2016.

ŢUCUREANU, V.; MATEI, A.; AVRAM, A. M. FTIR Spectroscopy for Carbon Family Study. **Critical Reviews in Analytical Chemistry**, v. 46, n. 6, p. 502–520, 2016.

TÜRK, S. et al. 3D porous collagen/functionalized multiwalled carbon nanotube/chitosan/hydroxyapatite composite scaffolds for bone tissue engineering. **Materials Science and Engineering C**, v. 92, p. 757–768, 1 nov. 2018.

TUTAK, W. et al. Toxicity induced enhanced extracellular matrix production in osteoblastic cells cultured on single-walled carbon nanotube networks. **Nanotechnology**, v. 20, n. 25, 2009.

VANCEA, A.; SERBAN, O.; FODOR, D. Relationship between osteopontin and bone mineral density. **Acta Endocrinologica**, v. 17, n. 4, p. 509–516, 2021.

VENKATESAN, J. et al. Preparation and characterization of carbon nanotube-grafted-chitosan - Natural hydroxyapatite composite for bone tissue engineering. **Carbohydrate Polymers**, v. 83, n. 2, p. 569–577, 2011.

VIMALRAJ, S. Alkaline phosphatase: Structure, expression and its function in bone mineralization. **Gene**, v. 754, n. April, p. 144855, 2020.

VISWANATHAN, N.; SUNDARAM, C. S.; MEENAKSHI, S. Sorption behaviour of fluoride on carboxylated cross-linked chitosan beads. **Colloids and Surfaces B: Biointerfaces**, v. 68, n. 1, p. 48–54, 2009.

WAGLEY, Y. et al. Canonical Notch signaling is required for bone morphogenetic protein-mediated human osteoblast differentiation. **Stem Cells**, v. 38, n. 10, p. 1332–1347, 2020.

WANG, H. et al. Synthesis and bioactivity of gelatin/multiwalled carbon nanotubes/hydroxyapatite nanofibrous scaffolds towards bone tissue engineering. **RSC Advances**, v. 5, n. 66, p. 53550–53558, 2015.

WENZ, A. et al. Hydroxyapatite-modified gelatin bioinks for bone bioprinting. **BioNanoMaterials**, v. 17, n. 3–4, p. 179–184, 1 set. 2016.

WENZ, A. et al. Bone matrix production in hydroxyapatite-modified hydrogels suitable for bone bioprinting. **Biofabrication**, v. 9, n. 4, 2017.

WESTON, W. A.; BARR, A. R. A cell cycle centric view of tumour dormancy. **British Journal of Cancer**, v. 129, n. 10, p. 1535–1545, 2023.

WILLIAMSON, A. et al. The future of the patient-specific Body-on-a-chip. **Lab on a Chip**, v. 13, n. 18, p. 3471–3480, 2013.

WOOD, P. F. et al. The Action of Angiocrine Molecules Sourced from Mechanotransduction-Related Endothelial Cell Partially Explain the Successful of Titanium in Osseointegration. **Journal of Functional Biomaterials**, v. 14, n. 8, 2023.

XI, Y. et al. Tissue inhibitor of metalloproteinase 1 suppresses growth and differentiation of osteoblasts and differentiation of osteoclasts by targeting the AKT pathway. **Experimental Cell Research**, v. 389, n. 2, p. 111930, 2020.

ZANDI, N. et al. Nanoengineered shear-thinning and bioprintable hydrogel as a versatile platform for biomedical applications. **Biomaterials**, v. 267, n. October 2020, p. 120476, 2021.

ZHANG, X. et al. Dose reduction of bone morphogenetic protein-2 for bone regeneration using a delivery system based on lyophilization with trehalose. **International Journal of Nanomedicine**, v. 13, p. 403–414, 12 jan. 2018.

ZHANG, Y. L. et al. Electrochemical aptasensor based on proximity-dependent surface hybridization assay for single-step, reusable, sensitive protein detection. **Journal of the American Chemical Society**, v. 129, n. 50, p. 15448–15449, 19 dez. 2007.

ZHAO, X.; LIU, R. Recent progress and perspectives on the toxicity of carbon nanotubes at organism, organ, cell, and biomacromolecule levels. **Environment International**, v. 40, n. 1, p. 244–255, 2012.